DEVELOPMENT OF A PHOTOACOUSTIC IMAGING SYSTEM

DEVELOPMENT OF A MULTI-SPECTRAL PHOTOACOUSTIC IMAGING SYSTEM FOR DETECTION OF INTRACRANIAL HEMATOMA

By JOSHUA BLAZINA, BS

A Thesis Submitted to the School of Graduate Studies in Partial Fulfillment of the Requirements for the Degree Master of Applied Science

McMaster University

MASTER OF APPLIED SCIENCE (2023)

Hamilton, Ontario, Canada (School of Biomedical Engineering)

TITLE:	Development of a Multi-spectral Photoacoustic Imaging System for Detection of Intracranial Hematoma
AUTHOR:	Joshua Blazina B.Sc (Neuroscience), McMaster University, Hamilton, Canada
SUPERVISOR:	Dr. Troy Farncombe
NUMBER OF PAGES:	xiii, 131

Abstract

Head trauma patients are susceptible to secondary injuries where afflicted tissues can propagate towards dysfunction after the initial injury is treated. Monitoring blood oxygenation (SpO_2) below the skull is crucial for the early detection of secondary head injury such as hematoma. To obtain such information in a point-of-care setting, photoacoustic (PA) imaging can be used to differentiate optical contrast between hemoglobin (Hb) species by measuring resultant ultrasonic waves emitted by optically irradiated tissue. Given the ratio of Red:NIR light absorption, information regarding SpO_2 can be determined *in vivo*. In this project, computer simulations involving PA imaging of tissue models have been performed and techniques tested using an optic fiber/transducer PA imaging system. In simulated and physical PA scans, Red:NIR ratio values are computed for various tissue models to evaluate optical contrast in target absorbers. Images reconstructed from simulations showed the ability to visualize differences in SpO_2 across a layer of skull tissue using multi-spectral optical irradiation. Red:NIR ratios were calculated using PA signals produced by 750 nm light and 850 nm light. Physical image reconstructions were conducted using a 5 ns pulsed laser and near-infrared (NIR) optical parametric oscillator (OPO). The pulse energy used during physical PA raster scans reached up to 5.3 mJ/pulse. Tissue phantoms

scanned consisted of optical absorbers surrounded by various tissue-mimicking materials. Images from physical acquisitions were acquired using a 2D CNC-controlled moving stage, but free-hand tracking using inertial and optical sensors have been investigated. At 5.3 mJ/pulse, images reconstructed from physical scans could not resolve optical absorbers positioned beneath a layer of skull-mimicking tissue. A limiting factor contributing to low signal-to-noise ratio (SNR) from inferior absorbers was the percentage of power lost during beam focusing. However, simulation results encourage future work to improve pulse energy output before simulation results can be validated.

Acknowledgements

I would like to express my utmost appreciation for my supervisor, Dr. Troy Farncombe, whose willingness to always make himself available has made a huge difference in my confidence. Your patience has been extremely encouraging and inspires me to push forward.

I would also like to thank my supervisory committee, for their valuable advice throughout this project.

Finally, thank you to my family and friends for their unwavering belief in me. I am truly blessed to be surrounded by constant love and support.

Table of Contents

List of Figures

List of Tables

Acronyms

CT	computer tomography
CNC	computer numerical control
HbO	oxygenated hemoglobin
HHb	deoxygenated hemoglobin
ICH	intracranial hematoma
Nd:YAG	neodymium-doped yttrium aluminum garnet; Nd:$Y_3Al_5O_{1_2}$
NIR	near-infrared
OD	optical density
SpO_2	peripheral capillary oxyegn saturation
PA	photoacoustic
SNR	signal-to-noise ratio

Chapter 1

Introduction

1.1 Intracranial Hemorrhage

Hemorrhagic stroke as a result of secondary injury can have dangerous, but preventable consequences given early detection. In Western societies, about 80% of strokes are caused by focal cerebral ischemia due to arterial occlusion, and the remaining 20% are caused by hemorrhages [17]. Hemorrhages in the brain occur when an intracranial artery bursts due to the weakening of blood vessel walls. Arteries can rupture for multiple reasons and can result in the pooling of blood called a hematoma [50]. During the onset of hemorrhagic stroke, sections of brain tissue downstream of the damage lose their supply of oxygen and nutrients, as well as inherit the risk of physical damage due to compression from an increase in intracranial pressure [18]. Below the skull, various layers of the meninges provide protection and stability to the brain while also offering structured passage for blood vessels and cerebrospinal fluid (CSF). Accordingly, intracranial hematomas (ICH) can form below any three of the layers of the meninges and may settle in different geometries based on the superior

layer. For example, epidural hematomas form below the cranium and above the most superior layer of the meninges, the dura mater. Due to the rigid connection between the dura mater and the skull, the blood pooling will appear as a lens shape. On the contrary, subdural hematomas are more mobile and able to move beneath the dura mater and may form in crescent shapes. In severe cases of subdural hematoma, the mass of the hematoma may compress the brain to produce a midline shift, where imaging can reveal a lateral push of the longitudinal fissure [29]. Examples of ICH geometry can be seen in Fig. 1.1.

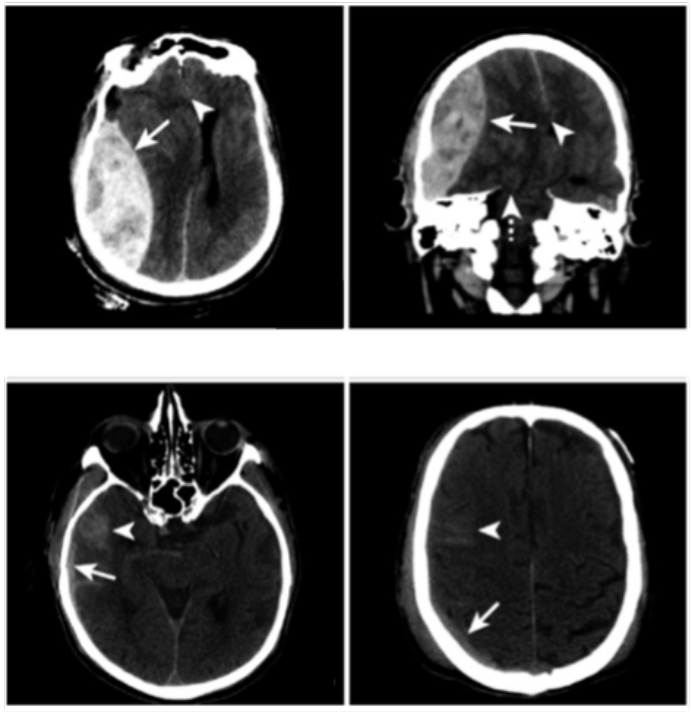

Figure 1.1: Non-Contrast CT images of ICH. Top row images show an epidural hematoma in the right cerebral hemisphere resulting in leftward mid-line shift. Bottom row images show a subdural hematoma in the right cerebral hemisphere [29].

In 2015, Panchal *et al.* studied cases of primary ICH, in which the cause of the condition was non-traumatic [61]. For a sample size of 50 patients, X-Ray Computed Tomography (CT) was used to stratify the sizes of ICH as they relate to different risks of mortality. 78% of patients exhibited "small" ICH, with a diameter of 1-2 cm and volume $< 30mL$. The remaining patients exhibited "massive" ICH with a volume $> 30mL$ and were at a distinctly higher risk of mortality.

Imaging protocols can allow for the identification of brain regions affected during ICH, as well as classify 3 intra-regional zones. Specifically, areas of the brain with decreased blood flow will often possess any combination of an infarct core, a penumbra, and an oligemic penumbra. The infarct core represents tissue that has lost physiological function permanently from the decrease in oxygen supply. The penumbra describes tissue that has lost function but can be salvaged if reperfusion occurs after thrombolysis. Finally, oligemic penumbra identifies a region of tissue experiencing asymptomatic hypoperfusion. The oligemic penumbra differs from the penumbra since the tissue region often recovers without reperfusion treatment [43] [65]. Therefore, the timing of clinical intervention during emergent ICH can have profound effects on long-term rehabilitation. Current clinical practices diagnose acute ICH through various structural imaging techniques [31] [19]; however, urgency in identification is often used to justify trade-offs in spatial resolution for point-of-care functionality [75]. For point-of-care monitoring of ICH, novel imaging systems require a spatial resolution of 0.5 - 2 *mm* to rival CT and MR [47].

1.2 Non-Invasive Transcranial Imaging

Clinical imaging techniques each take advantage of different biophysical principles to derive contrast between compounds in the human body. There are two considerations to be made when prioritizing an imaging technique for a certain clinical application.

First, hospitals must be designed such that imaging systems are available to optimize patient throughput. Hospitals must be responsible for supplying diagnostic systems for a wide variety of conditions, while also budgeting cost-effectively. For example, Positron Emission Tomography (PET) is often relied on for robust metabolic information, while X-Ray Computed Tomography (CT) and Magnetic Resonance (MR) scanners are common for structural imaging. However, due to fiscal constraints [28] [5], there is usually a lack of access to PET, X-Ray CT, and MR scanners. Therefore, there is a need for the development of cost-effective point-of-care imaging systems to relieve hospitals of patient backlog [7]. Point-of-care imaging systems describe diagnostic techniques which provide clinically relevant information in real-time, at the bedside. For the diagnosis of ICH, point-of-care imaging will remove the inconvenience of relocating a brain trauma patient to a scanner room, as well as cater to urgency with real-time data acquisition. Currently, functional Near-Infrared Spectroscopy (NIRS) has been pursued as a point-of-care outlet for brain imaging but is seldom used due to a low Signal-to-Noise Ratio during transcranial applications [12].

Second, healthcare must provide diagnostic techniques that cater to a wide variety of diseases, disorders, and injuries. In this chapter, a brief technical summary of X-Ray CT, MR, PET, and NIRS will be used to explore each technique's relevance to diagnosing ICH. Deficits for each system will be identified, and an opportunity for the development of a new imaging system will be described.

X-Ray CT scanners use a transmission-based technique to measure the attenuation of incident X-rays due to absorption and scattering across different tissues. The attenuation of X-Rays is directly proportional to the electron densities of different tissues, and representative values for different tissues are recorded as Hounsfield Units [23]. Eqn. 1.2.1 shows the formula used by X-ray CT to describe beam transmission.

$$I = I_0 e^{-\sum_{i=1}^{n} u_i x_i} \tag{1.2.1}$$

Where I is resultant beam intensity, I_0 is incident beam intensity, u_i is a tissue's attenuation coefficient (m^{-1}), and x_i is that tissue's thickness (m). With multiple transmission measurements in the same plane but at different orientations, u_i and x_i can be allocated to image pixels during tomographic image reconstruction. Therefore, contrast on CT is predominantly determined by tissue density. With respect to ICH, hematomas rapidly increase in hematocrit percentage (ratio of red blood cells to blood volume) and as a result, appear hyperintense on CT scans [13]. Overall, X-Ray CT is the most common modality used to image acute stroke and can offer spatial resolution superior to that of other options relatively quickly. To monitor ICH, serial Perfusion CT is used to calculate cerebral blood volume (CBV)-cerebral blood flow (CBF) mismatches. Serial imaging of a volume of brain tissue over time during the injection of an intravenous iodinated contrast bolus allows for the calculation of time-dependent changes in contrast concentration. As a result, a time-density curve can be plotted, and CBF, CBV, and mean transit time (MTT) can provide information about infarction [65]. In a study by Wang *et al.* in 2021 [80], perfusion characteristics of ICH patients were assessed using X-ray CT. From a sample cohort of 50 patients with ICH symptoms appearing less than 6 hours previous, Wang *et al.* suggest that

after hemorrhage, the edema would be hypoperfusive (low CBF), and surrounding areas would exhibit hyperperfusion (high CBF). Caveats to X-ray CT include the use of ionizing radiation that may be harmful to children or patients requiring serial CT scanning.

Despite having a slightly inferior spatial resolution, MR is another structural imaging modality with the potential to diagnose ICH. MR produces contrast between tissue structures based on differences in the local magnetic fields that each tissue's protons experience [51]. To diagnose ICH using principles of MR, susceptibility-weighted imaging (SWI) is the most reliable pulse sequence for selectively detecting various blood products. Specifically, oxygenated hemoglobin (HbO) and deoxygenated hemoglobin (HHb) interact with external magnetic fields according to principles of diamagnetism and paramagnetism respectively [83]. The mechanisms by which magnetic compounds interact in tissue is out of the scope of this thesis. By exploiting this endogenous contrast, MR offers improved sensitivity to ICH compared to CT without the use of ionizing radiation. A drawback specific to MR includes the long data acquisition times. Not only are CT and MR scans both inconvenient to administer to brain trauma patients, but MR imaging will lead to longer delays before treatment can intervene with the onset of symptoms.

Ultrasound (US) imaging should also be recognized as a common structural imaging modality, but is rarely used in transcranial applications. US imaging relies on acoustic impedance mismatches between tissues to detect US waves reflected at tissue boundaries [58]. However, poor penetration of US waves through the skull limits SNR at tissue depths relevant to ICH.

Conversely, functional imaging modalities may also reveal information about ICH.

PET imaging can use signals produced by radioactive tracers to quantify the metabolism of various compounds in the brain. Although fiscal constraints limit public access to PET scans, the health risks of ionizing radiation [10] in children should also be considered. According to a study by Hamada *et al.* [27], a single case of chronic expanding hematoma showed evidence of increased glucose uptake in tissue adjacent to the expanding hematoma. Despite the capability to track a wide range of biological processes, PET imaging of ICH does not have a practical patient timeline from diagnosis to treatment. Many PET imaging paradigms suggest that scans take place 1 hour after radiotracer injection [79] which may not be practical in urgent care situations. Should there be any metabolic data deemed clinically relevant to ICH, many standalone PET images lack the anatomical detail required for diagnostic interpretation [53]. It remains true however, that anatomic detail becomes less an issue in critical situations such as the onset of ICH.

The other relevant functional imaging technique for ICH diagnosis is functional NIRS. NIRS is an optical imaging technique capable of measuring global tissue oxygenation (SpO_2) levels beneath the skull. The contrast in the optical signals detected during NIRS is derived from differences in the absorption of incident photons by endogenous chromophores [9]. Specifically, oxygenated hemoglobin (HbO) and deoxygenated hemoglobin (HHb) absorb different amounts of near-infrared (NIR) wavelengths (Fig. 1.2), and the intensity of the reflected photons is indicative of the concentration of the different chromophores. According to a review by Chen *et al.* [9], software for real-time display of functional NIRS data is not yet available, due in part to the extensive post-acquisition processing required to extract changes in concentration from low signal-to-noise ratios (SNR). Low SNR from NIRS in transcranial

applications such as ICH detection is inevitable due to the high scattering of NIR light by the skull. The skull is responsible for scattering the incident photons before the excitation of hemoglobin species, as well as attenuating much of the reflected signal. However, it remains true that absorption of NIR wavelengths by human body tissue is low and much attenuation can be attributed appropriately to the presence of molecules of interest. Therefore in clinical trials, functional NIRS shows promise of detecting ICH in a timely and non-invasive manner.

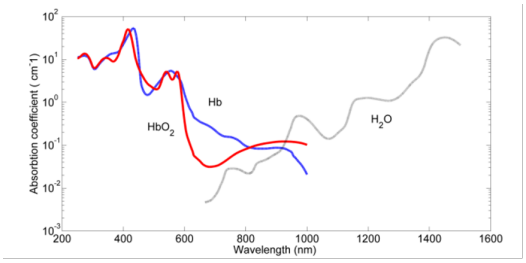

Figure 1.2: Absorption Spectra of Hb Species [46].

The current state of diagnostic imaging for the purpose of critical care demands point-of-care modalities. Popular imaging techniques such as PET, MRI, and NIRS are subject to ionizing radiation, risky time delays, and low SNR. Photoacoustic (PA) imaging is a multimodal technique that detects an ultrasonic pressure wave produced by tissue that has absorbed pulsed light energy. The resultant pressure wave is called a PA signal (Fig. 1.3) and provides two key pieces of information. First, following the illumination with light, the time at which the peak of a pressure wave arrives at a transducer is directly correlated to the depth at which optical absorption occurs. Second, the amplitude of the photoacoustic signal is directly correlated to the amount of absorption that occurs. PA imaging exploits the same optical contrast in hemoglobin species as NIRS but improves upon the SNR. PA signal detection can preserve the optical contrast more efficiently than NIRS because ultrasonic pressure

waves produced by PA imaging are subject to less attenuation than optical photons [81]. The PA effect was first recorded in detail in the late 19th century by Alexander Graham Bell [3], but it was not until 1993 that Chen *et al.* [8] first used pulsed PA imaging to study anatomy *in vivo*. The development of PA imaging systems for the purpose of detecting ICH is encouraged by the alignment of the hemoglobin absorption spectra with the biological optical window, allowing for an increase in sensitivity and penetration depth compared to other optical techniques. To monitor blood SpO_2, PA imaging observes optical contrast between hemoglobin (Hb) species through the measurement of PA waves emitted by a section of optically irradiated tissue. It should be noted that Thermoacoustic (TA) imaging techniques have also been explored [89] [76] to extend the imaging depth capabilities by using microwaves to induce the PA effect in tissues. Using microwaves, the contrast in TA images is derived from differences in the dielectric properties and conductivity of tissues [32]. Compared to PA imaging, TA imaging cannot differentiate between species of hemoglobin, meaning ICH diagnosis relies more heavily on the spatial resolution of images to discern anomalies in the geometries of blood on the surface of the brain.

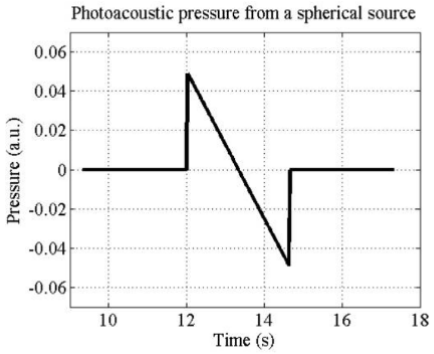

Figure 1.3: An example "N-wave" PA signal produced by a spherical source [44]

1.3 Principles of Photoacoustic Imaging

1.3.1 The Photoacoustic Effect

PA and TA imaging derive analog signals according to the PA or TA effect respectively. The PA effect occurs when any sample of chromophores absorbs electromagnetic (EM) energy and undergoes thermoelastic expansion [90]. Specifically, when a section of tissue absorbs heat energy, the tissue will expand and contract as it accumulates and releases energy and emits this mechanical energy in the form of a pressure wave. This pressure wave is then characterized as a photoacoustic signal and propagates away from the source in all directions to be detected by a pressure sensor such as a piezoelectric transducer. For a PA signal to be emitted from a tissue section, the energy of the incoming light wave must meet the energy levels of the electrons in the chromophores. When this parameter is satisfied, electrons will absorb the EM energy of photons and enter an excited quantum energy state, heating the molecule and subsequently expanding. With respect to an analog PA signal, the amplitude of the pressure wave released is directly correlated to the amount of power absorbed (W) that occurs in the volume of irradiated tissue. Also, because the shape of the detected acoustic wavefront has a compression and rarefaction component, the distance between the two peaks in time is proportional to the size of the absorber [84].

The review paper by Zhou *et al.* [90] outlines the conditions required to produce a pressure wave in a volume of tissue using electromagnetic energy. To efficiently produce the PA effect, the incident pulse of photons must occur quicker than the time it takes for both stress and heat to traverse the voxel. When a short, pulsed

light source irradiates a section of tissue, thermal and stress relaxation time parameters define the time limit within which a pulse width can confine thermal diffusivity and volume expansion to the duration of illumination. While stress and thermal confinement conditions are met, both stress and heat can accumulate sufficiently in the volume of interest to establish the necessary conditions for thermoelastic expansion. The relationships for the confinement conditions are described in Eqn. 1.3.1 and 1.3.2 as follows:

$$\tau_{\text{th}} = \frac{d^2}{\alpha_{\text{th}}} \tag{1.3.1}$$

Where τ_{th} is the thermal confinement time (s), d is the spatial resolution of the voxel of interest (mm), and α_{th} is the thermal diffusivity of the tissue in the volume of interest (mm^2/s).

$$\tau_{\text{s}} = \frac{d}{c} \tag{1.3.2}$$

Where τ_{s} is the stress confinement time (s), and c is the speed of sound for the media voxel of interest. For example, According to Eqn. 1.3.1 and 1.3.2, to resolve a PA signal reliably from a 1 mm^3 voxel of soft tissue, the optical energy pulse must be employed as follows: For soft tissue, the speed of sound is approximately 1500 m/s and the thermal diffusivity is 0.14 mm^2/s, meaning that the optical energy pulse must be less than 1.786 s to satisfy the thermal confinement condition, and less than 666 ns to satisfy the stress confinement condition. Heat is confined much more efficiently in soft tissue than stress, but nonetheless, rapid excitation of soft tissue is necessary to generate the PA effect.

Pulsed light emitting diodes (LED) can produce PA-based tomographic images, however Francis *et. al* [35] cite low pulse energy as a limitation for larger, more absorbing tissues. Nonetheless, LED PA imaging systems offer a cost-effective, portable solution to superficial imaging of tissues in point-of-care settings. The implementation of a pulsed laser light source for PA effect generation is more expensive, but will produce higher SNR, which is essential for transcranial imaging applications. For many applications, pulsed lasers have shown to reliably produce PA signals [82] [42] [38].

The relationship between the energy imparted on a section of tissue and the resultant initial pressure rise is also established for a laser pulse in Eqn. 1.3.3 [90]. If the pulse width from the incident light, τ, is less than τ_{th} and τ_{s}, then fractional volume change is negligible, and the following is true:

$$\text{if } \tau < \tau_{\text{th}} \text{ and } \tau_{\text{s}}, \quad p_0 = \frac{\beta \Delta T}{\kappa} \tag{1.3.3}$$

Where p_0 is the initial pressure rise (Pa), β is the thermal coefficient of volume expansion (K^{-1}), ΔT is the change in temperature (K) and κ is the isothermal compressibility coefficient (Pa^{-1}).

Further, the local change in temperature can be expressed as:

$$\Delta T = \frac{\eta_{\text{th}} A_e}{\rho C_v} \tag{1.3.4}$$

Where η_{th} is the percentage of absorbed light converted into heat, ρ is the density of the medium, A_e is the specific optical energy deposition (J/m^3), and C_v is the specific heat of the illuminated region at constant volume.

By substituting Eqn. 1.3.3 into Eqn. 1.3.4 , we can derive:

$$p_0 = \frac{\beta \eta_{\text{th}} A_e}{\kappa \rho C_v} \tag{1.3.5}$$

Next, the Grunesian parameter Γ (dimensionless) can be defined as:

$$\Gamma = \frac{\beta}{\kappa \rho C_v} \tag{1.3.6}$$

And the equation for the initial pressure rise becomes:

$$p_0 = \Gamma \eta_{\text{th}} A_e \tag{1.3.7}$$

1.3.2 Light Propagation in Tissue

ICH can develop in almost any region of the brain, and as such, the behaviour of photons and their interactions at different depths must be understood. Light propagation in tissue is described by instances of scattering and absorption that attenuate and disperse photons according to different concentrations of chromophores. During optical imaging, photons will encounter depths in the tissue sample that can be characterized by distinct levels of scattering. The amount of scattering is described using quantifiable distances known as the mean free path (MFP) and the transport mean free path (TMFP) [85]. MFP describes the average distance that a photon travels in the tissue model between two consecutive scattering events. TMFP describes the mean propagation distance that it takes for the directionality of photons, on average, to lose relation to the direction they had before entering the tissue.

The average values for MFP and TMFP vary according to tissue type and the

wavelength of light used, however, TMFP is typically ten times larger than MFP for the same conditions [60]. On average, the MFP for photons in tissue is about 0.1 mm, and the TMFP is about 1 mm. According to Wang (2008) [77] at an average of 10 TMFP, incident photons lose all relation to the direction of their initial velocity.

Before light travels 1 TMFP, optical fluence, $\phi(d)$ (W/cm^2), is described by the ballistic regime in Eqn. 1.3.8, where essentially no scattering has taken place [44].

$$\phi(d) = \phi_0 e^{-\mu_a d} \tag{1.3.8}$$

Where ϕ_0 is the initial fluence emitted by the light source (W/cm^2), μ_a is the absorption coefficient of the medium (cm^{-1}), and d is the distance travelled by the photons (cm). Any effect on attenuation of optical energy in the ballistic regime is attributed strictly to absorption by superior layers.

After 1 TMFP, photons enter the quasi-diffusive or completely diffusive regime, where optical intensity is a result of photons that have been scattered multiple times. Eqn. 1.3.9 illustrates the influence of scattering on ϕ(d).

$$\phi(d) = \phi_0 e^{-\mu_{eff} d} \quad , \quad \mu_{eff} = \sqrt{3\mu_a(\mu_a + \mu_s)} \tag{1.3.9}$$

Where μ_s is the scattering coefficient (cm^{-1}). The behaviour of light scattering is defined by both the wavelength of the incident light (λ) and the size of the scattering particles (Fig. 1.4). In tissue, λ is comparable to the size of the scattering object, and as a result, forward (Mie) scattering is predominant. This is in contrast to isotropic (Rayleigh) scattering, in which the size of the scattering object is $< 1/10$ the size of the incident wavelength, and directionality of scattered photons is conserved to little

or no effect [59]. For the detection of ICH, the target blood tissue will be several mm deep, and will experience excitation by diffuse light. Therefore optical energy deposition in ICH tissue models can most accurately be described via Eqn. 1.3.9.

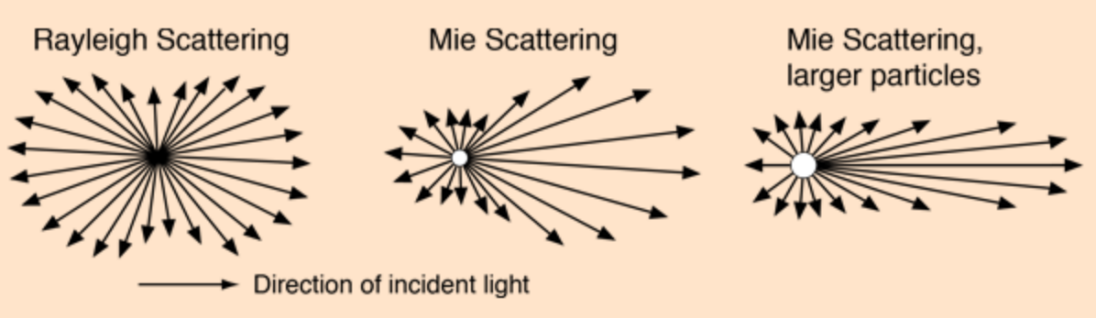

Figure 1.4: Schematic of Mie and Rayleigh Scattering. Image adapted from [59]

1.3.3 Sound Propagation in Tissue

Following thermoelastic expansion and contraction, an ultrasound wave is produced and traverses the medium as a mechanical wave. Ultrasound pressure waves are transmitted through particles in tissue as an alternating series of compressions (zones of high pressure) and rarefactions (zones of low pressure). The motion of the particles is influenced by two factors: the amount of energy in the emission and the forces of the restoring molecules (also known as the elasticity of the medium). For a spherical absorber of homogenous material, the characteristic PA signal is called an N-wave and serves as an example for many of the operating properties in the PA effect [44]. As mentioned previously, the temporal width between the positive and negative peak of a PA signal is proportional to the size of the absorber. Therefore, smaller objects will contribute to the higher frequency components of the PA signal. In the context of detecting pressure waves from ICH, higher-frequency components of the PA signal

will experience more attenuation from the skull than low-frequency components due to scattering, absorption, and diffraction [86]. Therefore, smaller ICH will be subject to a lower SNR because of attenuation induced by the skull. Nonetheless, according to [77] the ultrasonic scattering coefficient is 2-3 times less than the optical scattering coefficient for the same tissue.

In a study by Mohammadi *et al.* [55], the effects of the skull on PA signal detection are detailed. Firstly, the PA wave equation is modeled as follows:

$$\nabla^2 p(r,t) + (\tau(r)\frac{\partial}{\partial t}(-\nabla^2)^{\frac{y}{2}} + (\eta(r))(-\nabla^2)^{\frac{y+1}{2}})p(r,t) - \frac{1}{(c_0)^2(r)}\frac{\partial^2 p(r,t)}{\partial t^2} = \frac{-\beta}{C_v}\frac{\partial H(r,t)}{\partial t} \tag{1.3.10}$$

Where H(r,t) is a time-varying heat source and p(r,t) is a time-varying PA pressure wave at location r. c_0 is thermodynamic speed of sound, β is the thermal expansion coefficient, and C_v is specific heat capacity. Also, $\tau(r)$ and $\eta(r)$ describe the acoustic absorption and dispersion proportionality coefficients. y represents the power law exponent, which varies between tissues. It was shown through PA simulations and physical phantom image reconstructions that both skull thickness and proximity of the target absorber to the skull distort the waveform significantly in different ways. Mohammadi *et al.* (2019) note that the time shift in the first PA signal peak can be attributed to differences in the speed of sound in different tissues. Second, at the interface of inferior tissues and the skull, impedance mismatch caused acoustic wave reflection. Mohammadi *et al.* [55] conclude that acoustic reflection distorted the PA waveform by inducing ringing artifacts that may otherwise indicate inferior optical absorption. Finally, it is noted that heterogenous tissue interfaces produce bipolar asymmetry in the PA signal via conversion of shear waves to longitudinal waves and

vice versa. Overall, the average speed of sound in relevant tissue models simulating ICH is 1.5 mm/μs. In the simplest approximation, the depth of an absorber (d) with respect to a transducer can be calculated by a 1-dimensional velocity calculation:

$$d = v \cdot t \tag{1.3.11}$$

Where v is the speed of sound in the medium, and t is the time at which the transducer detected the first positive peak of the pressure wave. It should be noted that for an ICH model, the confined location of hematoma in the meninges will introduce many tissue interfaces that will distort any PA signals produced by pulsed laser excitation.

1.4 Piezoelectric Transduction and Resolution

Ultrasonic PA signals are detected using various arrangements of piezoelectric transducers. Transducers can either be arranged for single-element, 1-dimensional image reconstruction in PA tomography or PA microscopy, or multi-element arrays that can be used to produce 3-dimensional image reconstructions. In single-transducer implementations, reflection mode or transmission mode apparatus have been used in preclinical research, whether the transducer is located ipsilateral or contralateral to the light source respectively [68] [62]. Multi-element transducer arrays use principles of computed tomography to combine PA signals from many angles to produce 3D images with improved resolution [57].

For detecting ICH, Gao *et al.* [20] have shown the importance of picking an appropriate center frequency of the ultrasonic transducer in photoacoustic applications

as it relates to image resolution. Higher center frequency was shown to be related to the absorber's boundary information, and lower frequency was associated with the absorber's central information. Hence, the smaller the absorber size, the higher the frequency component. For instance, centimeter, millimeter, and a few hundred-micrometer absorbers generate ultrasonic waves in the $\sim$ 20 kHz - 300 kHz, $\sim$ 70 kHz - 2.5 MHz, and $\sim$ 400 kHz - 20 MHz range respectively. This implies that when the center frequency of the ultrasonic transducer is high, the imaging resolution will be higher, and that transducer choice depends on the resolution required for the application.

Piezoelectric transducers in a PA system convert the mechanical energy of the pressure wave to electrical energy. Considering the small amount of displacement that a pressure wave would generate, piezoelectric transducers offer viable methods of transduction for most ultrasound techniques. A piezoelectric transducer is distinguished by a highly pliable piezoelectric element surrounded by auxiliary layers and wiring [70]. Fundamentally, the piezoelectric effect works very similarly to a capacitive transducer, where the force applied results in a displacement value that is proportionate to the output voltage. A piezoelectric element is comprised of metal alloys and requires a natural polarity to produce an output voltage. When the element is deformed, a new charge difference is created within the dipole moment proportional to the magnitude and direction of the stress [48]. Due to the role of the dipole moment, the charge difference can produce a negative or positive current that will appropriately influence the output voltage.

To visualize the output voltage, Eqn. 1.4.1 summarizes the transducer transfer

function with which the force of a pressure wave is converted into an analog voltage value. In Eqn. 1.4.1, q represents the charge, C represents the capacitance, k represents the piezoelectric constant, ϵ_0 represents the dielectric constant of free space, and ϵ_r represents the relative dielectric constant of free space. The permittivity of free space, ϵ_0 (Farads/m), can be described as the proportionality between electric displacement (C/m^2) and electric field intensity in a vacuum (N/C). Electric displacement itself can be understood as the charge per unit area that would be displaced across a layer of conductor placed across an electric field. ϵ_r is the permittivity (Farads/m) of a different medium with magnitude determined relative to ϵ_0.

$$V = \frac{q}{C} = \frac{k \times \text{applied force} \times \text{distance separating plates}}{\epsilon_0 \times \epsilon_r \times \text{Area of Plates}} \tag{1.4.1}$$

A priority for preclinical ICH applications is matching the impedance of the transducer surface with the tissue model. For the same reasons that the skull distorts PA signals, the auxiliary material on a piezoelectric transducer, as well as the detector-tissue interface, must minimize environmental stress to focus on the signal of interest. For this reason, many PA imaging systems in preclinical and research trials use water baths to house tissue samples for optimal acoustic transmission [74]. Impedance is defined as having a real resistance value and an imaginary reactance value. Upon matching, the piezoelectric element can absorb the pressure wave with maximum penetration, filtering environmental noise before displacement occurs [54].

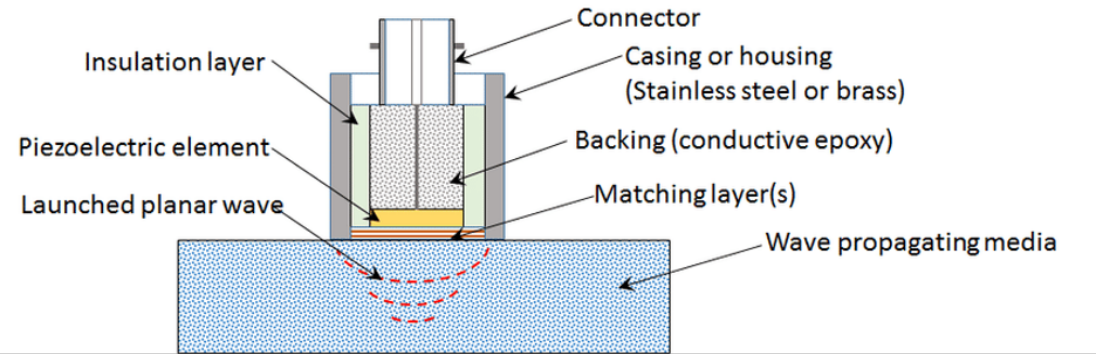

Figure 1.5: Schematic of a piezoelectric ultrasonic transducer cross-section showing various parts. Image adapted from [64].

There is also a backing material on the transducer that alters the resonance frequency of the piezoelectric element [4]. The resonance frequency of an element is defined as the frequency at which a material will vibrate at its highest amplitude. Accordingly, the natural frequency of objects is proportional to the square root of the material stiffness divided by the mass [86]. This relationship is important for piezoelectric users to consider so that a transducer is sensitive to expected external forces and not focused on noise. Furthermore, the resonant frequency of the transducer is related to image resolution. In the study by Gao *et al.* (2013) [20], it was found that absorbers used in PA tomography had a higher frequency component the smaller their size. This perpetuates the idea that the resonant frequency of the transducer must be application specific. If the size of the absorber requires a high resolution, then the center frequency of the piezoelectric element must also be relatively high. Gao *et al.* [20] note that because of this law, the frequency range of the signal input to the transducer can be anywhere from 20 kHz to 20 MHz for ultrasonic waves.

Therefore, to maintain high resolution when imaging hemoglobin and blood cells, relevant PA systems must resolve compounds at nm and μm scales respectively. Accordingly, piezoelectric transducers with a resonant frequency in the megahertz range are appropriate. According to a review by Wang and Hu [78], the achievable spatial resolution for most PA tomography systems is on the order of 1/200 of the desired imaging depth. Therefore, for detecting ICH across $\sim$ 1 cm of skull, the spatial resolution achieved would ideally be 50 μm. However, even using more sophisticated PA computed tomography techniques, [57] reports spatial resolutions of 800-900 μm when resolving a PA point source beneath an adult skull. Many preclinical applications of single-element PA tomography systems have been shown to image blood vessels and SpO_2 at depths past 1 cm [42] [68] [62] [82]. However, vessels imaged at these depths often exclude the skull from the tissue model or examine small animal or neonatal subjects.

To determine the resolution necessary for the detection of ICH, there are two factors that should be considered: First, the size of the average ICH, and second, the resolution of other imaging techniques used for ICH detection. As previously recorded by a study by Panchal *et al.* [61], small hematomas range in diameter from 1-2 cm. Using an expected target size as a reference, the necessary spatial resolution of proposed imaging systems should adhere to Nyquist sampling standards. The Nyquist criterion requires a sampling interval equal to twice the highest specimen spatial frequency [69]. Therefore, for a hematoma 1 cm in diameter, a minimum axial spatial resolution of 5 mm x 5 mm pixels should be sufficient.

In comparison to other popular modalities used for ICH detection, most standard head CT scans have pixel resolution of 0.5 mm x 0.5 mm within the axial plane [56]. SWI techniques used in transcranial MR applications have also been reported to have high-resolution capability. Using 3D gradient echo sequences with 1.5 T scanners, axial resolution is reported to be as low as 0.5 mm x 0.5 mm [26]. In one final comparison, NIRS has a considerably lower spatial resolution in transcranial applications. According to [72] and [33], the axial resolution of NIRS averages spatial resolutions of $\sim$ 1 cm x 1 cm.

1.5 Novel Application

In this thesis, the development of a multi-spectral PA imaging system is pursued to spatially resolve hematoma across a layer of skull tissue. Using specific wavelengths, optical contrast is derived between HHb and HbO to image relative SpO_2 of a tissue model in 3D. Simulations were conducted to ensure local optical fluence can be standardized between two incident wavelengths before image reconstructions are compared to discern relative SpO_2. Using a technique from pulse oximetry called the Red:NIR ratio, it is expected that the ratio of two PA images from a blood tissue sample will be larger for deoxygenated blood, than oxygenated blood. In this project, 2D raster scans for a co-axial laser/transducer were implemented in simulated and physical imaging environments. Also investigated in this thesis, was the prospect of free-hand probe tracking, using an inertial measurement unit (IMU) and optical mouse sensor.

While the use of PA imaging clinically has shown promise in research studies, Attia *et al.* (2019) [1] note the prerequisite of inter-system standardization before conclusions drawn from studies are considered valuable. The goal of this thesis is to contribute to the growing pool of PA implementations that confirm similar trends in different applications. Hopefully, attention and investment can be directed toward studies with large sample sizes and human subjects.

Chapter 2

Literature Review

PA imaging is an active area of research for a variety of clinical applications due to high ultrasound spatial resolution, as well as significant endogenous contrast. Since 1993, there have been 74,560 academic publications on PA imaging, and 5318 publications mentioning PA imaging and hemorrhage [15].

2.1 PA-based Models for Blood Oxygenation Measurement

In optical techniques, tissue oxygenation is the primary metric for identifying regions of ischemic/hemorrhagic stroke. In the NIR optical window, HbO and HHb have optical absorption coefficients at least one magnitude larger than those of other chromophores [45]. Tissue SpO_2 is calculated as the ratio of HbO to total Hemoglobin concentrations. Therefore, because of the linear relationship between optical energy absorbed and PA signal amplitude, there are also many methods used to extract tissue

SpO_2 from PA signals. In the most simple and popular method, linear spectroscopic inversion (LSI) assumes direct proportionality between PA signal amplitude and the optical absorption coefficients of relevant chromophores. Unfortunately, during least-squares regression, LSI does not account for the non-linear contribution of local tissue fluence to PA signal generation. As a result, measured PA signals can erroneously produce absorption spectra for chromophores during LSI [24]. Methods adopted to estimate local fluence for spectroscopic calculations include the Optical-Transport-based (OT-based) method, the Acoustic-Spectrum-based (AS-based) model, Statistic-Unmixing-based models, and the Eigenspectral Multispectral fluence model. In the following sections, OT-based and AS-based fluence approximations will be explored.

2.1.1 Linear-Model-based SpO_2 Measurement

LSI for SpO_2 estimation is a popular technique for SpO_2 measurement in PA imaging despite inherent inaccuracies. Li *et al.* (2018) [45] describe the LSI model using a series of equations that are solved to produce molar concentrations of HbO (C_{HbO}) and HHb (C_{HHb}). In Eqn. 2.1.1, a 2D PA image (P(λ_i,x,y)) at Cartesian coordinates x and y can be considered a linear combination of local optical fluence ($\phi(\lambda)$), the molar concentration (C) of any relevant chromophores, and those chromophores' molar extinction coefficients (ϵ):

$$P(\lambda_i, x, y) = \phi(\lambda)(\epsilon_{HHb}(\lambda_i)C_{HHb}(x, y) + \epsilon_{HbO}(\lambda_i)C_{HbO}(x, y)) \tag{2.1.1}$$

Where C_{HHb} and C_{HbO} are the molar concentrations of HHb and HbO at wavelength λ_i and ϵ_{HHb} and ϵ_{HbO} are the extinction coefficients of HHb and HbO at wavelength λ_i respectively.

To solve Eqn. 2.1.1 for C_{HbO} and C_{HHb}, multiple incident wavelengths can be used to produce PA images such that:

$$P = \begin{bmatrix} P(\lambda_1, x, y) \\ P(\lambda_2, x, y) \end{bmatrix} \tag{2.1.2}$$

where P is an array of measured PA images at multiple wavelengths, and,

$$\epsilon = \begin{bmatrix} \epsilon_{HHb}(\lambda_1) & \epsilon_{HbO}(\lambda_1) \\ \epsilon_{HHb}(\lambda_2) & \epsilon_{HbO}(\lambda_2) \end{bmatrix} \tag{2.1.3}$$

where ϵ is an array of the molar extinction coefficients for HHb and HbO at each wavelength. Once the data is collected, LSI can be used to determine C_{HbO} and C_{HHb} through regression analysis.

i.e

$$\begin{bmatrix} C_{HHb}(x, y) \\ C_{HbO}(x, y) \end{bmatrix} = (\epsilon^T \epsilon)^{-1} \epsilon^T P \tag{2.1.4}$$

Although many LSI implementations normalize values for incident light energy, the assumption that local optical fluence is equal between wavelengths is not accurate. As the depth of target tissue increases, the effect of tissue optical properties on local fluence changes more dramatically between wavelengths.

In a study by Li *et al.* (2008) [52], PA-based LSI was used to image Hb SpO_2 in mouse brain tumour neovasculature. Two transducers were used to detect PA signals at 120 different positions in 360° about the transverse plane of the mouse head. At each of the 120 positions, four incident wavelengths were used to produce PA signals: 764 nm, 784 nm, 804 nm, and 824 nm. In Fig. 2.1, resultant SpO_2

and total Hb images are displayed as calculated using LSI. In Fig. 2.1, the tumor location is indicated by the red arrow, seen pointing towards the right hemisphere of the mouse brain.

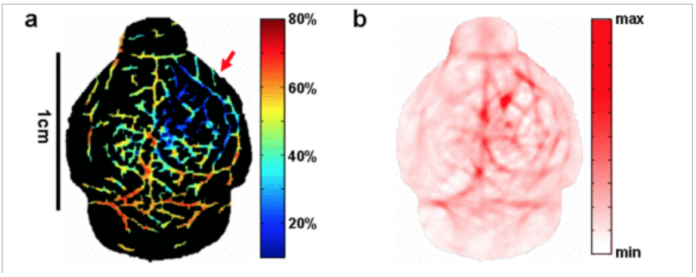

Figure 2.1: SpO_2 (left) and Total Hb (right) PA images adapted from [52].

Li *et al.* (2008) were able to reconstruct the SpO_2 image by segmenting the vasculature from the background using local total Hb measurements. The resultant SpO_2 and total Hb measurements from the *in vivo* model were not compared to known values to determine accuracy. Instead, PA images are compared to planar fluorescence images of exogenous label IRDye800-c(KRGDf), a peptide known to bind to proteins associated with tumor angiogenesis. Using both imaging techniques, tumor regions were correlated with areas of hypoxia (low SpO_2) and areas of angiogenesis (high total Hb concentration). Although the size of the mouse brain does not affect local fluence differences as much as a larger object would, Li *et al.* (2008) [52] still fail to acknowledge the shortcomings of local fluence approximations during SpO_2 quantification.

2.1.2 Optical Transport-based Fluence Approximation

Optical-Transport-based (OT-based) fluence approximation is a method used to enhance linear spectral fitting techniques. OT-based fluence approximation uses Eqn. 1.3.9 as a function of wavelength to estimate local fluence throughout an entire tissue model. In a study by Laufer *et al.* (2006) [41], OT-based fluence approximations is used to scale PA signals after tissue types in the object are segmented and literature values for μ_a and μ_s are assigned. Another way to convey a PA wave equation is as follows (Eqn. 2.1.5):

$$P(\overrightarrow{x}, \lambda) = \Gamma \mu_a(\overrightarrow{x}, \lambda)\phi(\overrightarrow{x}, \mu_a(\overrightarrow{x}, \lambda), \mu_s(\overrightarrow{x}, \lambda)) \tag{2.1.5}$$

Where P is the PA signal amplitude at 3D location $\overrightarrow{x}$ using wavelength λ, Γ is the Grunesian parameter, and ϕ is the local optical fluence. Therefore, where LSI fails to account for differences in molar extinction at depths, OT-based fluence approximation can more accurately determine C_{HbO} and C_{HHb} during regression analysis (Eqn. 2.1.4). In the study by Laufer *et al.*, resultant PA signal amplitudes from blood samples with varying SpO_2 were plotted as a function of wavelength. Afterward, the fluence-corrected amplitudes were fit to these data to recover the concentrations of HbO and HHb along with estimates of SpO_2. Laufer *et al.* report that HbO and HHb measurements varied by $\pm$ 3.8 g/l and $\pm$ 4.4 g/l respectively. One drawback to the use of OT-based fluence approximation is that for complex tissue models *in vivo*, segmentation of tissue boundaries can become oversimplified.

2.1.3 Acoustic Spectrum-based Fluence Approximation

The last method to be explored that approximates fluence during PA imaging is acoustic-spectrum-based (AS-based) fluence approximation. AS-based fluence approximation uses the frequency spectrum of a detected PA signal to define the relationship between signal frequency ($S(\omega)$) and local optical fluence ($F(\lambda_1)$). Specifically:

$$S(\omega) = F(\lambda_1)O(\omega)H(\omega)a(\omega) \tag{2.1.6}$$

Where $O(\omega)$ is the object frequency spectrum, $H(\omega)$ is the system frequency response distribution, and $a(\omega)$ is the acoustic attenuation factor. If multiple incident wavelengths are used, the ratio of the signal frequency spectra can be written as follows:

$$\frac{S_1\omega}{S_2\omega} = \frac{F(\lambda_1)\sqrt{(\frac{\omega}{\mu_{a2}})^2 + c^2}}{F(\lambda_2)\sqrt{(\frac{\omega}{\mu_{a1}})^2 + c^2}} \tag{2.1.7}$$

Where c is the speed of sound in soft tissue. According to Guo *et al.*[25], the reduced scattering coefficient is neglected because the anisotropy factor is close to 1 in blood for the wavelength used (around 585 nm). To obtain the absolute values of $F(\lambda_1)$, $F(\lambda_2)$, μ_{a1} and μ_{a2} using the acoustic spectra, the data is fit to Eqn. 2.1.7.

In the study by Guo *et al.* [25], a 1 mm x 1 mm section of a mouse ear was imaged with 2 optical wavelengths (561 nm and 570 nm). Then, the absorption coefficients and the incident fluence ratios were quantified from the acoustic spectral ratios. Guo *et al.* report that when AS-based fluence approximation is ignored, calculations of SpO_2 values become "inaccurate" by 8-11%.

It should be noted that for AS-based fluence approximation, PA microscopy must be used. This is because in order to derive Eqn. 2.1.7, an objective lens must focus the incident laser beam so much that the "optically homogenous" blood vessel can be assumed to have a flat surface in relation to the beam diameter. Hence, one flaw with AS-based fluence approximation is that when target blood vessels become smaller or find themselves at greater depths, Eqn. 2.1.7 becomes inaccurate.

2.2 Current Preclinical PA Imaging Applications

During this short literature review, recent conclusions drawn by other studies can validate the potential of the PA system used in this project, as well as outline expected limitations. There are many preclinical and clinical studies acquiring images of blood tissue using PA systems. It should be noted that for preclinical and clinical studies that claim to estimate oxygen saturation for PA scan data, failure to account for local optical fluence should be identified as a caveat.

In 2010, a pulsed laser was used with 800 nm light to image breast vasculature up to 40 mm beneath the tissue surface [40]. Using a hemisphere array of 128 piezoelectric transducers TOF backprojection reconstruction algorithms were used to produce maximum intensity projections (MIP) of blood vessels less than 1 mm in diameter (Fig. 2.2). By modifying a pre-existing small-animal PA imaging system, Kruger *et al.* [40] were the first to obtain sub-millimeter spatial resolution images of breast vasculature without the use of contrast agents.

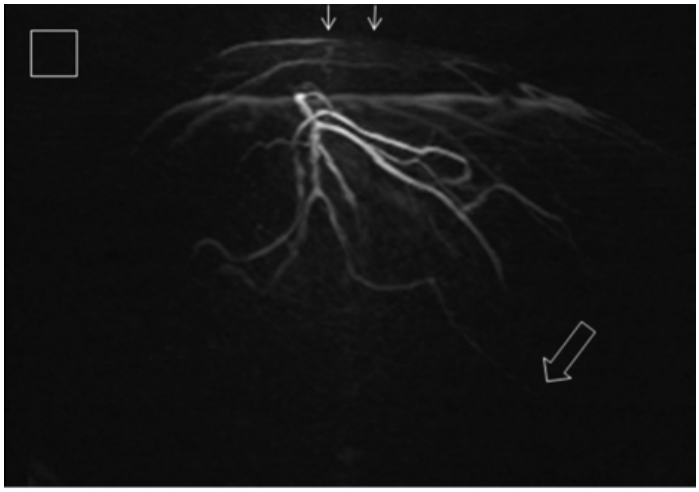

(a)

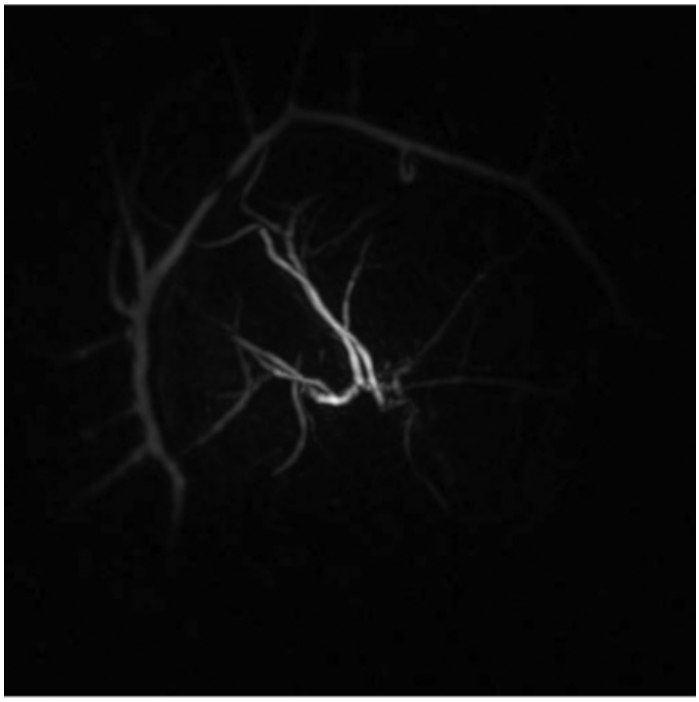

(b)

Figure 2.2: PA Angiography MIP of a patient's left breast a) Lateral projection b) Anterior-Posterior projection. PA images adapted from [40].

Ultimately, the ability of PA imaging to derive contrast in the tissue model without the use of contrast agents can be attributed to the absorption spectra of Hb in the NIR region. As summarized by Kruger *et al.* (2010) [40], the absorption coefficient of whole blood (150 g Hb/l) is $\sim$ 17 times that of the surrounding breast tissue. According to [40], operating a laser at 800 nm with a 10 Hz repetition rate and pulse energy of 20 mJ/pulse offers a valid solution for imaging blood vessels <1 mm in diameter. For the purpose of this project, it is expected that an ICH tissue model would offer a lower SNR due to an increase in scattering between the light source and the target tissue. Therefore, the contrast and imaging depth achieved by Kruger *et al.* is not assumed to be feasible for the experiments in this thesis.

Further signal transduction methods have been proposed to exploit superior spatial resolution when imaging hemoglobin. Zhang *et al.* (2009) [88] cite issues with the implementation of piezoelectric transducers in reflection mode PA imaging systems. Zhang *et al.* argue that opaque detectors, and a detector element size larger than the acoustic wavelength limits spatial resolution. By replacing piezoelectric transducers with a transparent Fabry-Perot polymer interferometer, 100 μm spatial resolution was achieved in 3D images of skin and subcutaneous tumour vasculature at depths up to 5 mm.

In transcranial applications, Shan *et al.* (2023) [66] conducted 3D PA imaging and SpO_2 quantification of neonatal mouse brains for the detection of ICH. PA tomography images of neonatal mice brains were obtained and then compared to images of the same subjects after collagenase was injected to induce hemorrhage. Lesion-to-Brain size ratios were quantified and tracked alongside SpO_2 in the lesion. Shan *et al.* report a spatial resolution of 105 μm up to 5 mm in depth, but also acknowledge

the discrepancy in thickness between the skull of neonatal mice and other *in vivo* models. Nonetheless, Shan *et al.* report the first whole-brain dynamic assessment of hemorrhage SpO_2 in the neonatal brain. Notably, Shan *et al.* use a custom cylindrical piezoelectric transducer array to optimize aperture angle, as well as consider local optical fluence with respect to wavelength when quantifying SpO_2. Wavelengths of 780 nm and 850 nm were used to irradiate the mouse brain, and LSI was used to create the ratio of HbO to total hemoglobin. In Fig. 2.3, tomographic images can be seen relative to corresponding histological slices.

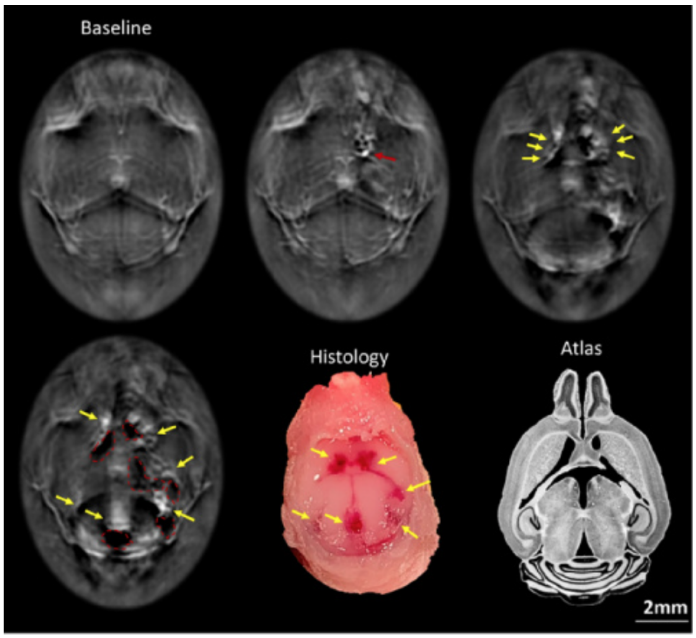

Figure 2.3: Tomographic PA images at the same depth over time. The red arrow denotes the location at which the collagenase was injected, and yellow arrows denote hematoma. Areas encircled by a red, dashed lines denote low optical absorption. Images adapted from [66].

Using the tomographic images, Shan *et al.* [66] are able to track the size of the lesions produced by dividing the number of pixels represented by low absorption, by the number of pixels in the entire brain area.

Finally, Kang *et al.* (2021) [37] used slightly more complex *in vivo* models to measure SpO_2. In this model, stroke lesions are induced in the posterior cortex of anesthetized piglets using a photothrombotic technique. Transcranial PA images were obtained *in vivo* within 2 h from the stroke onset using a range of incident light in 10 nm intervals from 700-900 nm. Brain SpO_2 images were able to provide a statistically significant difference in oxygen saturation calculations between regions of interest and control regions. However, in all stroke models, there were insignificant decreases in HbO and total Hb concentrations between regions of interest and control regions. Concentrations were calculated using an LSI method, and the mean spectral attenuation was measured *ex vivo* and compensated for before the spectral-unmixing process [36]. Still, Kang *et al.* speculate that discrepancy may have been presented due to many reasons. First, inconsistent distance and angle between a detector and a tissue sample would affect light fluence and acoustic attenuation, skewing the estimation of hemoglobin concentrations using LSI. Second, inducing stroke in vivo using photothrombosis may also "trap" blood cells in the clot, leading to inconsistent decreases in total hemoglobin concentrations as opposed to embolic stroke models. Overall, Kang *et al.* offer support for the use of SpO_2 intensity maps for the diagnosis of thrombotic stroke 3 mm below a 5 mm neonatal skull.

While tested in many different capacities, spatial resolution and penetration depth remain a challenge for transcranial applications of quantitative PA imaging. Still, the prospect of a clinically relevant non-ionizing, non-invasive imaging technique for ICH is encouraged by the results of many preclinical experiments.

Chapter 3

Simulations

After treating traumatic brain injury, monitoring blood oxygenation (SpO_2) below the skull is crucial for the early detection of secondary injuries such as ICH. To obtain these data in a point-of-care setting, PA imaging observes optical contrast between hemoglobin (Hb) species by measuring ultrasonic waves emitted by a section of optically irradiated tissue.

In the first stage of this project, PA image acquisitions of various tissue models are tested in a computer simulation environment. Using MATLAB-based software toolkits, *mcxyz.c* and *k-wave*, a co-axial laser/transducer system was modeled and the PA process simulated to deposit pulsed light energy into a 3D tissue model along with detected resultant PA signals. Raster scans were conducted in 2 dimensions so that 1-dimensional PA signals (analogous to A-line ultrasound signals) could be reconstructed into images of the tissue models at certain depths. Two novel approaches to the PA imaging procedure used by Jain Mandakini [34] were tested using simulation software. The first technique was the Red:NIR ratio technique for producing contrast between differing levels of blood SpO_2. The tissue models imaged in simulations

contained various tissue types as well as different blood SpO_2 values with appropriate optical properties. The second technique includes various signal post-processing techniques to enhance the quality of the images. Although the geometries of tissue imaged during simulations were created to mimic ICH as accurately as possible, there are limitations to be considered when drawing conclusions with the simulation data. A few limitations that should be identified are as follows:

Firstly, the PA signals detected using *k-wave* do not include any background noise that can be expected from a physical PA system. Second, the tissue optical properties in the *mcxyz.c* library are assumptions of homogenous tissue concentrations within each voxel. Finally, the light source modeled using *mcxyz.c* is an assumption of a perfectly collimated beam consisting of one predetermined wavelength and exactly one million photons.

3.1 PASimulate

PASimulate is a program that simulates PA image acquisition. PASimulate uses two MATLAB toolboxes named *mcxyz.c* and *k-wave*. Using the toolboxes, PASimulate facilitates the acquisition of PA signals using a co-axial laser/transducer apparatus at predetermined positions over a 3D tissue model in a raster pattern. To use PASimulate, the user must input the wavelength of light to be used, as well as up to two oxygenation levels which can characterize any blood tissue used in the model. Depending on the step size chosen for the raster scan, PASimulate produces a 3-dimensional array containing the time-resolved PA signals. For the following simulations, signals are acquired across a 40 mm square in 2 mm increments, producing data analogous to measurements from a physical laser system.

3.2 *mcxyz.c*

mcxyz.c uses a Monte-Carlo probability system to track the deposition of photons in a user-generated 3D tissue model. At each interaction location within the tissue model, the Monte-Carlo method predicts a photon step size and anisotropy of scatter using a library of optical properties for the tissue model. The Monte-Carlo method used by *mcxyz.c* is also called the hop-drop-spin method which includes a few stages of calculation. Photons are launched in *mcxyz.c* with a certain weight and trajectory, and at the first stage of the hop-drop-spin algorithm, a random step length is generated to move the photon within the starting medium. If the photon encounters a different medium, reflection and refraction calculations update the initial displacement value. When a photon interacts, a fraction of the photon's weight is lost according to the absorption coefficient of the interaction voxel. If the weight of the photon decreases below a certain threshold following absorption, the photon either dies or increases its energy to repeat the earlier phases according to laws of energy conservation [87].

In this project, the first input to *mcxyz.c* is a 3D tissue model that the user generates with a program from *mcxyz.c* called *make_model*. The second input to *mcxyz.c* is the number of photons that will be simulated in the tissue model. Upon completing the raster scan, *mcxyz.c* outputs the spatial distribution of absorption in 3-dimensional space for each location scanned in the tissue model. The "Absorption Map" is obtained by multiplying the relative fluence of photons [W/cm^2 per total W delivered] at a voxel in the tissue model by the absorption coefficient (μ_a [cm^{-1}]) of the tissue in each position (Fig. 3.1).

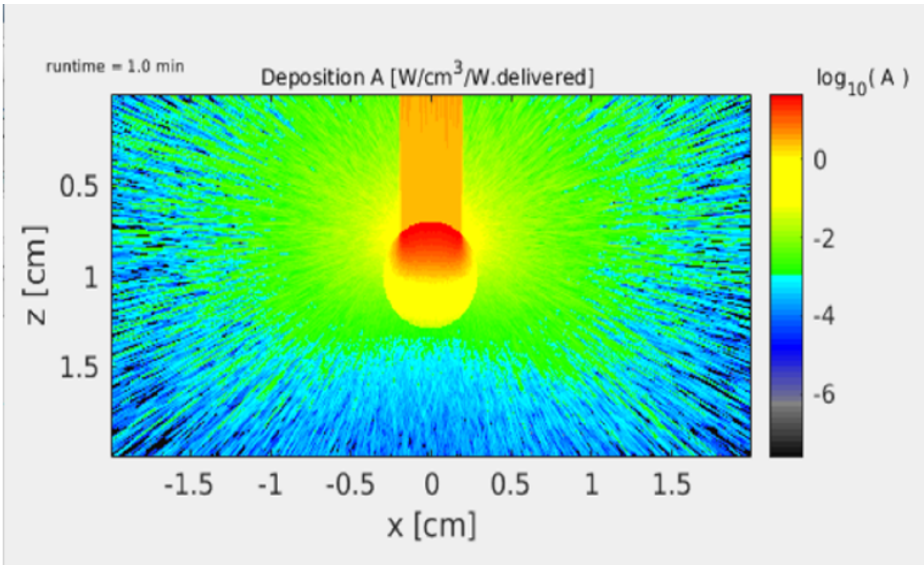

Figure 3.1: Absorption map from Monte-Carlo simulation of 1000000 photons deposited in the centre of a blood vessel with 95% oxygenation.

As mentioned previously, the output from *mcxyz.c* is a spatial distribution of absorption, or a 3D "absorption map". The absorption map output from *mcxyz.c* is then converted into an initial pressure distribution (IPD) once input to the following program, *k-wave*. Because optical power deposition and pressure values are proportional, values from the absorption map ($\mathrm{W}/cm^3/W_{\mathrm{delivered}}$) are redefined as initial pressure values with arbitrary units. Using the IPD, *k-wave* performs a time-domain simulation of detected acoustic waves in 3D space. In this project, the 3D absorption map acts as the acoustic source of the ultrasound waves which will be recorded as PA signals.

3.3 *make_model*

make_model is part of the *mcxyz.c* toolbox which lets the user establish the parameters of the tissue model which will be simulated. *make_model* produces a 3D array in which the value of each index references a tissue with a specific set of optical properties. *make_model* has the user define the geometry of different tissues as well as the laser beam width, shape, and source location. For this project, the beam has a radius of 2 mm to irradiate the tissue model at an initial direction orthogonal to the x-y plane. The raster scan steps then take place between signal acquisitions in the x and y directions.

In this project, 3 categories of tissue models have been used to create images and draw conclusions relevant to the thesis. The first model is called the simple model, in which a geometry of blood is suspended in water. Two different simple model blood geometries were scanned: a cylindrical blood vessel with 3 mm radius positioned along the y-axis and an ellipsoid blood geometry 2 cm wide (x-axis), 1.2 cm long (y-axis) and 0.6 cm tall (z-axis). The second model is called the complex model, in which 1 mm of dermis and 4 mm of skull is placed above each blood geometry. Finally, the hematoma model describes a semi-ellipsoid of blood resting on layers of brain tissue below 1 mm of dermis and 5.5 mm of skull. In Fig. 3.2 and 3.3, xz-plane cross-sections of the various tissue models are displayed with incident light beams illustrated.

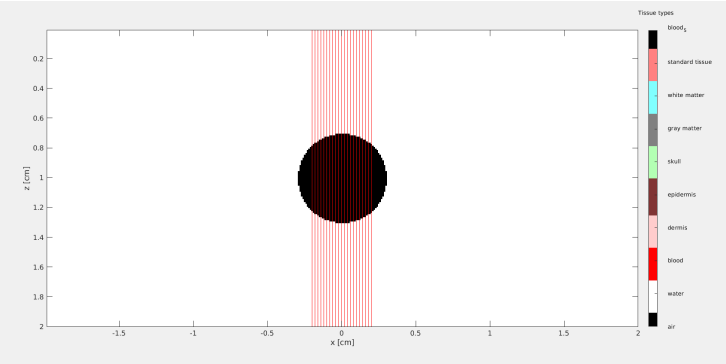

(a) simple model of a blood vessel with 5% SpO_2 in water; 40mm long (y-axis), 3 mm radius.

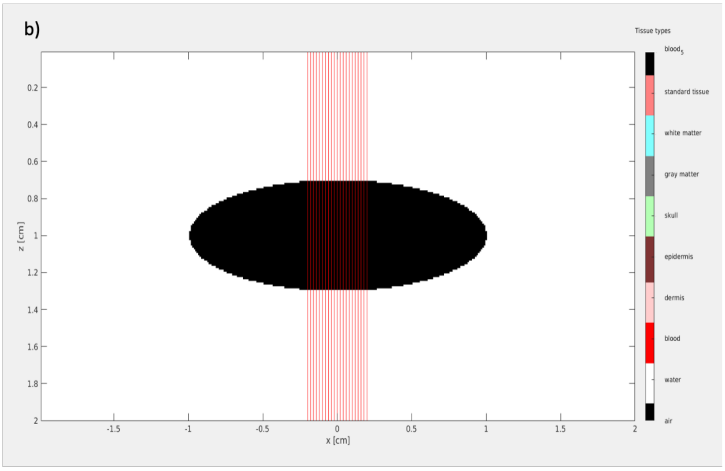

(b) simple model of an ellipsoid with 95% SpO_2 in water, 2 cm wide (x-axis), 1.2 cm long (y-axis), 0.6 cm tall (z-axis).

Figure 3.2: xz-plane cross-sections of "Simple" 3D tissue models created using *mcxyz.c* software

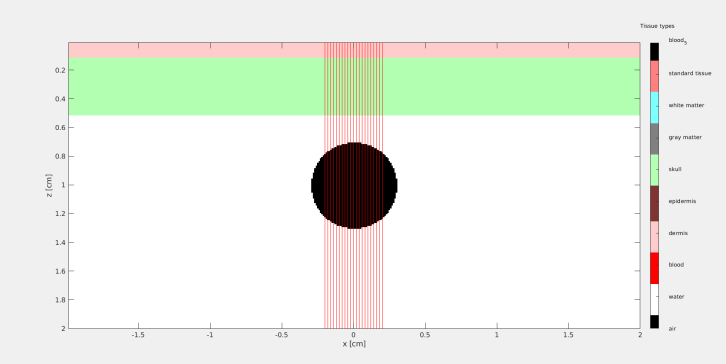

(a) Complex tissue model consisting of a blood vessel with 5% SpO2 beneath 4 mm of skull and 1 mm of dermis.

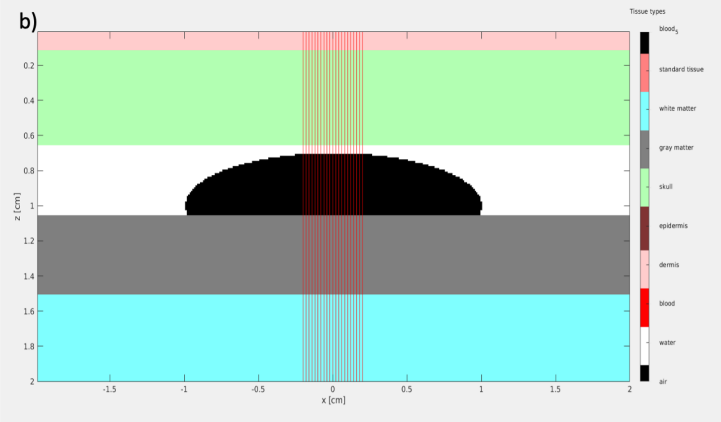

(b) Complex tissue model of hematoma consisting of a "semi-ellipsoid" blood geometry with 5% SpO_2 positioned beneath 5.5 mm of skull and 1 mm of dermis resting on 4.5 mm of gray matter and 5 mm of white matter.

Figure 3.3: xz-plane cross-sections of "Complex" 3D tissue models created using *mcxyz.c* software

3.4 *makeTissuelist*

makeTissuelist is a program that loads the absorption spectra [cm^{-1}] of various tissues across a number of wavelengths (lambda [nm]) from 300 to 1000 nm. The tissues for which these absorption coefficients are recorded include oxygenated blood (150 g of Hb/Litre), deoxygenated blood, water, fat, and melanosomes. Using this library, a data structure is created to include the name of a tissue, as well as coefficients that describe the absorption, scattering, and anisotropy of scattering of photons at the defined wavelength. By default, *makeTissuelist* provides optical parameters for air, water, blood, dermis, epidermis, fat, skull, white and gray matter. For this project, extra tissue types are added which correspond to percentage levels of SpO_2 in blood. To derive the absorption spectra for various blood SpO_2 levels, each optical parameter of oxygenated whole blood is multiplied by the percent SpO_2 defined by the user. The second alteration made to this code was made after discovering that there were differences in PA signals at different wavelengths due to increased absorption of NIR light by water. Because this project focuses on using the PA effect to determine blood SpO_2, the absorption coefficient of water was hard-coded to remain at 4.52×10^{-3} cm^{-1}, the μ_a of water for 680 nm light.

3.5 *hemascan/k-wave*

The second stage of the PA imaging simulation is the detection of PA pressure waves as they are emitted from the tissue model. To obtain a time-domain PA signal, a MATLAB toolbox called *k-wave* asks to user to define an acoustic source and a binary transducer mask which will be enclosed in a computational grid. For this project, the

source is characterized as an initial pressure distribution (IPD) map, most appropriate for users wanting to simulate pulsed PA tomography [2]. An IPD map is chosen as opposed to time-varying sources. Choosing to define an IPD inherently employs certain governing equations which dictate the conservation of mass, momentum, and energy during acoustic wave propagation within the medium. Of interest to this project, IPD equations allow for the use of a special anisotropic layer (known as a perfectly matched layer or PML) for absorbing the acoustic waves when they reach the edges of the computational domain.

Positioned at the top of the computational domain is the transducer mask. In this project, a ring-shaped transducer is modeled by a pixelated sensor mask with an outer diameter of 1 cm and an inner diameter of 6 mm comprised of 5032 pixels, each comprising a transducer element. Each binary transducer element within these radii detects and records the resultant PA signals at each (x,y) position during a raster scan. Although each binary element will record a PA signal, the resultant waveform is a sum of all elements. This means that the final PA signal will display a pressure wave with peaks averaged in time as they arrive at various transducer elements on the ring (Fig. 3.4).

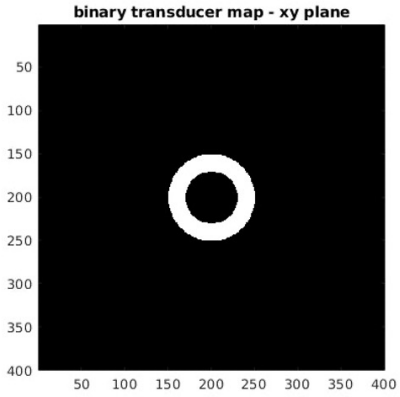

Figure 3.4: Binary image map of transducer modelled using *k-wave* in the xy-plane.

Other user-defined parameters in *k-wave* that affect the output include the recording time, the speed of sound in the medium, as well as the center frequency and percent bandwidth of a Gaussian frequency response for the transducer. For this project, the simulation records for 25 μs, the center frequency is 3 MHz, the percent bandwidth is 80% and the speed of sound in the medium is 1.5mm/μs. It should also be noted that the ambient density distribution within the medium (kg/m^3) was left undefined, meaning that the acoustic wave propagation occurs in a lossless medium.

The output of *k-wave* displays a time-domain PA signal across the predetermined number of time points. Each data point along the t-axis represents 0.1 μs, while the amplitude plotted on the y-axis is measured in arbitrary units. The magnitude of each data point represents the sum of the acoustic pressure values recorded by all sensor elements. It is expected that, according to the speed of sound in soft tissue/water, simulations scanning blood tissue located 7 mm below the transducer should produce a PA peak at $\sim$4.666 μs. For subsequent experiments, the absorption spectra of oxygenated blood (HbO) and deoxygenated blood (HHb) seen in Fig. 1.2 convey

features fundamental to the experimental design. Particularly, HbO and HHb absorption spectra have an isosbestic point at around 810 nm. Therefore, by irradiating a section of tissue with light of wavelength less than 810 nm, deoxygenated tissue is expected to produce larger PA signals than oxygenated tissue. The opposite is then expected when the same tissue is pulsed with light of wavelength greater than 810 nm. Simulations scanning all tissue models recorded PA signal amplitudes confirming that oxygenated blood preferentially absorbed IR light compared to red light. For this project, HHb is modeled as 5% SpO_2 and HbO is modeled as 95% SpO_2.

3.6 Formula of Best Fit

Using the simulation data, as well as a technique called the Red:NIR ratio, information about expected SpO_2 values can be extracted from raw PA signals. The Red:NIR ratio is commonly used in pulse oximetry in which resultant AC and DC signals from simultaneous light pulses can be compared to extract SpO_2 information [67] [30]. In both pulse oximetry and PA tomography, pulsing the same location with red light then NIR light, and dividing the two resultant signals respectively, conveys the inverse correlation between ratio amplitude and SpO_2 magnitude. This is expected according to the absorption spectra of HbO and HHb because, as the wavelength of light increases, HbO begins to dominate absorption. In this project, a curve of best fit was produced from simple vessel model simulation data to observe the expected Red:NIR ratio as SpO_2 increases. For wavelengths of 680 nm and 990 nm, arrays of PA signals were recorded at 15% SpO_2 intervals, from 5-95%. For each SpO_2 level, the 680 nm array was divided by the 990nm array, and the maximum ratio was calculated at an (x,y) location known to be representative of the blood vessel.

Least-squares regression is then performed on the ratio data to produce coefficients for a second-degree polynomial function representing the relationship between Red:NIR ratio amplitude and blood SpO_2. This formula is useful when scanning a tissue sample with unknown SpO_2, where the Red:NIR ratio can be determined and the resultant SpO_2 found. It should be noted that this formula may only hold true for identical tissue models for two fundamental reasons. First, in other tissue models, the patterns of scattering and absorption will vary greatly according to tissue geometry. Second, when using a physical PA imaging system, errors from system hardware can alter signal strength over time.

3.7 *butterimage*

To produce images using simulation data, a custom MATLAB program called *butterimage* processes the raw data before displaying 2D images of the tissue model at different depths. Each pixel in the reconstructed images has an amplitude according to the average Red:NIR ratio between two light pulses across the specified depth. For this project, average ratio values across intervals of 10 time points (1.5 mm in depth) are represented by each pixel.

In simple tissue models, PA signal arrays from raster scans using 680 nm light are used for the red-light data and scans using 990 nm light are used for NIR light data. According to the absorption spectra in Fig. 1.2, these wavelengths exploit one of the highest differences in absorption coefficients between hemoglobin species, while staying in the biological optical window. At wavelengths shorter than 650 nm, the absorption coefficients of other tissues such as bone increase dramatically. At wavelengths longer than 1000 nm, absorption of incident light by water dominates

any absorption by blood. However, in complex tissue models, the superficial layers of dermis and skull tissue absorbed the chosen wavelengths very differently. To obtain the most accurate information about SpO_2 from the Red:NIR ratio in complex simulations, the absorption coefficients of dermis and skull tissue for the wavelengths chosen must be as similar as possible. This way, the optical fluence reaching the target tissue is the same between wavelengths, validating the use of optical contrast in image reconstruction. The only restriction to the wavelength selection process is that the two wavelengths chosen remain on opposite sides of the isosbestic point of oxygenated and deoxygenated hemoglobin. Therefore, for complex tissue models, a "red wavelength" of 750 nm was used and a "NIR wavelength" of 850 nm was used.

The first step in processing the PA signal arrays before image reconstruction was to filter high-frequency noise from the data using a low-pass Butterworth filter. A Butterworth filter allows for the isolation of low-frequency peaks known to represent tissues of interest. In this project, a 12th-order filter is applied with a cut-off frequency of 4 MHz. The 4 MHz cut-off frequency limits the spatial resolution of the signals to 0.375 mm in the depth domain.

Once the signals are smoothed of noise, complex tissue models required the artificial scaling of PA signals from 750 nm light due to a remaining difference in absorption in layers of skull and bone. To scale the red-light signals, a scaling factor is calculated by taking the Red:NIR ratio of the PA data across all (x,y) locations for the first 30 data points of the tissue model. The 30 data points represent the acoustic signal produced by absorption in the first 4.5mm of the tissue model, occupied by the layers of dermis and skull tissue. By dividing the first 30 data points of the red-light signals by these ratios, the signal is made to be equal between the two wavelengths in the

superficial tissue layers. Next, to scale the fluence of red light past these superficial layers, a second scaling factor is calculated with the Red:NIR ratio using the remaining 220 data points of both signals. However, the second scaling factor averages the ratio produced by signals at locations where the vessel is not present, thus presenting the same assumed absorption for both wavelengths. This way, any fluence lost for reasons other than absorption in the blood vessel can be compensated for. The last 220 data points in red light signals are divided by the second scaling factor at every (x,y) location.

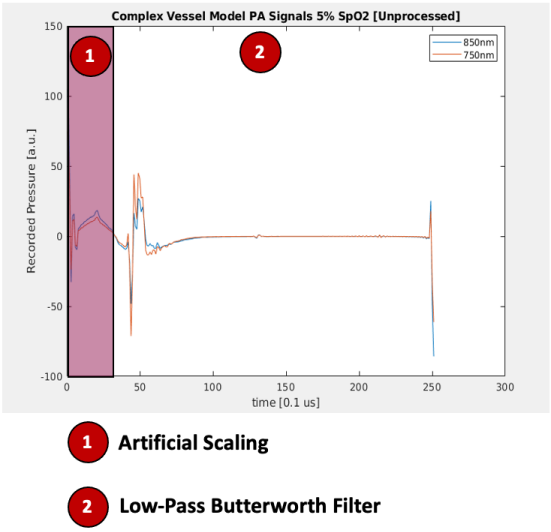

(a) Complex Vessel PA signals before processing

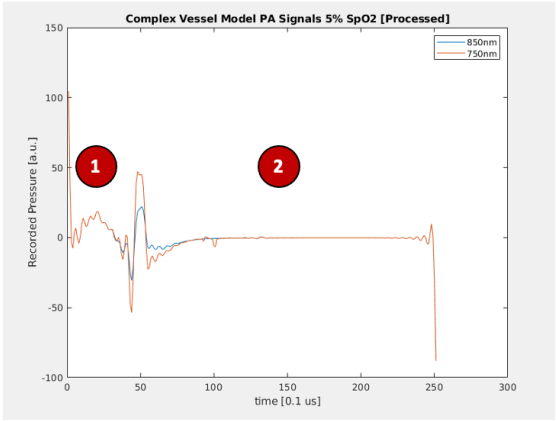

(b) Complex Vessel PA signals after scaling and filtering

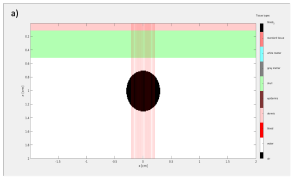

(c) Complex Vessel tissue model cross-section

Figure 3.5: Representative PA signals pre- and post-processing

Finally, the absolute value of each PA signal is taken as input for calculating the Red:NIR ratio array. It was found through simulations that some time points contained ratio values far greater than expected. For reference, in simple vessel model simulations, the maximum Red:NIR ratio recorded using 680 nm and 990 nm light was calculated to be 5.6328, specifically present in tissue models with 5% SpO_2. Therefore, when a PA signal produces one time point with a ratio greater than 5.6328, that ratio's influence on the pixel value can skew image resolution for reasons other than optical contrast. Therefore, before 2D images are reconstructed, any ratio value above 6 is truncated. The value of pixels displayed in the following images represent the log_{10} of the average Red:NIR ratio across 1.5 mm of depth.

Chapter 4

Experimental Validation

In this project, the simulation results are validated by developing a physical PA system to image similar tissue phantoms. The imaging phantoms consisted of tissue-mimicking materials that replicated ICH conditions in increasing complexity. 2-dimensional raster scans of phantoms were conducted using two wavelengths, each on either side of the hemoglobin isosbestic point. Red:NIR ratio images were then produced to confirm that contrast can be produced in PA images based solely on differences in optical absorption. To achieve this, the PA system developed required the installation of an optical parametric oscillator (OPO) for multi-spectral tuning. Finally, signal processing techniques similar to the simulation procedure were employed to ensure that contrast derived in images could be used as evidence of optical contrast.

4.1 Preliminary Setup

In the first PA apparatus, an Opotek VIBRANT 355 II laser system was used to generate different wavelengths of light from an Nd:YAG $BRILLIANT^{TM}$ pump laser (Fig. 4.1). By using up to 3 harmonic generators and a polarizer, PA data could be acquired using wavelengths ranging from 530nm to 1001nm. The laser pump repetition rate is 10 Hz with a pulse width of 5 ns. Quality factor, Q, is defined as the ratio of energy stored in the laser cavity to the energy loss per cycle [39]. Therefore, the higher the quality factor, the lower the energy loss. During Q-switch light emission, energy is stored in the flashlamp while Q is low to prevent laser emission. After enough energy has accumulated, a high cavity Q value is restored, and the accumulated energy is suddenly released in the form of a very short pulse of light (5 ns). After a flashlamp pulse is released by the $BRILLIANT^{TM}$ laser, the $Arrow^{TM}$ OPO was used to output wavelengths in a range from 400 – 2400 nm. According to the $Arrow^{TM}$ OPO tuning curve on the VIBRANT datasheet (Fig. 4.2)[73], the expected peak average pulse energy is output at $\sim$ 450 nm with 30 mJ/pulse. Before all imaging acquisitions, an ASEQ LR1-B spectrometer and Thorlabs PM400 optical power meter were used to sample light output by the laser/probe in order to determine the emitted power at relevant wavelengths.

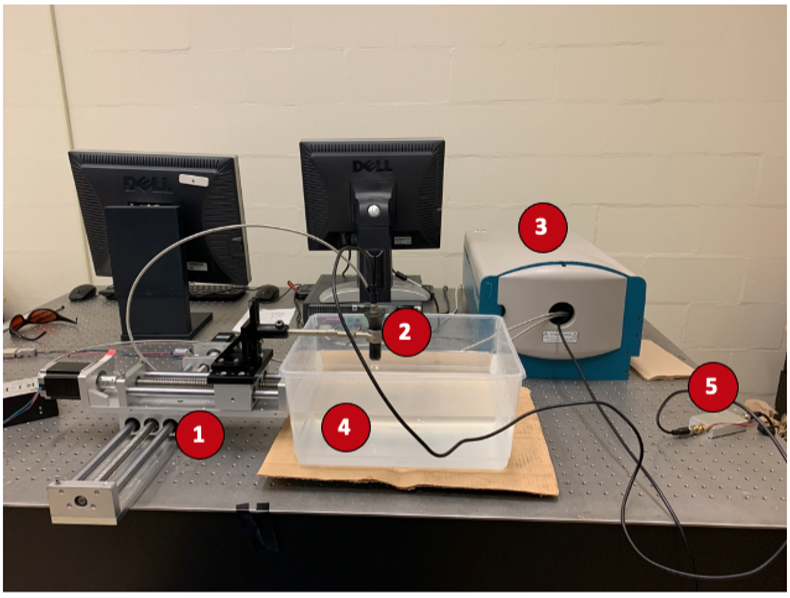

Figure 4.1: Preliminary PA Imaging System

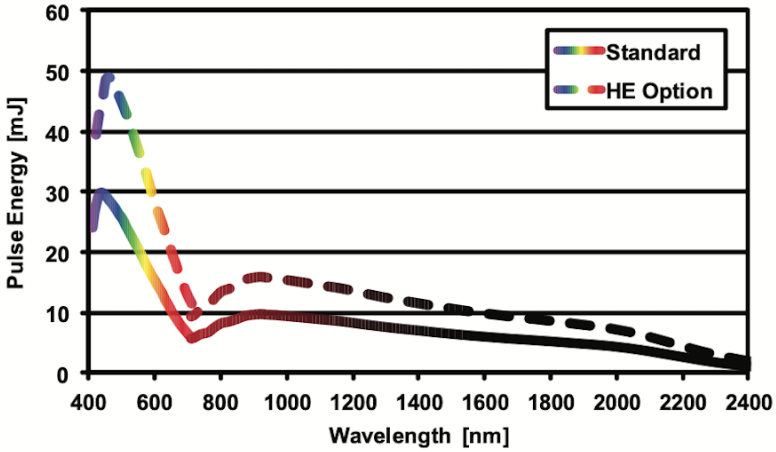

Figure 4.2: $Arrow^{TM}$ OPO Tuning Curve [73]

As seen in Fig. 4.1, the pulsed laser light is focussed into a Thorlabs high-power optical fiber leading from the VIBRANT system to the PA probe. The function of the PA probe is to house both the optic fiber output as well as the ring-shaped piezoelectric transducer responsible for PA signal detection. The probe is made from $Formlabs^{TM}$ black plastic resin and is held by metal clamps that position the probe orthogonal to the surface of the image phantom housing. Finally, signals detected by the transducer are transmitted from the probe toward an ultrasonic pre-amplifier, then subsequently digitized. Further information regarding the transducer and digital acquisition card (DAQ) will be covered in subsequent sections.

4.2 Transducer Specifications

In this project, a ring-shaped transducer allows for the construction of co-axial fiber optic/transducer arrangements. Biqin *et al.* (2017) [16] have simulated different detector geometries to evaluate their amplitude sensitivity distribution due to an ultrasonic monopole source. In Fig. 4.3, the frequency and spatial responses are displayed for four different detector geometries. Biqin *et al.* (2017) have shown that the ring shape detectors provide significant sensitivity at higher frequencies, making them suitable for broadband detection (Fig. 4.3). The specific transducer used in this project is a piezoelectric transducer from $StemInc.^{TM}$ with a center frequency of 3 MHz. The piezoelectric transducer is ring-shaped, 0.7 mm thick, 1.5 cm across the outer diameter of the ring and 0.85 cm across the inner diameter of the ring.

Once a PA signal is detected by the transducer, the analog voltage signal transmitted has frequency and amplitude parameters different than that of the natural phenomenon. In photoacoustics, the frequency response of a transducer is a measure of how quickly the detector can respond to changes in pressure. In most cases, the frequency response of a piezoelectric sensor loses accuracy above and below the resonant frequency of the piezoelectric element. For example, the 3 MHz piezo ring transducer from $Steminc.^{TM}$ [70] offers a resonant frequency of 2.95 MHz $\pm$ 3%. Therefore, in this project, the transducer used will detect PA signals most accurately when the signal frequencies are $\approx$ 3 MHz.

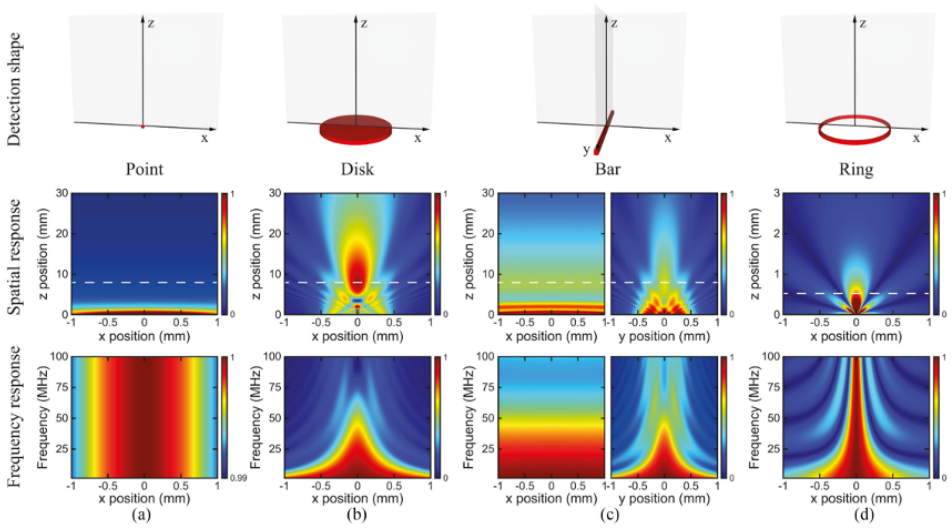

Figure 4.3: Simulation results from Biqin et al. (2017) [16] showing spatial and frequency responses of ultrasonic transducers. The top row of images shows the geometry of the transducers simulated. The middle row of images shows the spatial distributions of ultrasonic amplitude detection sensitivities to a monopole ultrasound source. The bottom row of images shows the spatial distributions of ultrasonic amplitude detection sensitivities at each position z, marked by a dotted line in the middle row.

4.3 DAQ Specifications

During PA signal recording, an oscilloscope data acquisition card (DAQ) converts analog voltage signals from the system transducer to a digital signal. Two DAQs were used in this project: initially a PCI-5122 from National Instruments containing a 14-bit ADC, and later a PCI-5102 from National Instruments containing an 8-bit ADC.

To begin signal recording, the DAQ used requires a trigger coinciding with the production of PA pressure waves. In the preliminary PA apparatus, the DAQ was triggered by a photodetector placed between harmonic generators in the laser. If the

probe is not moving and the PCI-5122 receives a voltage signal from the photodetector, the DAQ would begin to record any PA data from the transducer/pre-amplifier. In this arrangement, the trigger coincided with light pulses emitted by the laser pump. In the second PA apparatus, the DAQ was connected directly to the Q-switch of the laser itself. As previously mentioned in section 4.1, a Q-switch would signal the laser pump to emit a 5 ns pulse of light. Therefore, once the PCI-5102 receives the voltage signal from the VIBRANT Q-switch, the DAQ would begin to record any PA data from the transducer/pre-amplifier. Using the Q-switch, the trigger signal more directly coincided with the emission of light pulses by the laser pump.

Once the DAQ begins to record, the vertical and temporal resolution of the PA signals is determined by the bit size and sample rate of the ADC respectively. The PCI-5122 samples at a rate of 100 million samples per second while the PCI-5102 samples at a rate of 20 million samples per second. In this project, the PCI-5122 used a vertical range of 5 V, producing a resolution of 610 μV per vertical step. Otherwise, the PCI-5102 produced a resolution of 39 mV per vertical step. With respect to the digital PA waveform output by the DAQ, each data point in the signal recorded by the PCI-5122 represents 0.01 μs of time while each data point in the signal recorded by the PCI-5102 represents 0.05 μs of time.

4.4 Secondary Setup

Following several successful image acquisitions, a significant decrease in optical power output was noticed, and as a result, modifications were made to the setup. This new setup (Fig. 4.4) used the same 10 Hz $BRILLIANT^{TM}$ laser pump, but the OPO was changed in order to obtain more power at NIR wavelengths. Following the pump laser, a $\lambda/2$ waveplate is used to rotate beam polarization, prior to input into the OPOTEK $MagicPRISM^{TM}$ NIR OPO. The $MagicPRISM^{TM}$ is capable of outputting 680-970 nm light and is tuned via a PC and USB connection. Other optical instruments included in the second set-up include band-pass optical filtering lenses (650 nm $> \lambda >$ 900 nm), neutral density filters (0.3 OD, 1.0 OD), a beam collimator, and fiber optic launch. Short and long-pass optical filter lenses are included to reduce the influence of 1064 nm and 532 nm light originating from the pump laser. Neutral density filters were included because the pulse energy output by the OPO was higher than the limits set by the American National Standards Institute (ANSI) for laser light exposure. Also, the high pulse energy output by the OPO was also observed to cause damage to subsequent optics. Finally, a beam collimator was used to focus the laser beam into a fiber optic bundle.

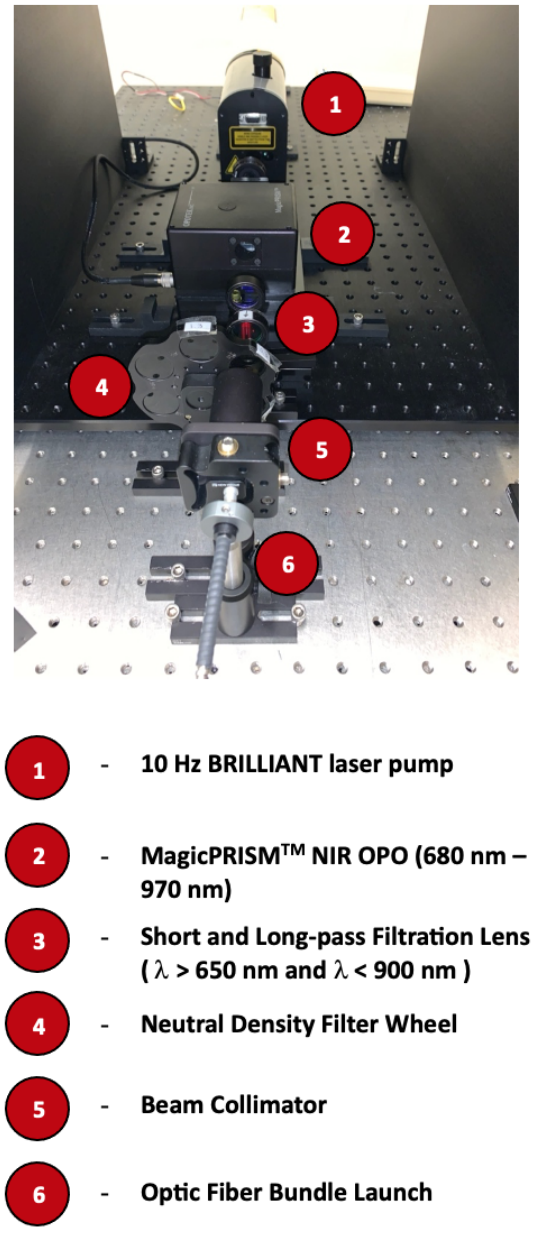

Figure 4.4: Secondary PA system arrangement. Not imaged: Handheld Probe, Phantom Bath, CNC Stages, Ultrasonic Pre-amplifier.

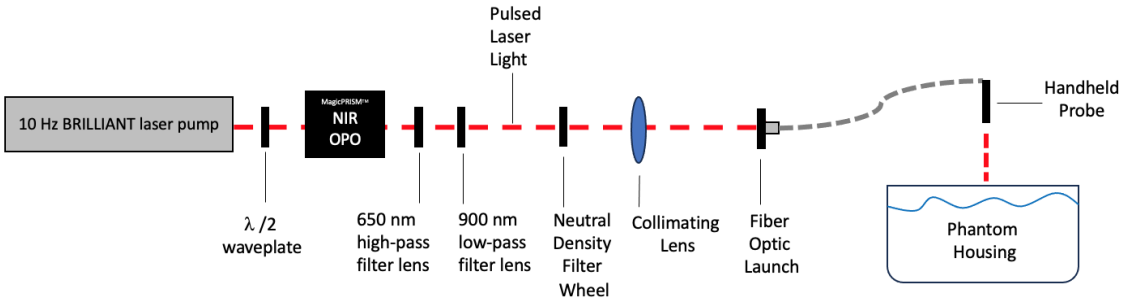

Figure 4.5: Secondary PA aystem arrangement schematic.

4.5 Laser Safety

According to ANSI guidelines, the maximum permissible exposure (MPE) to human skin by a laser is limited according to the wavelength used. It is crucial for any prospect of implementing this system in humans, that the PA system is safe. For each wavelength used, the pulse energy was recorded at various points in each laser apparatus.

For wavelengths (λ) between 400-700 nm, the MPE to a laser for less than 1 μs is 20 mJ/cm^2. For wavelengths between 700-1050 nm, the MPE to a laser for the same time is as follows:

$$\text{MPE} = 20 \times 10^{2(\frac{\lambda - 700}{1000})} \tag{4.5.1}$$

The wavelengths relevant to the clinical prospects of this project include scans with 640 nm, 750 nm, 850 nm, and 897 nm. Assuming that the beam radius of the VIBRANT laser is 3 mm [73], the maximum pulse energy permissible was calculated to be 5.6548 mJ/pulse, 7.119 mJ/pulse, 11.283 mJ/pulse, and 14.0093 mJ/ pulse respectively.

4.6 Probe Tracking

In the physical PA system, an (x,y) Computer Numerical Control (CNC) stage is used with a program called *moveStage*, to move the PA probe in a raster pattern above a tissue phantom. Once the computer acquires data at a certain (x,y) position, *moveStage* translates the probe by a set distance before the data acquisition system (DAQ) is triggered to record the next set of signals. In this project, the stage is moved in increments of 0.5 - 2 mm in the x and y dimensions resulting in a raster scan. In *moveStage*, the stepper motors move the probe across an area in space based on the dimensions and step size specified by the user. Limitations to an x,y CNC system for the purpose of detecting ICH include the inability to move the probe around a tissue model along a third dimension. Considering a 2D raster scan along a human head, if movements along the z-axis are not taken into account, resultant images of a curved head will be "flattened" into a 2D plane. In order to track the probe along a curved surface for accurate 3D imaging, a feedback system must record discrete translational distances before subsequent signal acquisitions.

In future experiments, a more sophisticated system for 3D space will be used to track the probe. Using Arduino and MATLAB software, initial investigations of a probe tracking system were conducted using an Adafruit inertial measurement unit (IMU), a Teensy microcontroller, and an Agilent optical mouse sensor. The microcontroller accesses the IMU and mouse sensor to read roll, pitch, and yaw values as well as x and y translational readings respectively. Roll, pitch, and yaw are gyroscopic measurements of rotation about three different Cartesian axes. If a vector were to be oriented along the z-axis, roll refers to rotation about the z-axis, pitch refers to rotation about the x-axis, and yaw refers to rotation about the y-axis. Using these

components, the PA system could utilize a handheld probe with a feedback mechanism responsible for tracking the probe's rotation and translation in 3D space. By acquiring PA signals at regular intervals, 2D translational and 3D rotational movements could be recorded during each acquisition.

4.7 *rasterizePA*

rasterizePA is the program used to automate the stage-translated raster scan and trigger PA data acquisition. The output of *rasterizePA* consists of a 4-dimensional dataset that contains multiple PA signals at each (x,y) location, stored as a 4D (x,y,t,N) matrix. First, *rasterizePA* will initialize the DAQ, then ask the user for a few inputs. The user is asked to define the number of signals to be collected at each location, the dimensions of the x-y grid to be scanned, as well as the step size of the probe in each direction. Once the parameters for the recording and raster pattern are defined, the program starts the scan and displays the image as each location is pulsed and detected. An image is displayed in real-time consisting of coloured pixels with brightness relative to every other pixel in the image. The value within each pixel is calculated by summing the absolute value of each data point in a PA signal within a range of depth defined by the user. In this project, the PCI-5122 records for 40 μs at each (x,y) location, for a total number of 4000 data points per pulse. When the PCI-5102 is used, the DAQ records for 25 μs at each (x,y) location, for a total number of 500 datapoints per pulse. During raster scans, the DAQ would record 10 sample PA signals at each location, which are averaged to reduce background noise. For the images provided in the following sections, x and y resolutions range from 0.5 mm to 2 mm.

4.8 *ratioimage*

Following a 2D raster scan over the field of view (FOV) at 750 nm, a subsequent scan over the same FOV was performed using 850 nm light. *ratioimage* is the program used to produce Red:NIR ratio images of phantoms imaged during the project. *ratioimage* was used to output a 2D image with pixels representing the average Red:NIR ratio of PA signals produced by optical absorbers in response to each wavelength of light used. Before a Red:NIR ratio image is produced, the pulse energy is measured at each wavelength. It is necessary that the same amount of incident light energy is imparted on the phantom between wavelengths to derive accurate Red:NIR ratios that reflect differences in absorption. Therefore, when the phantom is irradiated by red or NIR light at different pulse energies, the PA signals produced by the phantom are scaled by the ratio of the pulse energies used. This way, any difference in PA signal amplitude can be attributed to differences in the optical absorption properties of the phantom rather than by variations in laser output power. Afterward, the absolute value of the PA signals at each pixel from the 750 nm image are divided by the signals at the same locations in the 850 nm image. Ratios with denominators $\simeq 0$, or denominators $= 0$, had the quotients set to 1. Also, ratios with numerators equal to zero had the quotients set to 1. Finally, the average Red:NIR ratios were displayed in pixels across varying slice thicknesses. *ratioimage* was also used to produce single-wavelength maximum intensity projections (MIP). When displaying single-wavelength MIPs, pulse energy scaling is done to account for the incident energy mismatch, and the absolute value of each PA signal is still taken. However, slices are not created to produce 2D MIPs. For the 2D MIPs produced in this project, each pixel displays the maximum PA signal value across all time points.

4.9 Phantom Specifications

In this project, several imaging phantoms were tested in increased complexity.

The first phantom imaged consisted of a $Formlabs^{TM}$ black resin ellipsoid measuring 5 cm in length, 1.2 cm in width, and 3 cm in height (Fig. 4.6). The ellipsoid also had a 1.2 cm diameter hole across its width. The ellipsoid was submerged in water and suspended by monofilament fishing line $\sim$ 1.5 cm below the transducer. This phantom was imaged many times using wavelengths of light ranging from 530 nm to 1001 nm. Black plastic resin was used because it was a cost-effective and geometrically-customizable material that proved to produce PA signals from NIR light efficiently.

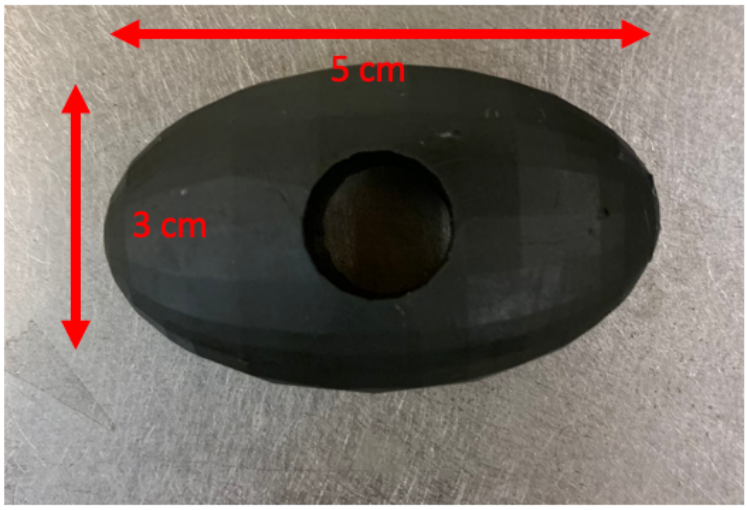

Figure 4.6: Simple Ellipsoid Absorber

The second imaging phantom tested was called the scaffold phantom. The scaffold phantom consists of a 3D printed geometry of black plastic resin suspended in a water bath. The scaffold geometry can be seen in Fig. 4.7 and consists of cylindrical trusses

connecting a top and bottom rod in a triangular pattern. The plastic is 1 mm wide at all points of the geometry. The scaffold phantom was developed and imaged to further test the limits of the PA imaging system with respect to spatial resolution. The scaffold phantom was imaged using 750 nm light and 850 nm light.

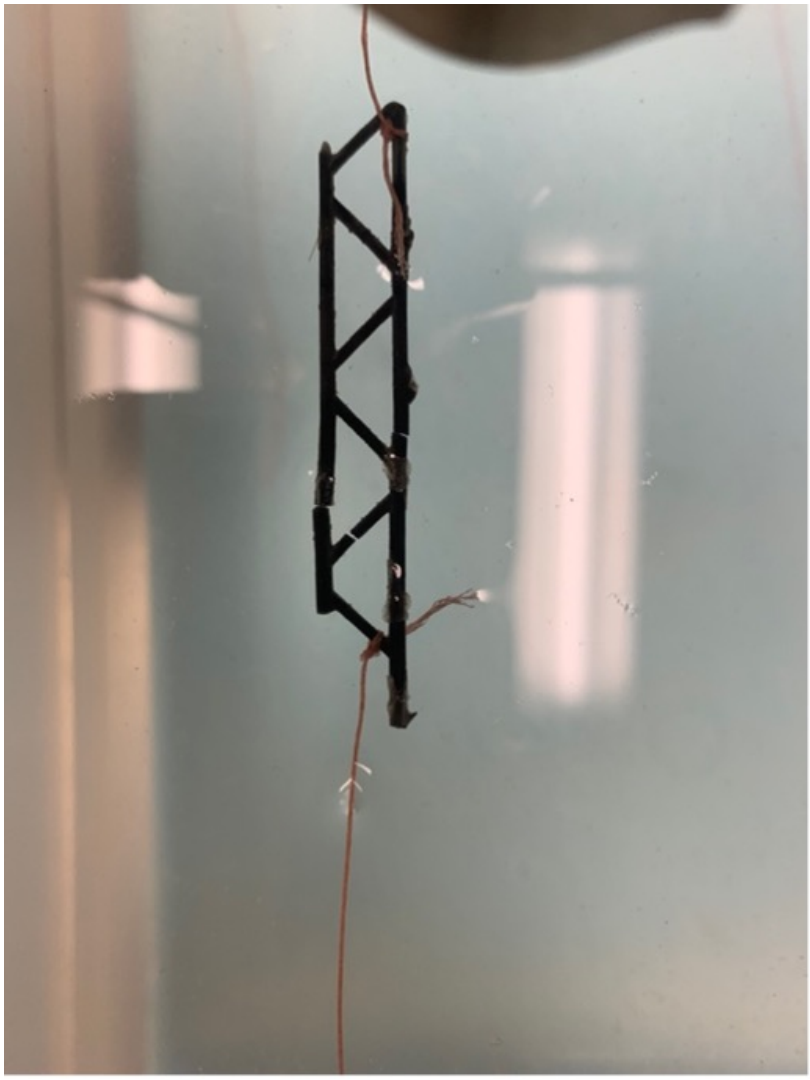

Figure 4.7: Scaffold Absorber

A subsequent imaging phantom tested was called the soft tissue phantom. The soft tissue phantom was created to suspend the black resin optical absorbers at specific depths in knox gelatin (Fig. 4.8). Colourless gelatin was expected to mimic the optical properties of grey and white matter in the brain. Many studies reference the mixture of intralipid solution in gelatin for photoacoustic brain phantoms [11], but soft tissue phantom scans were aimed at investigating the effect of gelatin alone on PA signal generation before increasing the optical intricacy of the phantoms. The soft tissue phantom was imaged using 550 nm light, 640 nm light, and 869 nm light.

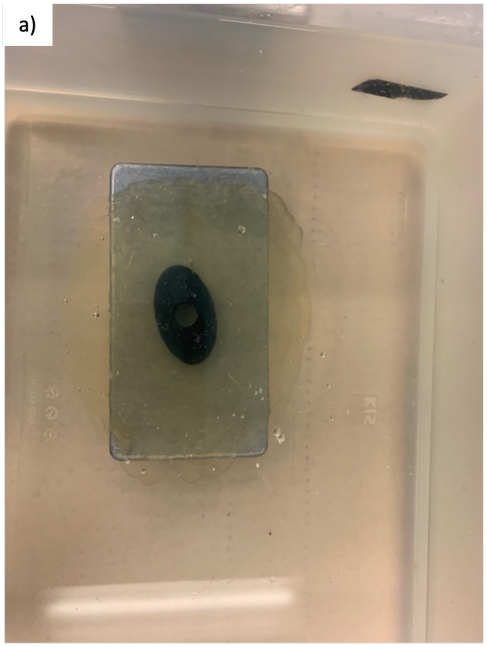

(a) X-Y Plane

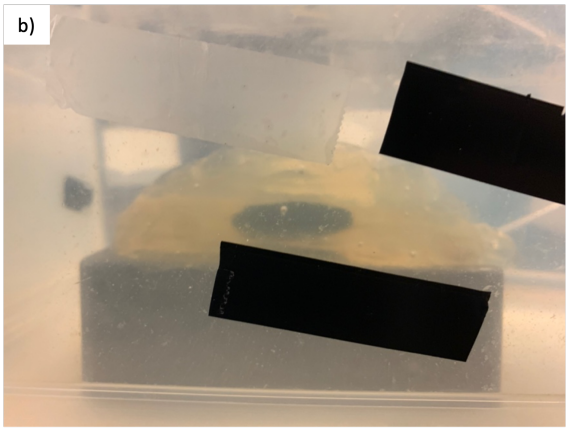

(b) X-Z Plane

Figure 4.8: Soft tissue phantom consisting of translucent $Knox^{TM}$ gelatin surrounding the black resin ellipsoid absorber

To develop phantoms more representative of a hematoma tissue model, the optical absorption and scattering of the media surrounding the resin absorbers was increased. To achieve this, a lipid phantom was created consisting of 50% v/v knox gelatin and 50% v/v canola oil [34]. Also using the gelatin mold, a superior layer 1 cm deep of ThermoFisher Scientific India Ink emulsified in gelatin was developed [71] (Fig. 4.9). According to a project by Di Ninni *et al.* [14], the absorption absorption coefficient of India Ink in gelatin with respect to 633 nm light could be estimated as a function of the % weight concentration as follows:

$$\mu_a = 372.9 \times (\%\ \text{Ink Concentration}) + 0.0019 \tag{4.9.1}$$

Therefore, for an absorption coefficient of 0.0053 cm^{-1} at 633 nm, a % weight concentration of $\sim 0.014\%$ is required to mimic the skull.

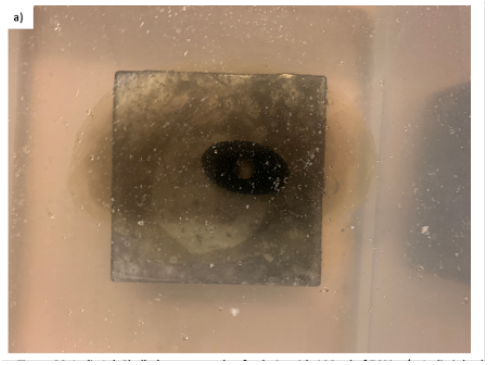

(a) X-Y Plane

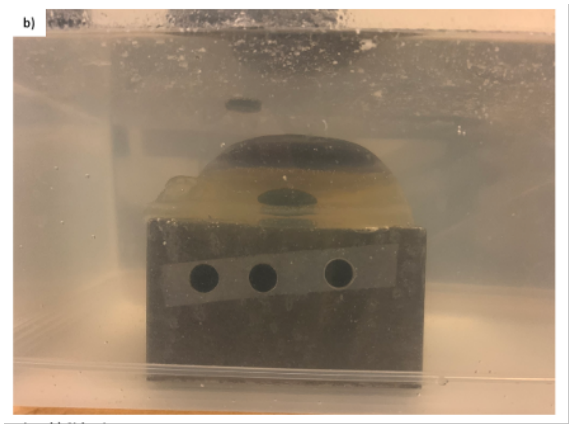

(b) X-Z Plane

Figure 4.9: India Ink phantom consisting of translucent $Knox^{TM}$ gelatin surrounding the black resin ellipsoid absorber. 1 cm of gelatin above the ellipsoid was emulsified with India Ink

Finally, an imaging phantom using skull-mimicking material was created and imaged using a procedure from a study by Rao and colleagues [63]. Using reflectometry, Rao offers a low-cost, optically accurate imaging phantom for skull using paraffin wax and black and white pigment dyes. Rao computed an expected reflectance profile for a skull layer based on values of μ_a and μs from available literature. Then, by measuring the reflected intensity of 670 nm light, the profile of phantoms containing various concentrations of pigment dye could be matched to the known profile. In this project, the skull phantom used 100 ml of paraffin wax, 10 mg of black pigment dye, and 160 mg of white pigment dye. The skull model dimensions are 12 cm in length, 12 cm in width, and 7 mm in depth. During imaging acquisitions, the skull layer was suspended using monofilament fishing line above half of the resin ellipsoid (Fig. 4.10).

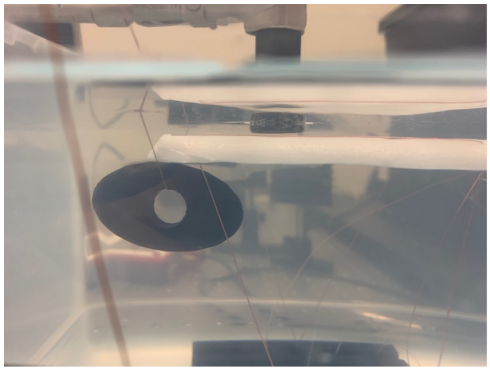

(a) X-Y Plane

(b) X-Z Plane

Figure 4.10: Half-Covered Ellipsoid phantom consisting of skull-tissue-mimicking material positioned above the black resin ellipsoid absorber.

Chapter 5

Results & Discussion

5.1 Simulations

5.1.1 Wavelength Selection Process

As discussed in Section 1, changing the wavelength of incident pulsed laser light in PA imaging simulations changes the contrast between deoxygenated blood and other tissue types. To obtain accurate information about blood SpO_2 from the Red:NIR ratio, the incident power to the site of interest should be the same for each wavelength. This implies that, when imaging tissue models, the chosen Red and NIR wavelengths must exhibit as similar absorption coefficients for dermis and skull as possible, while remaining on opposite sides of the hemoglobin isosbestic point. Initially, according to the absorption spectra in Fig. 1.2, contrast was maximized by using wavelengths of 680 nm and 990 nm. These wavelengths exhibited one of the highest differences in absorption coefficients between hemoglobin species while staying within the biological optical window. At wavelengths shorter than 650 nm, the absorption coefficients of

other tissues such as bone increase dramatically. At wavelengths longer than 1000 nm, absorption of incident light by water dominates any absorption by blood. It was found that the absorption coefficients for the dermis were closest in magnitude between a "red wavelength" of 750 nm and an "IR wavelength" of 850 nm. The absorption coefficient for dermis at 850 nm is 0.0380 cm^{-1}, 1.49 times greater than the coefficient at 750 nm, at 0.0256 cm^{-1}. For the skull, the absorption coefficients had a similar ratio at 850 nm with an absorption coefficient of 0.0176 cm^{-1}, 1.59 times higher than the absorption coefficient for 750 nm, when it is 0.0111 cm^{-1} (Fig. 5.1). It can also be seen that in comparison to the wavelengths used in the simple vessel models (680 nm and 990 nm), the absorption coefficients for the superficial layers are much closer in magnitude. To confirm that optical contrast can still be achieved at the wavelengths chosen, the Red:IR ratio (750 nm : 850 nm) of absorption coefficients in deoxygenated blood was determined to remain above 1 at $\sim$1.9.

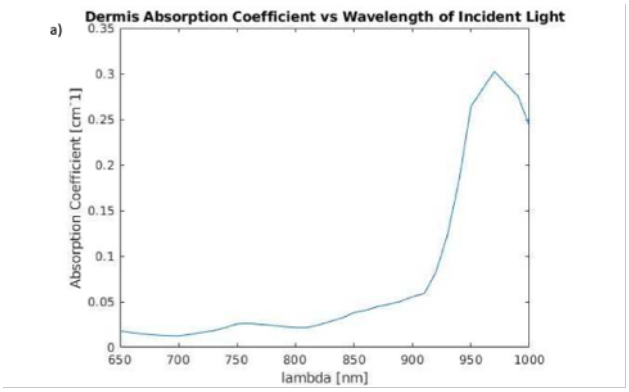

(a) Dermis absorption coefficients

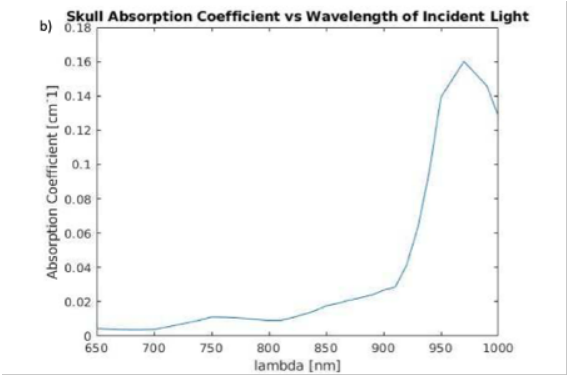

(b) Skull absorption coefficients

Figure 5.1: Absorption spectra of superficial tissue layers across wavelengths in the biological window (650nm -1000nm)

5.1.2 Signal Plots

Across simulations for all tissue models, the Red:NIR ratio remained positive for portions of PA signals corresponding to HHb. Fig. 5.2 includes plots of PA signals from the centre of every tissue model to compare results between wavelengths. In all tissue models, the blood tissue is located 7 mm beneath the transducer. As expected, the signals plotted in Fig. 5.2 show the largest section of the PA pressure wave arriving 4.6 μs after the laser pulse.

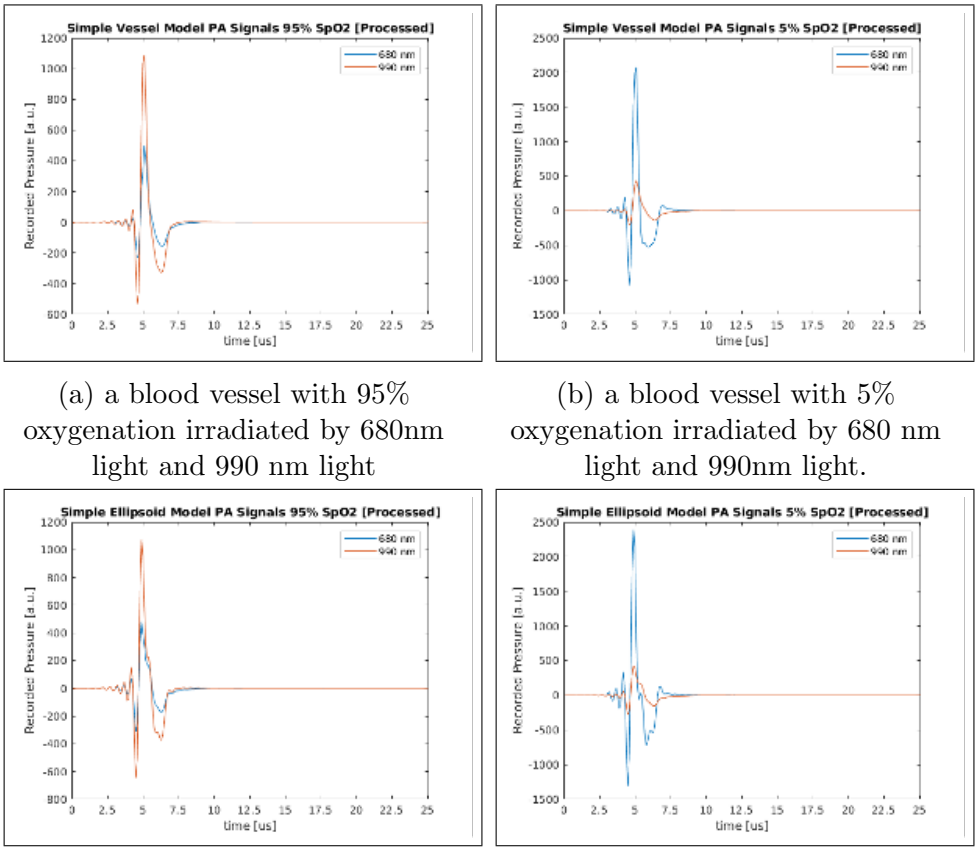

(a) a blood vessel with 95% oxygenation irradiated by 680nm light and 990 nm light

(b) a blood vessel with 5% oxygenation irradiated by 680 nm light and 990nm light.

(c) an ellipsoid with 95% oxygenation irradiated by 680nm light and 990 nm light

(d) an ellipsoid with 5% oxygenation irradiated by 680nm light and 990 nm light

Figure 5.2: Recorded PA Signals from simple tissue models

The shape of the PA signal supports the theoretical linear correlation between chromophore absorption and PA signal amplitude. With respect to the chromophores included in simulated tissue models, hemoglobin dominates absorption and produce the largest pressure wave when the chosen wavelengths were used for the PA effect. Specifically, the largest peaks recorded during imaging simulations originated from deoxygenated tissue models.

5.1.3 Formula of Best Fit

Using data from PA imaging raster scans, the maximum observable Red:IR ratio decreased according to the following formula:

$$\text{Red:NIR ratio} = 5.4689 \times 10^{-4} \cdot (SpO_2)^2 - 0.1103 \cdot (SpO_2) + 6.0547 \qquad (5.1.1)$$

The coefficients for the curve of best fit were calculated using a least-squares method for a second-degree polynomial. The entire curve and its proximity to the simulation results can be seen below in Fig. 5.3.

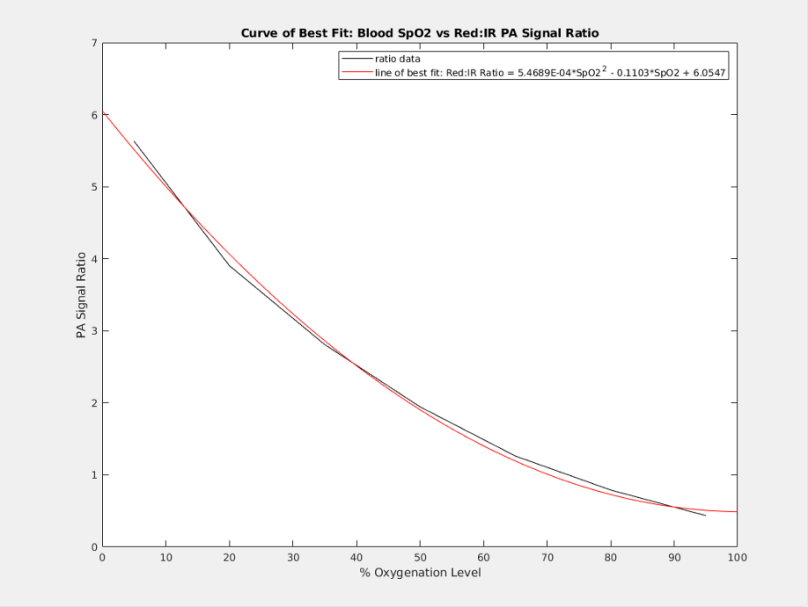

Figure 5.3: The average PA signal ratio from a simple vessel model vs. 15% oxygenation intervals. Regression Formula:
$Red:NIR \;\; ratio = 5.4689 \times 10^{-4} \cdot (SpO_2)^2 - 0.1103 \cdot (SpO_2) + 6.0547.$

Using the curve of best fit formula, the maximum expected signal amplitude between the two wavelengths will be identical at about 70.4016 % SpO_2.

As expected, the curve of best fit displays an inverse correlation between blood SpO_2 and the calculated Red:NIR ratio. During the wavelength selection process, it was important to use two wavelengths of light at which the absorption in the tissue surrounding the hematoma would be identical. As a result, tissue models with oxygenation at which the ratio is expected to be 1 will show little to no contrast between the blood and surrounding tissue in reconstructed images. Still, due to the nature of the hemoglobin absorption spectra, the red:NIR ratio of PA signals between hemoglobin species will be greater than 1 until SpO_2 reaches $\sim$70%.

Therefore, in PA imaging applications using a formula of best fit to estimate SpO_2 from the Red:NIR ratio, blood tissue will appear "oxygenated" in Red:NIR ratio image reconstructions until $\sim$70% SpO_2. According to [49], SpO_2 values $<$90% are considered low. Therefore, the formula of best fit will be useful for estimating SpO_2 from Red:NIR ratio images when ischemia is unclear. Still, it is expected that the accuracy of the formula is limited by the geometry of blood producing the ratios used as input to the least-square regression algorithm. As discussed in Section 3, it is expected that physical systems will scan tissue models with different geometry, changing patterns of optical scattering and absorption. Also, it is expected that physical PA imaging systems will experience errors in system hardware, altering PA signal strength over time.

5.1.4 Image Reconstruction

Fig. 5.4, 5.5, 5.6, and 5.7 display 2D images at certain depths reconstructed using the signal arrays collected using *mcxyz.c* and *k-wave* software. The images represent a slice of the tissue model in the xy-plane, averaging the absolute value of PA signal amplitude across ∼1.5 mm of depth. The images span 38 mm in the x direction and 38 mm in the y direction, with each pixel representing a 2 mm step. The normalized Red:NIR ratio is higher in deoxygenated tissue models than in oxygenated tissue models, as expected. The $\log_{10}$ of the Red:NIR ratio is displayed in each pixel in order to control image contrast. Displaying the $\log_{10}$ of the Red:NIR ratio values introduces a linear scale to pixel ratio values in the FOV. Also, the upper and lower limits of pixel values displayed are identical between tissue models that differ only in SpO_2 for easier visual comparison.

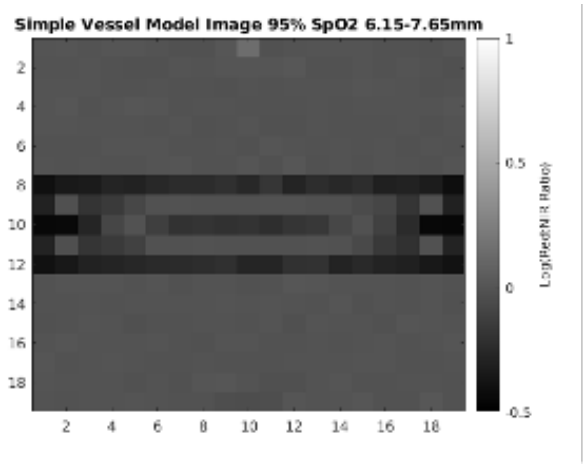

(a) Ratio image of simple vessel model with 95% SpO_2 at depth 6.15 - 7.65 mm.

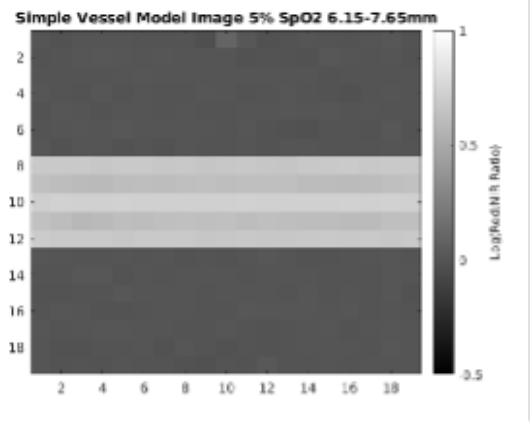

(b) Ratio image of simple vessel model with 5% SpO_2 at depth 6.15 - 7.65 mm.

Figure 5.4: Red:NIR ratio image reconstructions of simple vessel models using scans with 680 nm light and 990 nm light.

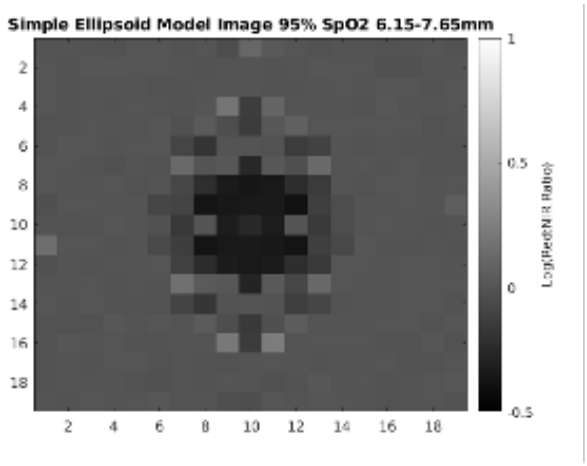

(a) Ratio image of simple ellipsoid model with 95% SpO_2 at depth 6.15 - 7.65 mm.

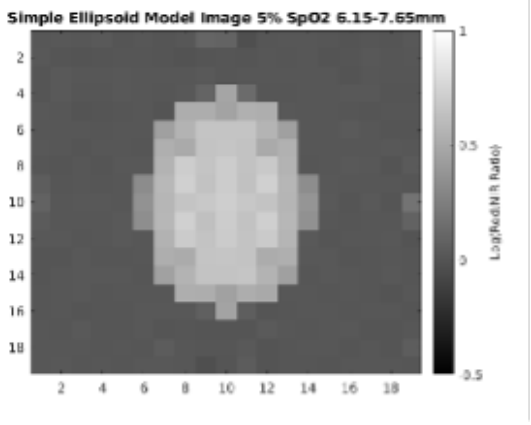

(b) Ratio image of simple ellipsoid model with 5% SpO_2 at depth 6.15 - 7.65 mm.

Figure 5.5: Red:NIR ratio image reconstructions of simple ellipsoid models using scans with 680 nm light and 990 nm light.

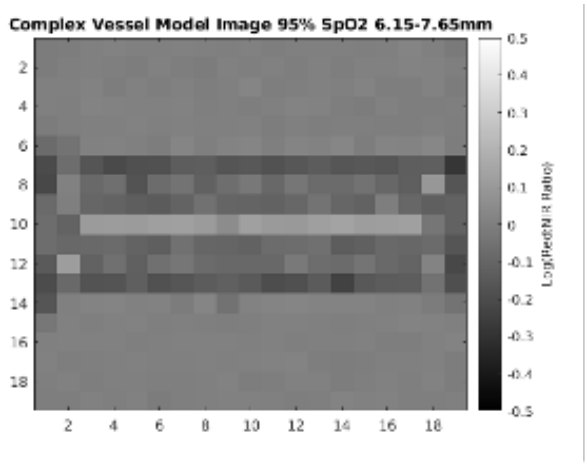

(a) Ratio image of complex vessel model with 95% SpO_2 at depth 6.15 - 7.65 mm.

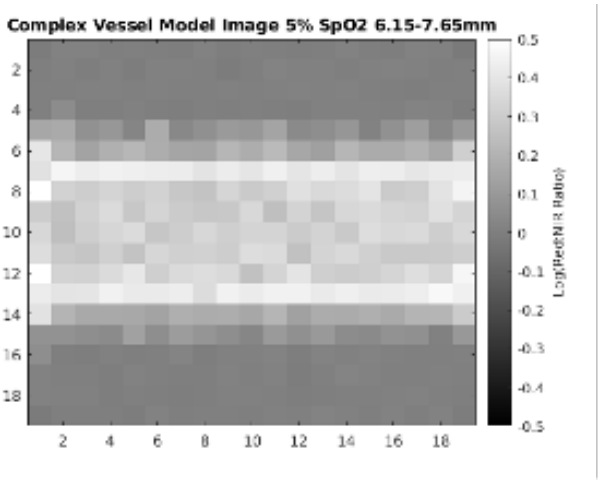

(b) Ratio image of complex vessel model with 5% SpO_2 at depth 6.15 - 7.65 mm.

Figure 5.6: Red:NIR ratio image reconstructions of complex vessel models using scans with 750 nm light and 850 nm light.

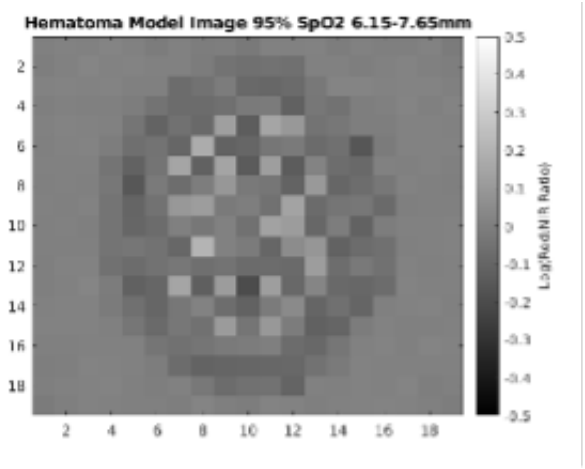

(a) Ratio image of hematoma model with 95% SpO_2 at depth 6.15 - 7.65 mm.

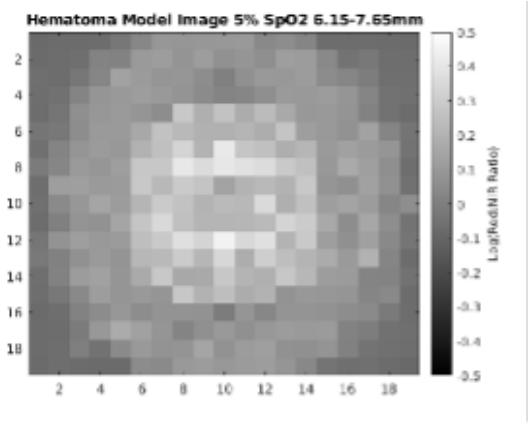

(b) Ratio image of hematoma model with 5% SpO_2 at depth 6.15 - 7.65 mm.

Figure 5.7: Red:NIR ratio image reconstructions of hematoma models using scans with 750 nm light and 850 nm light.

In this project, it was noted that in reconstructions of simple and complex tissue models with 95% SpO_2, the average ratio was lower than or equal to 1, compared to identical tissue models with 5% SpO_2 in which the average Red:NIR ratio was much greater than 1. These results confirm that a PA imaging technique can produce contrast between varying SpO_2 levels using the absorption spectra of hemoglobin, even across thin layers of bone.

Furthermore, in all reconstructions, the relative geometry of the tissue model was preserved. Specifically in complex tissue models, a cylindrical vessel and ellipsoid shape were evident, however, the radii are exaggerated. This can be explained by the shape of the transducer simulated in the k-wave program. In complex tissue models, (x,y) pixel locations at which there is no vessel beneath the light source (Fig. 5.8a) will still produce significant PA signals due to optical scatter from the superficial layers (Fig. 5.8b). However, because the transducer and the light source are not of equivalent size and shape, the pressure wave does not travel the assumed distance from the IPD to the light source. Instead, transducer elements closer to the IPD will detect the pressure wave at a time point earlier than would be expected if the sensor was at the same position as the beam. Therefore, when *butterimage* displays a pixel that is next to the vessel, the geometry of the transducer allows for those pressure waves to arrive at similar times as those where the light source was directly above the vessel (Fig. 5.8c).

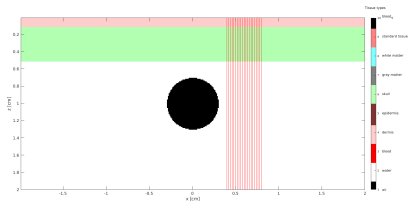

(a) An XZ-plane cross-section of a complex vessel tissue model displaying an incident beam originating at an x-axis position right of the vessel.

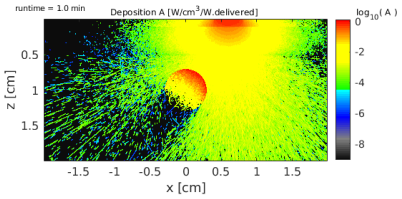

(b) An XZ-plane cross-section of a complex vessel tissue model absorption map produced by 750 nm light.

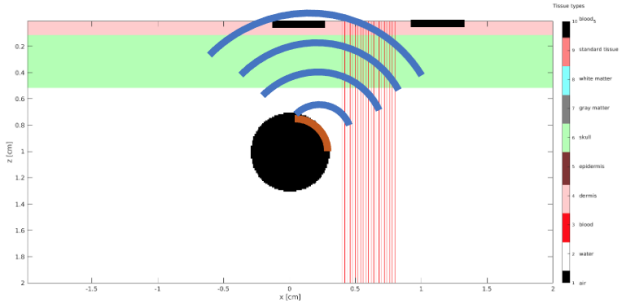

(c) A schematic illustrating the behaviour of a resultant PA wave produced by the optical absorption seen in Fig. 5.8b. The orange arc shape represents the portion of the tissue model that absorbed the most optical energy (a simplified IPD). The blue arc shapes represents PA wave propagation towards the transducer. The black lines at the top of the image represent the position of ring-shaped binary transducer.

Figure 5.8: Schematics illustrating the cause of exaggerated radii of blood tissue geometries in 2D reconstructed PA images.

5.2 Experimental Validation

5.2.1 Single-wavelength PA Images

Single-wavelength PA images were acquired for two reasons: to test the spatial resolution of the system and gather data on an expected Red:NIR ratio for the Formlabs black resin material. When validating the results of imaging simulations with each PA system setup, the most informative acquisitions came from the simple ellipsoid phantom, the simple scaffold phantom, the soft tissue phantom, and the half-covered ellipsoid phantom. Figures 5.9 - 5.16 use a second y-axis for PA signal plots to convey the approximate depth at which the absorber was located that produced the pressure wave. The approximate depth was calculated using the speed of sound in water (1.5 mm/s). Fig. 5.9 and 5.10 show 2D images at 16.5 mm - 22.5 mm depth reconstructed from the simple ellipse phantom with an associated PA signal for both 750 and 850 nm light. The images in Fig. 5.9a and 5.10a span 5 cm in the x direction, and 7 cm in the y direction, with each pixel representing a 2 mm step. The PA signals in Fig. 5.9b and 5.10b represent the raw PA signal data for pixel (x,y) = (14,18) for both scans.

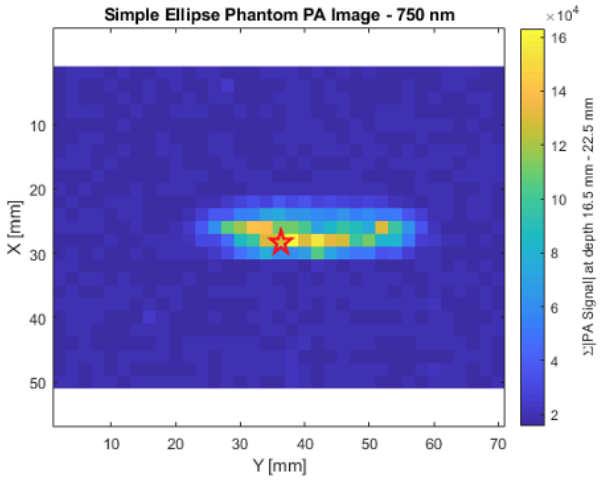

(a) PA image of the simple ellipsoid phantom using 750 nm light at depth 16.5 - 22.5 mm. The red star indicates the pixel representing 5.9b.

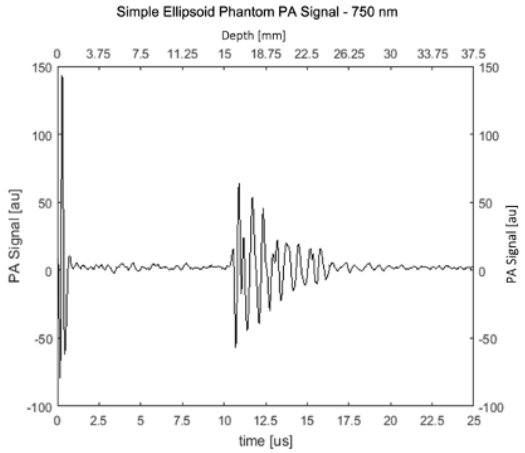

(b) Sample PA signal from 5.9a.

Figure 5.9: Resultant image and signal from PA raster scans using 750 nm light. Images produced using the second PA system set-up and the PCI-5102.

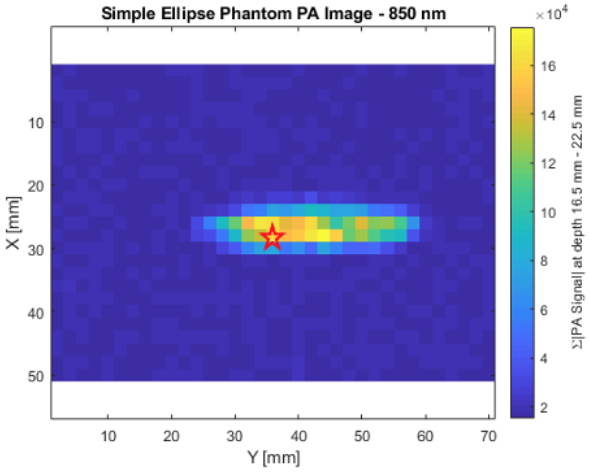

(a) PA image of the simple ellipsoid phantom using 850 nm light at depth 16.5 - 22.5 mm. The red star indicates the pixel representing 5.10b.

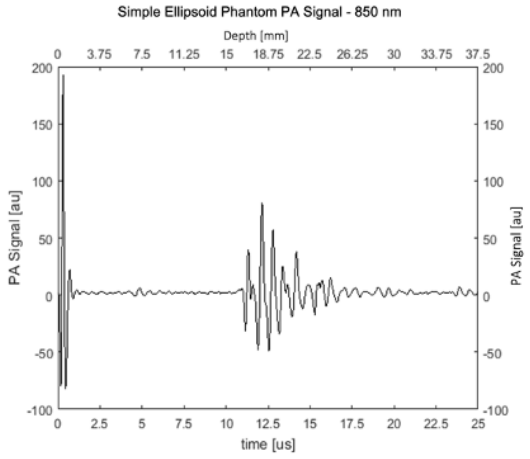

(b) Sample PA signal from 5.10a.

Figure 5.10: Resultant image and signal from PA raster scans using 850 nm light. Images produced using the second PA system set-up and the PCI-5102.

Between both single-wavelength images produced of the simple ellipsoid phantom in Fig. 5.9 and 5.10, the 850 nm image displays larger amplitude PA signals. According to these images, this would indicate that the black plastic resin has a higher absorption coefficient at 850 nm than at 750 nm. Both images display an absorber geometry 5 pixels wide in the X direction, and 19 pixels long in the Y direction. Because the simple ellipsoid phantom scan was conducted using a step size of 2 mm, the images convey an absorber width of 10 mm and a length of 38 mm. The absorber is known to be 12 mm in width and 50 mm in length. One potential reason for an underestimation in absorber size is that the effective volume of the ellipsoid at its vertices (endpoints of the major axis) is much smaller. According to the stress and thermal confinement conditions for PA signal generation, the smaller the desired spatial resolution, the shorter the time the pulse energy must be. Therefore, because the 5 ns pulse is expected to provide very high spatial resolution, the amount of light energy delivered to ellipsoid vertices must be insufficient to produce a significant PA signal.

Fig. 5.11 and 5.12 show 2D images at 18 mm - 19.5 mm depth reconstructed from the simple scaffold phantom with an associated PA signal for both 750 and 850 nm light. Fig. 5.11a and 5.12a images span 5.85 cm in the x direction, and 2.25 cm in the y direction, with each pixel representing a 0.5 mm step. The PA signals in Fig. 5.11b and 5.12b represent the raw PA signal data for pixel (x,y) = (79,38) for both scans.

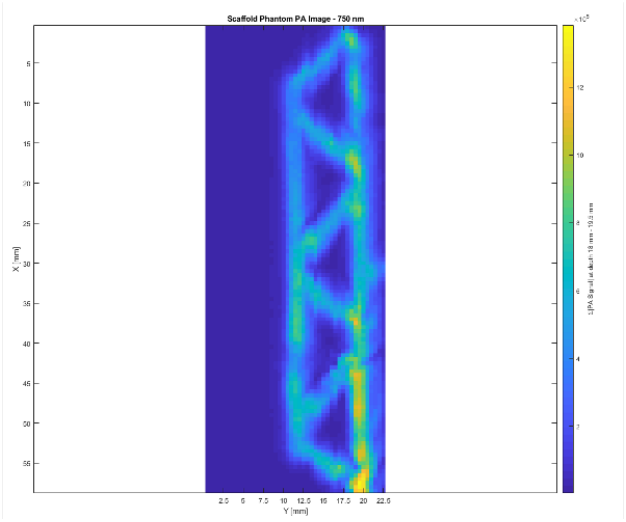

(a) PA image of the scaffold phantom using 750 nm light at depth 18 - 19.5 mm.

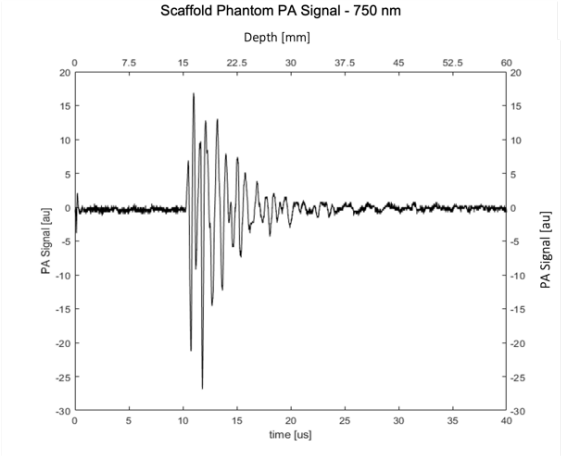

(b) Sample PA signal from 5.11a.

Figure 5.11: Resultant image and signal from PA raster scans using 750 nm light. Images produced using the second PA system set-up and the PCI-5122.

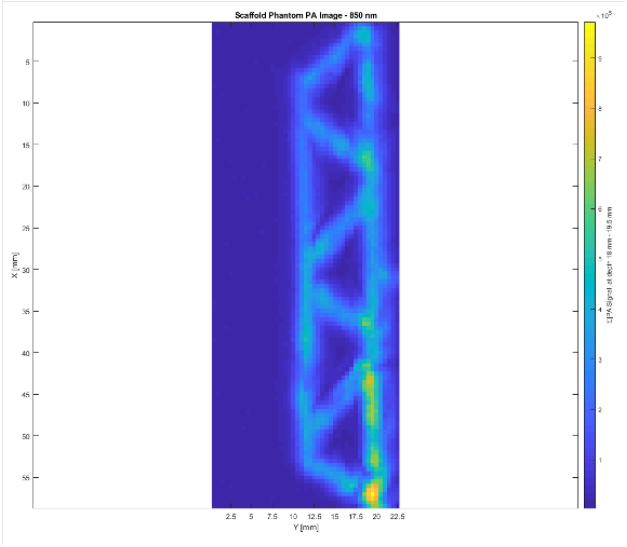

(a) PA image of the scaffold phantom using 850 nm light at depth 18 - 19.5 mm.

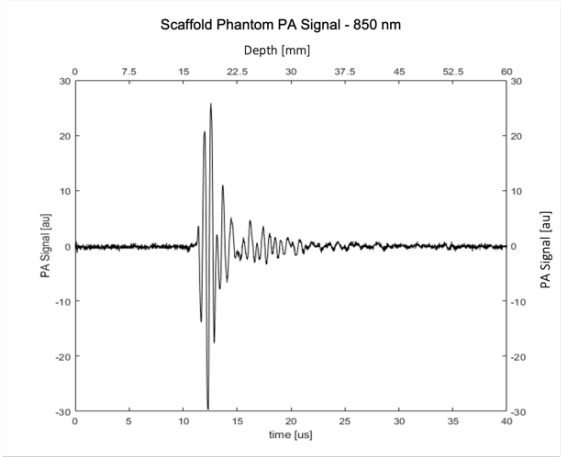

(b) Sample PA signal from 5.12a.

Figure 5.12: Resultant image and signal from PA raster scans using 850 nm light. Images produced using the second PA system set-up and the PCI-5122.

According to the single-wavelength images of the scaffold phantom shown in Fig. 5.11 and 5.12, the 750 nm image displays higher amplitude PA signals. This offers contradictory information about the absorption coefficient of the ellipsoid material when both wavelengths are used. When acquiring the scaffold images in Figure 5.11 and 5.12, a step size of 0.5 mm was used during the raster scan. The scaffold absorber is known to consist of rods 1 mm in width, yet the images display rods at least 2 mm in width. One explanation for this overestimation in size is the beam spread out of the probe. At (x,y) locations where the scaffold is not positioned along the same z-axis as the fiber optic, beam spread may still cause light energy deposition in the absorber, resulting in a PA signal. When depth images are reconstructed, the scaffold absorber appears larger than it is.

Fig. 5.13 and 5.14 show images at 39 mm - 42 mm depth reconstructed from the soft tissue phantom with an associated PA signal for both 640 and 869 nm light. Fig. 5.13a and 5.14a images span 7.6 cm in the x direction, and 4.8 cm in the y direction, with each pixel representing a 2 mm step. The PA signals in Fig. 5.13b and 5.14b represent the raw PA signal data for pixel (x,y) = (14,13) for both scans.

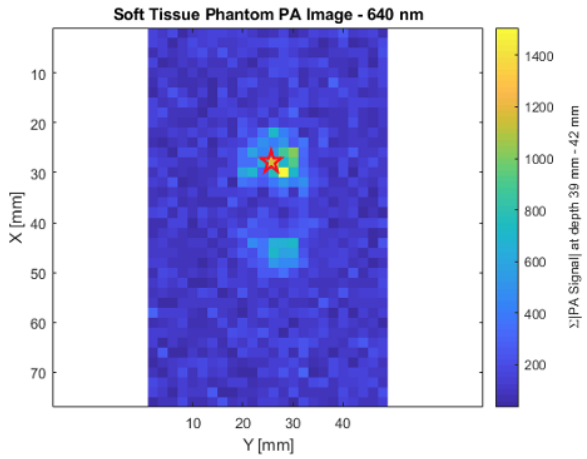

(a) PA image of the soft tissue phantom using 640 nm light at depth 39 - 42 mm. The red star indicates the pixel representing 5.13b.

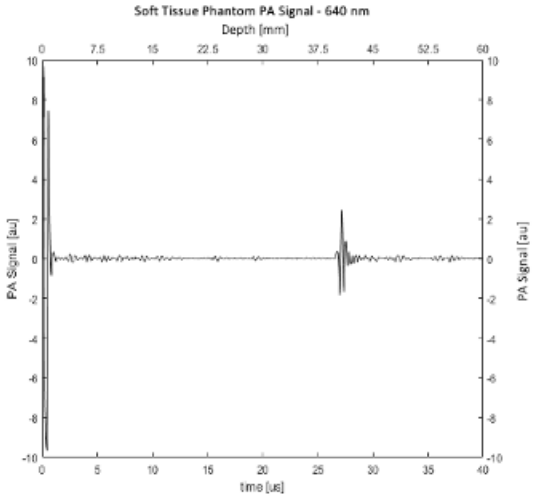

(b) Sample PA signal from 5.13a.

Figure 5.13: Resultant image and signal from PA raster scans using 640 nm light. Images produced using the first PA system set-up and the PCI-5122.

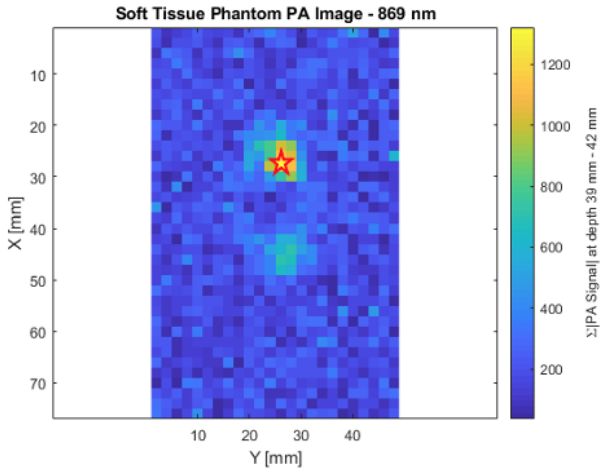

(a) PA image of the soft tissue phantom using 869 nm light at depth 39 - 42 mm. The red star indicates the pixel representing 5.14b.

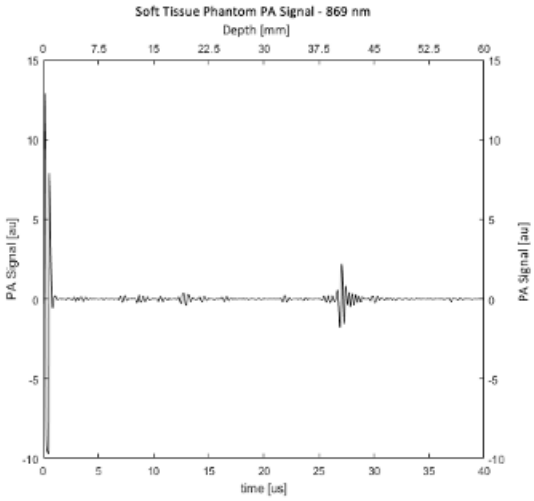

(b) Sample PA signal from 5.14a.

Figure 5.14: Resultant image and signal from PA raster scans using 869 nm light. Images produced using the first PA system set-up and the PCI-5122.

The depth images displayed in Fig. 5.13 and 5.14 allow us to assess the impact of a soft-tissue-mimicking material on PA signals. When scanning the soft tissue phantom, light propagated through water before reaching gelatin at depth ≥ 1 cm beneath the transducer, reaching the target absorber at $\sim$4 cm of depth. In Fig. 5.13b and 5.14b, there are no significant PA pressure waves correlated to the PA effect in the gelatin. At the depth shown in Fig. 5.13a and 5.14a, the SNR appears to be less than that of other acquisitions. A lower SNR could be due to several reasons, but two suggestions include a lower pulse energy output from the PA system as well as a greater scattering coefficient for gelatin compared to water. The initial PA system was used to acquire images for the soft tissue phantom, and pulse energy measurements were recorded to be $\sim$ 0.2 mJ/pulse. Although the absorber geometry could still be resolved, the low pulse energy measurements were the main incentive to change the OPO and develop the second PA system. With respect to differences in scattering coefficient, μ_s of $Knox^{TM}$ gelatin is unknown, however, the μ_s of soft tissue is 100 cm^{-1}, ten times that of water. Therefore, the more accurate the phantoms mimic hematoma *in vivo*, the more scattering will occur, and the lower the SNR will be.

Fig. 5.15 and 5.16 show images at depth 16.5 mm - 18 mm reconstructed from the half-covered ellipsoid phantom with associated PA signals for both 750 and 850 nm light. The skull-mimicking material covers half of the ellipsoid in the phantom and begins at y = 20 during both raster scans. Fig. 5.15a and 5.16a images span 5 cm in the x direction, and 7 cm in the y direction, with each pixel representing a 2 mm step. The PA signals in Fig. 5.15b and 5.16b representing uncovered ellipsoid are shown using the pixel (x,y) = (17,16) for both scans. The PA signals representing covered ellipsoid in Figure 5.15b and 5.16b are shown using the raw PA signal data for pixel (x,y) = (17,22) for both scans.

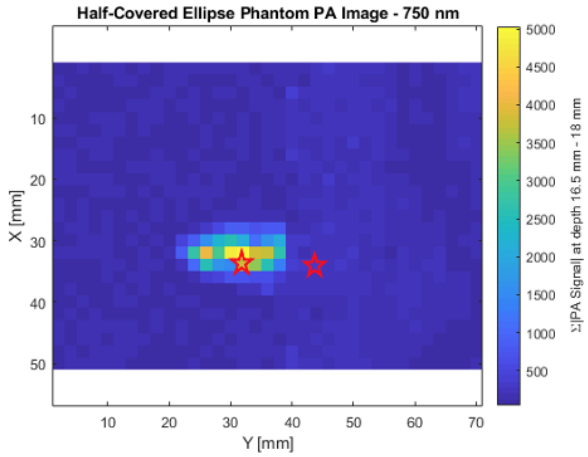

(a) PA image of the Half-Covered Ellipsoid phantom using 750 nm light at depth 16.5 - 18 mm. The red stars indicate the pixels representing 5.15b.

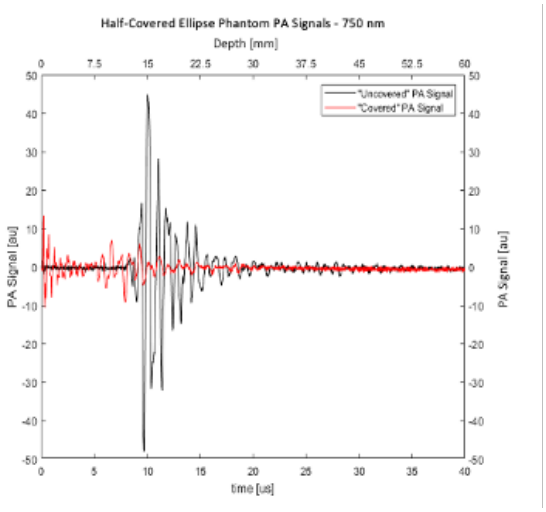

(b) Sample PA signals from 5.15a.

Figure 5.15: Resultant image and signals from PA raster scans using 750 nm light. Images produced using the second PA system set-up and the PCI-5122.

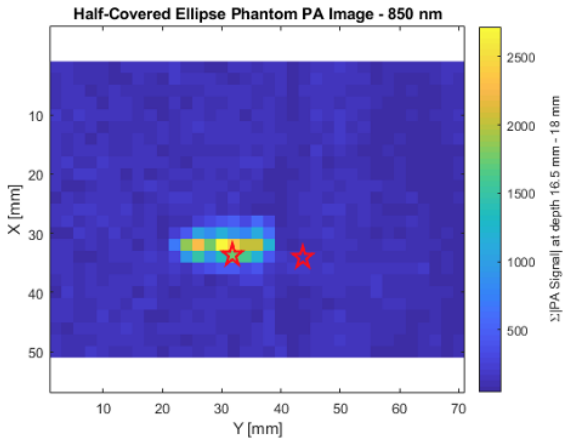

(a) PA image of the Half-Covered Ellipsoid phantom using 850 nm light at depth 16.5 - 18 mm. The red stars indicate the pixels representing 5.16b.

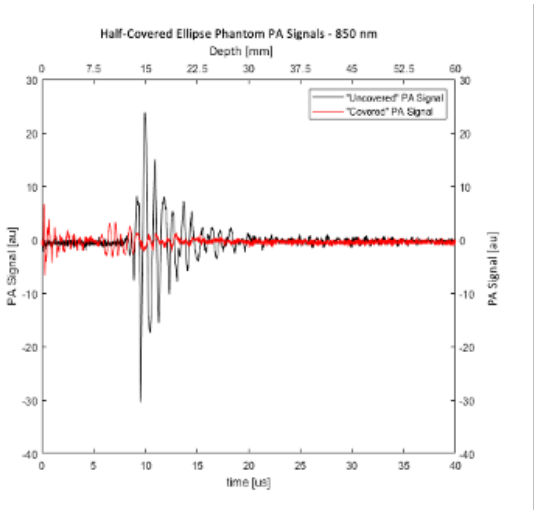

(b) Sample PA signals from 5.16a.

Figure 5.16: Resultant image and signals from PA raster scans using 850 nm light. Images produced using the second PA system set-up and the PCI-5122.

Finally, Fig. 5.15 and 5.16 allow us to assess the penetration of light energy across a skull-mimicking tissue layer. The range of depth chosen for the 2D image slices in Fig. 5.15a and 5.16a coincided with a section of the phantom beneath the layer of skull. Despite using the second PA system with pulse energies between 3.1 - 5.3 mJ/pulse, there were no PA signals correlated with the resin ellipsoid located beneath the skull material. However, the skull-mimicking material did absorb enough light energy in both 750 nm and 850 nm acquisitions to produce its own PA signal. PA pressure waves corresponding with the skull material are evident in Fig. 5.15b and 5.16b, as well as at other pixel locations (x,y) where $y \geq 20$.

5.2.2 Power Readings

During the development of the second PA laser system, pulse energy measurements were taken after the installation of each optical instrument to minimize energy loss occurring in the optical system prior to the probe. Energy output was measured at 5 different locations in the optical path which are labeled in Fig. 5.17. Through the computer interface, the energy output of the OPO was increased from 70-100% in 10% intervals and pulse energy was measured respectively. Once the collimating lens and fiber optic launch was installed, a % energy output of 80% was used. At an energy output $\geq$81%, damage to the fiber optic was observed. According to Table 5.1, the $MagicPRISM^{TM}$ OPO was able to output a maximum of 117 mJ/pulse at 750 nm, and 114 mJ/pulse at 850 nm. $\sim$5% of the pulse energy was lost at stage 2 after the bandpass filters were installed. 50% of the power output at stage 2 was lost after the 0.3 OD filter was installed. Once the collimating lens was installed, 82% of the power output at stage 3 was lost using 750 nm light, and 88% of the power output at stage 3 was lost using 850 nm light. Overall, 95% of the power from the pump laser was attenuated before the output was measured at the probe. According to Table 5.2, the laser pulse energies used fall under the ANSI guidelines for MPE at each wavelength. It was also found that the pulse energy output by the probe for 750 nm light was $\sim$1.76 times that output for 850 nm light.

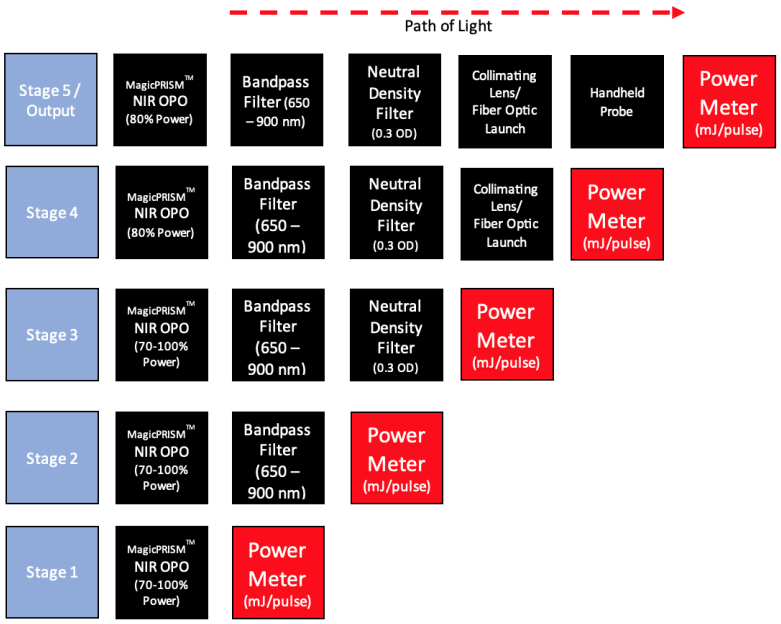

Figure 5.17: Pulse Energy Measurement Diagram.

Pulse Energy Readings (mJ/pulse)	**Stage 1**	**Stage 2**	**Stage 3**	**Stage 4**	**Stage 5**
750 nm	79 - 117 mJ/pulse	76 - 111 mJ/pulse	38.8 – 56.2 mJ/pulse	8.5 mJ/pulse	5.3 mJ/pulse
850 nm	78 - 114 mJ/pulse	76 - 110 mJ/pulse	38.8 – 55.9 mJ/pulse	5.9 mJ/pulse	3.1 mJ/pulse

Table 5.1: Pulse Energy Readings.

assuming 3 mm incident beam radius	**ANSI Safety Guidelines - Skin Exposure (mJ/pulse)**
750 nm	7.12 mJ/pulse
850 nm	11.283 mJ/pulse

Table 5.2: ANSI Laser MPE guidelines.

5.2.3 Maximum Intensity Projections

To establish an expected Red:NIR ratio more accurately, maximum intensity projections (MIP) were reconstructed for the scaffold phantom and the half-covered ellipsoid phantom. To produce the MIPs seen in Fig. 5.18 and 5.19, the amplitude of the 850 nm PA signals was multiplied by the ratio of pulse energy output to account for discrepancies in energy deposition. Finally, the maximum value of every PA signal across all time points is displayed in the 2D MIP.

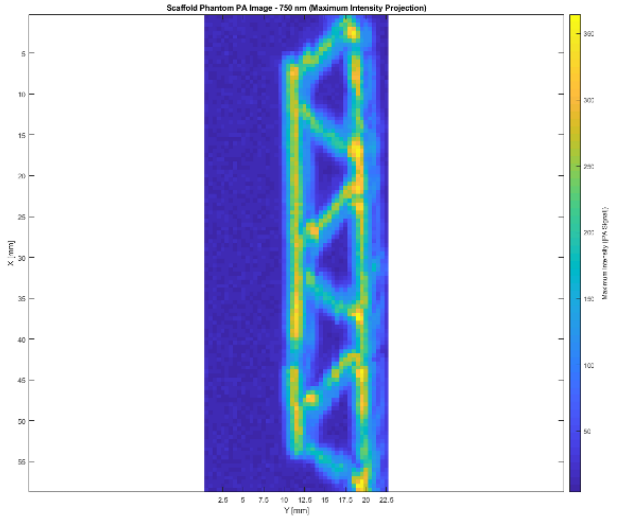

(a) Maximum Intensity Projection of the Scaffold Phantom using 750 nm light.

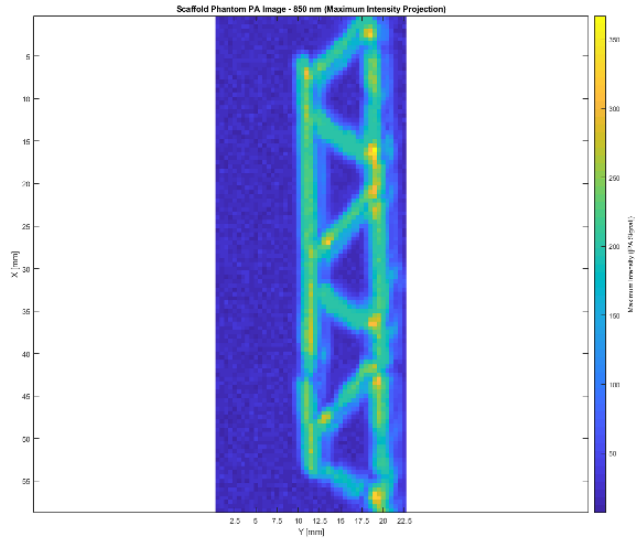

(b) Maximum Intensity Projection of the Scaffold Phantom using 850 nm light.

Figure 5.18: Resultant MIPs from PA raster scans using 750 nm and 850 nm light.

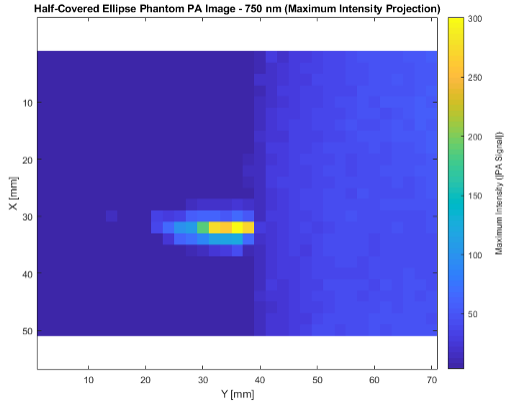

(a) Maximum Intensity Projection of the Half-Covered Ellipsoid Phantom using 750 nm light.

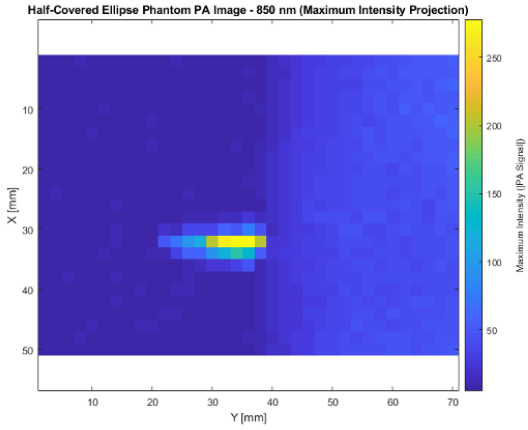

(b) Maximum Intensity Projection of the Half-Covered Ellipsoid Phantom using 850 nm light.

Figure 5.19: Resultant MIPs from PA raster scans using 750 nm and 850 nm light.

According to Figures 5.18 and 5.19, larger amplitude PA signals are more consistently displayed in 850 nm images. Therefore, it is likely that the black plastic resin material has a higher absorption coefficient for 750 nm light than 850 nm light.

5.2.4 Multi-spectral PA Images

In the final steps of the experiment, the Red:NIR ratio of PA images was obtained, and filtering was conducted in an effort to reveal PA signals from depths beneath layers of skull. Subsequently, PA signals were collected from the same location above a simple scaffold phantom. It was found that the maximum amplitude [a.u] of the signal from 750 nm light was 2.018 times that of the signal from 850 nm light. Therefore, if light and ultrasound attenuation is ignored, $\sim$24% of the Red:NIR ratio is contributed by differences in absorption. In Fig. 5.20 and 5.21, Red:NIR ratio images are shown for the simple scaffold phantom and the half-covered phantom. The ratio images are then adjusted to account for differences in incident light energy. For each ratio image, the 850 nm PA signals were scaled by the Red:NIR ratio of the incident pulse energies.

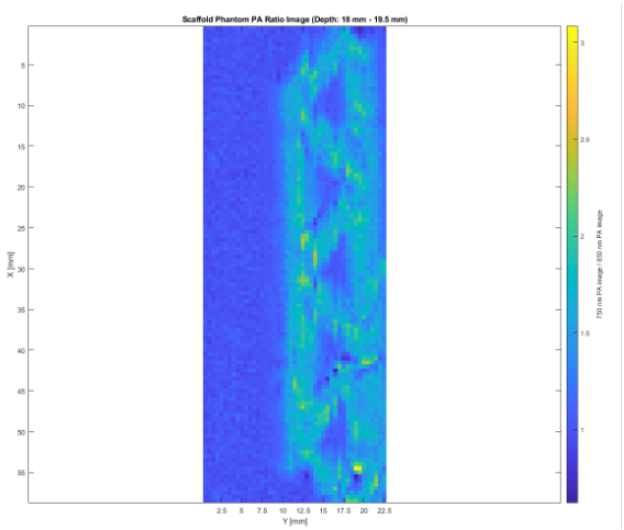

(a) Red:NIR ratio image of the simple scaffold phantom using 750 nm light and 850 nm light at depth 18 - 19.5 mm.

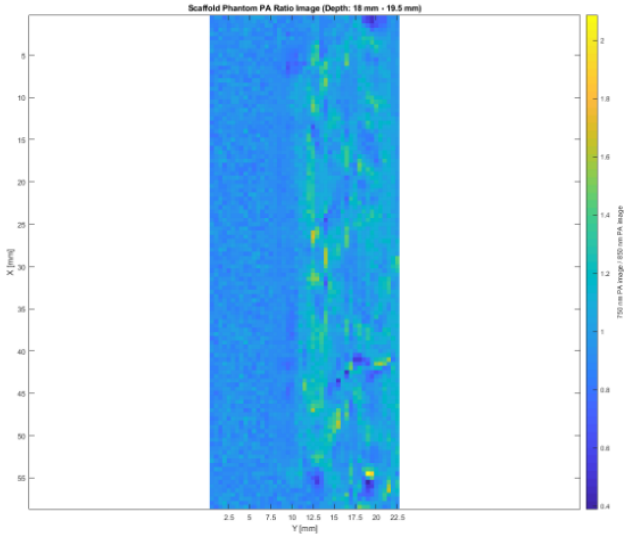

(b) Red:NIR ratio images of the simple scaffold phantom using 750 nm light and 850 nm light at depth 18 - 19.5 mm. 850 nm array has been scaled to accommodate for incident energy mismatch.

Figure 5.20: Red:NIR ratio images from PA raster scans using 750 nm and 850 nm light.

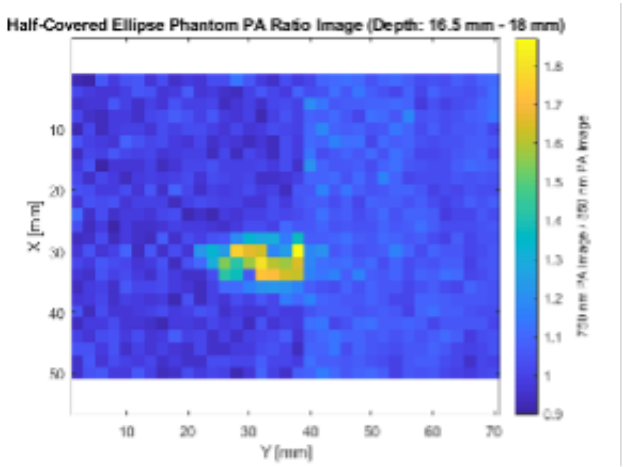

(a) Red:NIR ratio image of the Half-Covered Ellipsoid phantom using 750 nm light and 850 nm light at depth 16.5 - 18 mm.

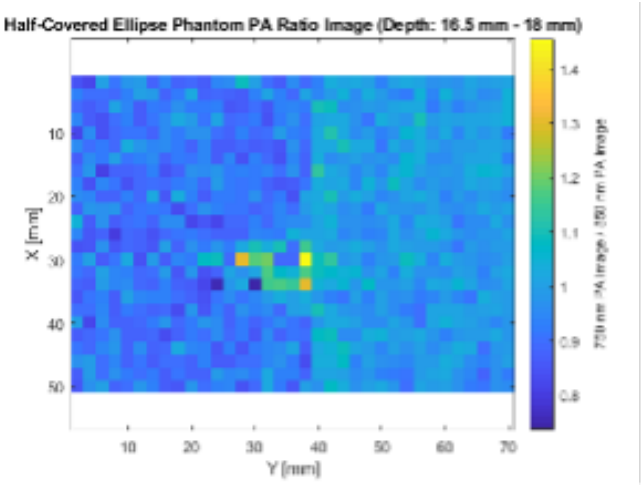

(b) Red:NIR ratio images of the Half-Covered Ellipsoid phantom using 750 nm light and 850 nm light at depth 16.5 - 18 mm. 850 nm array has been scaled to accommodate for incident energy mismatch.

Figure 5.21: Red:NIR ratio images from PA raster scans using 750 nm and 850 nm light.

Fig. 5.20a and 5.21a are included so that the SNR of the absorber in each Red:NIR ratio image can be compared with 5.20b and 5.21b. In Fig. 5.20b and 5.21b, the Red:NIR ratio images for depth images are displayed while accounting for incident energy mismatches. Although the SNR in the ratio images is much less once power scaling is done, the average Red:NIR ratio where the absorber is expected to be located is $\sim$1.3 for the scaffold phantom and $\sim$ 1.2 in the uncovered region of the half-covered phantom. When the Red:NIR ratio is taken of the Half-covered phantom, the difference in absorption is not significant enough to make the ellipsoid visible beneath the layer of skull.

Chapter 6

Conclusion

This thesis discussed the development of a multi-spectral PA imaging system for the purpose of detecting ICH. Initial steps were taken towards implementing an algorithm for estimating blood SpO_2 in ICH imaging phantoms. Findings from other PA imaging studies and results from computer simulations encourage further development of the physical PA system and the Red:NIR ratio technique. In the experiments conducted, there were many limitations identified that hindered the validation of the Red:NIR ratio technique.

6.1 Future Work

In the future, there are many improvements that can be made to the experimental design to improve the robustness of the system.

First, more robust optics alignment can be conducted to minimize power loss before the fiber optic. As seen in Table 5.1 and Table 5.2 the pulse energy used during image acquisitions is still much less than what is permitted under ANSI guidelines.

Also, steps should be taken to design imaging phantoms that more accurately replicate the tissue model of interest. It was observed that the skull-mimicking material used from [63] has a different elastic structure than bone. In future experiments, the optical coefficients of scattering and absorption for the material used in this thesis should be determined for comparison to the parameters of bone described in literature. Subsequently, it is expected that sections of bone tissue *in vitro* and eventually *in vivo* can be used to most accurately test the transcranial capabilities of the PA imaging system. Also, future experiments should test the quantification of blood SpO_2 using the Red:NIR ratio. To do this, one method that should be explored is the artificial oxygenation of mouse or human blood obtained through Canadian Blood Services or other organizations. According to Gehrung *et al.* [21], the oxygenation of blood may be varied using hydrogen peroxide for oxygenation and sodium hydrosulfite for deoxygenation. Using hemoglobin as the target absorber in physical PA image acquisitions will most accurately validate the simulation results.

Otherwise, further signal processing in physical image acquisitions is needed to confirm that PA signals reflect a similar amount of light energy reaching the optical absorbers layers of skull. In simulations, there was scaling of the PA signals produced by the wavelength less than 810 nm due to a discrepancy in absorption coefficients in the skull. During physical image acquisitions, signal processing algorithms can be developed to account for the difference in light absorption by skull-mimicking material between incident wavelengths used for the Red:NIR ratio. For the scaling of PA signals in physical acquisitions, it is important to identify whether skull material is present at each pixel, or if the thickness of the skull varies between (x,y) locations.

Another prospect is to compare the sensitivity of Red:NIR ratio images to more

common LSI procedures when detecting changes in oxygenation. Although both methods use multi-spectral PA images of the same tissue model, the assumptions associated with the formula of best fit method used in simulation data limit the estimation of oxygenation to specific geometries.

6.2 Sources of Error

The major limitation of the experiments in this project includes poor light delivery through the optical paths of both the initial and subsequent PA imaging system setups. As discussed in Section 5.2.2, 95% of the power from the laser pump was lost before output by the probe. Factors limiting effective transmission through system optics include inaccurate beam focusing and alignment. According to 5.1, most of the pulse energy is lost unintentionally after the collimating lens/fiber optic launch. At this stage in the optical path, the beam diameter is focused from 5 mm to 2 mm. It was observed that at % pulse energy levels $\geq$80%, unfocused light pulses were damaging the casing around the fiber core. Therefore, it is suspected that much of the power loss came from light pulses that were not perfectly focused onto the optic fiber core.

Another source of error observed during image acquisitions includes inconsistent grounding of pre-amplifier wiring. Many noise components were discovered to appear intermittently during raster scans and skewed the amplitude of the average Red:NIR ratio at times. To reduce the effect of this noise, a 50 Ω terminator and low-pass filter was attached to the input port for the pre-amplifier. A 50 Ω terminator was attached to the open end of the BNC connection to reduce the reflection of analog voltage signals back toward the pre-amplifier via impedance matching. The low pass filter

was attached directly to the transducer BNC cable to attenuate frequencies higher than 32 MHz from reaching the pre-amplifier. However, a more robust grounding mechanism should be investigated.

Beam spread was another relevant source of error during image reconstruction. The image reconstruction algorithm used assumes a 1-dimensional tissue profile at each (x,y) location when detecting a PA signal. However, the light beam spread significantly once exiting the probe, and could instigate the PA effect in absorbers that were located at different (x,y) locations. As a result, pixels in reconstructed images could localize resultant signal amplitudes to inaccurate (x,y) values. One method that has been explored to counter this is the installation of a beam collimator on the end of the handheld probe. Collimating the light beam output by the probe would irradiate the tissue phantoms with only beams of light parallel to the z-axis of the probe. Additionally, the production of PA apparatuses with multiple detectors would suffer less from this issue. Using the same principles as CT scans, PA systems with multiple detectors can use more than one line of response to localize a signal's origin in 3D space.

Finally, there is also reason to believe that poor ultrasound signal detection hindered PA image reconstruction. It is best practice during ultrasound signal detection to add acoustic impedance matching layers to the front and back-side of the piezoelectric transducer. A matching layer on the front should be investigated to match the acoustic impedance of water because impedance mismatches result in acoustic signal attenuation [6]. Backing layers on the transducer should also be investigated to dampen vibrations from other system hardware that could produce extraneous signals [22].

6.3 Conclusion

To detect ICH as a secondary injury in brain trauma patients, we have chosen to develop a PA system to aid in the monitoring of blood SpO_2. In this thesis, we have developed a PA imaging system to produce optical contrast in Hb species through multi-spectral analysis.

Using the Red:NIR ratio, simulated multi-spectral PA image acquisitions successfully imaged various levels of oxygenation across layers of bone.

To validate simulation results, a 5 ns pulsed Nd:YAG laser was used with an NIR OPO to acquire images of tissue phantoms with varying complexity. Geometries of black plastic resin were surrounded by various materials to mimic ICH conditions. In physical image acquisitions where a layer of bone-mimicking tissue was present at superficial depths, inferior optical absorbers were invisible.

The physical and optical accuracy of tissue phantoms can be greatly improved. Black plastic resin was used because it was a cost-effective and customizable material that proved to produce PA signals from NIR light efficiently. Blood-mimicking material should be used to validate simulation results more closely. Similarly, the optical accuracy of the skull-mimicking material should be tested and validated.

Also, improving the output efficiency of NIR light through laser optics should also be pursued. This can be done through a more rigorous optic alignment procedure to ensure that the maximum amount of pulse energy is transmitted through beam-focusing instruments.

Bibliography

[1] A. B. E. Attia, G. Balasundaram, M. Moothanchery, U. Dinish, R. Bi, V. Ntziachristos, and M. Olivo. A review of clinical photoacoustic imaging: Current and future trends. *Photoacoustics*, 16:100144, Dec. 2019. ISSN 22135979. doi: 10.1016/j.pacs.2019.100144. URL https://linkinghub.elsevier.com/retrieve/pii/S2213597919300679.

[2] P. Beard. Biomedical photoacoustic imaging. *Interface Focus*, 1(4):602–631, Aug. 2011. ISSN 2042-8898, 2042-8901. doi: 10.1098/rsfs.2011.0028. URL https://royalsocietypublishing.org/doi/10.1098/rsfs.2011.0028.

[3] A. G. Bell. On the production and reproduction of sound by light. *American Journal of Science*, s3-20(118):305–324, Oct. 1880. ISSN 0002-9599. doi: 10.2475/ajs.s3-20.118.305. URL https://ajs.scholasticahq.com/article/64037.

[4] L. Brown. The effects of material selection for backing and wear protection/quarter-wave matching of piezoelectric polymer ultrasound transducers. In *2000 IEEE Ultrasonics Symposium. Proceedings. An International Symposium (Cat. No.00CH37121)*, volume 2, pages 1029–1032, San Juan, Puerto Rico,

2000. IEEE. ISBN 978-0-7803-6365-6. doi: 10.1109/ULTSYM.2000.921500. URL http://ieeexplore.ieee.org/document/921500/.

[5] B. Buntz. 5 of the Most Expensive Medical Devices, May 2014. URL https://www.mddionline.com/business/5-most-expensive-medical-devices.

[6] D. Callens, C. Bruneel, and J. Assaad. Matching ultrasonic transducer using two matching layers where one of them is glue. *NDT & E International*, 37(8): 591–596, Dec. 2004. ISSN 09638695. doi: 10.1016/j.ndteint.2004.03.005. URL https://linkinghub.elsevier.com/retrieve/pii/S096386950400026X.

[7] Canadian Association of Radiologists. Addressing the Medical Imaging Dilemma in Canada: Restoring Timely Access for Patients Post-Pandemic, Feb. 2022. URL https://car.ca/advocacy/past-submissions/.

[8] Q. Chen, R. Dewhurst, P. Payne, and A. Davies. Photo-acoustic probe for intra-arterial imaging and therapy. *Electronics Letters*, 29(18):1632, 1993. ISSN 00135194. doi: 10.1049/el:19931087. URL https://digital-library.theiet.org/content/journals/10.1049/el_19931087.

[9] W.-L. Chen, J. Wagner, N. Heugel, J. Sugar, Y.-W. Lee, L. Conant, M. Malloy, J. Heffernan, B. Quirk, A. Zinos, S. A. Beardsley, R. Prost, and H. T. Whelan. Functional Near-Infrared Spectroscopy and Its Clinical Application in the Field of Neuroscience: Advances and Future Directions. *Frontiers in Neuroscience*, 14: 724, July 2020. ISSN 1662-453X. doi: 10.3389/fnins.2020.00724. URL https://www.frontiersin.org/article/10.3389/fnins.2020.00724/full.

[10] S. R. Cherry, J. A. Sorenson, and M. E. Phelps. *Physics in nuclear medicine*. Elsevier/Saunders, Philadelphia, 4th ed edition, 2012. ISBN 978-1-4160-5198-5.

[11] J. R. Cook, R. R. Bouchard, and S. Y. Emelianov. Tissue-mimicking phantoms for photoacoustic and ultrasonic imaging. *Biomedical Optics Express*, 2(11): 3193, Nov. 2011. ISSN 2156-7085, 2156-7085. doi: 10.1364/BOE.2.003193. URL https://opg.optica.org/boe/abstract.cfm?uri=boe-2-11-3193.

[12] X. Cui, S. Bray, D. M. Bryant, G. H. Glover, and A. L. Reiss. A quantitative comparison of NIRS and fMRI across multiple cognitive tasks. *NeuroImage*, 54(4):2808–2821, Feb. 2011. ISSN 10538119. doi: 10.1016/j.neuroimage.2010.10.069. URL https://linkinghub.elsevier.com/retrieve/pii/S1053811910013777.

[13] O. Del Marmol and B. Coulier. "Black" and "White" Blood on Unenhanced CT. *Journal of the Belgian Society of Radiology*, 103(1):16, Feb. 2019. ISSN 2514-8281. doi: 10.5334/jbsr.1733. URL http://jbsr.be/articles/10.5334/jbsr.1733/.

[14] P. Di Ninni, F. Martelli, and G. Zaccanti. The use of India ink in tissue-simulating phantoms. *Optics Express*, 18(26):26854, Dec. 2010. ISSN 1094-4087. doi: 10.1364/OE.18.026854. URL https://opg.optica.org/oe/abstract.cfm?uri=oe-18-26-26854.

[15] Digital Science & Research Solutions, Inc. Dimensions - Publications, 2023. URL app.dimensions.ai.

[16] B. Dong, C. Sun, and H. F. Zhang. Optical Detection of Ultrasound in Photoacoustic Imaging. *IEEE Transactions on Biomedical Engineering*, 64(1):4–15, Jan. 2017. ISSN 0018-9294, 1558-2531. doi: 10.1109/TBME.2016.2605451. URL http://ieeexplore.ieee.org/document/7558159/.

[17] E. S. Donkor. Stroke in the 21st Century: A Snapshot of the Burden, Epidemiology, and Quality of Life. *Stroke Research and Treatment*, 2018:1–10, Nov. 2018. ISSN 2090-8105, 2042-0056. doi: 10.1155/2018/3238165. URL https://www.hindawi.com/journals/srt/2018/3238165/.

[18] Dr. Jeffery Thomas Stroke Shield Foundation. Stroke Types: Ischemic versus Hemorrhagic, Dec. 2013. URL https://strokeshieldfoundation.org/our-research-focus/ischemic-versus-hemorrhagic-stroke-types/.

[19] D. A. Dylewski, A. M. Demchuk, and L. B. Morgenstern. Utility of Magnetic Resonance Imaging in Acute Intracerebral Hemorrhage. *Journal of Neuroimaging*, 10(2):78–83, Apr. 2000. ISSN 10512284. doi: 10.1111/jon200010278. URL https://onlinelibrary.wiley.com/doi/10.1111/jon200010278.

[20] Y. Gao, J. Rong, and X. Jing. The effect of different center frequency of transducers on the photoacoustic tomography. In *2013 IEEE International Conference on Medical Imaging Physics and Engineering*, pages 315–318, Shenyang, China, Oct. 2013. IEEE. ISBN 978-1-4673-5887-3 978-1-4799-6305-8. doi: 10.1109/ICMIPE.2013.6864559. URL http://ieeexplore.ieee.org/document/6864559/.

[21] M. Gehrung, S. E. Bohndiek, and J. Brunker. Development of a blood oxygenation phantom for photoacoustic tomography combined with online pO2 detection and flow spectrometry. *Journal of Biomedical Optics*, 24

(12):1, Oct. 2019. ISSN 1083-3668. doi: 10.1117/1.JBO.24.12.121908. URL https://www.spiedigitallibrary.org/journals/journal-of-biomedical-optics/volume-24/issue-12/121908/Development-of-a-blood-oxygenation-phantom-for-photoacoustic-tomography-combined/10.1117/1.JBO.24.12.121908.full.

[22] B. Gill. Why Does an Ultrasound Probe Need Matching Layers?, May 2017. URL https://www.probomedical.com/learn/blog/why-does-an-ultrasound-probe-need-matching-layers/.

[23] L. W. Goldman. Principles of CT and CT Technology. *Journal of Nuclear Medicine Technology*, 35(3):115–128, Sept. 2007. ISSN 0091-4916. doi: 10.2967/jnmt.107.042978. URL http://tech.snmjournals.org/cgi/doi/10.2967/jnmt.107.042978.

[24] J. Gröhl, T. Kirchner, T. J. Adler, L. Hacker, N. Holzwarth, A. Hernández-Aguilera, M. A. Herrera, E. Santos, S. E. Bohndiek, and L. Maier-Hein. Learned spectral decoloring enables photoacoustic oximetry. *Scientific Reports*, 11(1): 6565, Mar. 2021. ISSN 2045-2322. doi: 10.1038/s41598-021-83405-8. URL https://www.nature.com/articles/s41598-021-83405-8.

[25] Z. Guo, S. Hu, and L. V. Wang. Calibration-free absolute quantification of optical absorption coefficients using acoustic spectra in 3D photoacoustic microscopy of biological tissue. *Optics Letters*, 35(12):2067, June 2010. ISSN 0146-9592, 1539-4794. doi: 10.1364/OL.35.002067. URL https://opg.optica.org/abstract.cfm?URI=ol-35-12-2067.

[26] E. M. Haacke, Y. Xu, Y.-C. N. Cheng, and J. R. Reichenbach. Susceptibility

weighted imaging (SWI). *Magnetic Resonance in Medicine*, 52(3):612–618, Sept. 2004. ISSN 0740-3194, 1522-2594. doi: 10.1002/mrm.20198. URL https://onlinelibrary.wiley.com/doi/10.1002/mrm.20198.

[27] K. Hamada, A. Myoui, T. Ueda, I. Higuchi, A. Inoue, N. Tamai, H. Yoshikawa, and J. Hatazawa. FDG-PET imaging for chronic expanding hematoma in pelvis with massive bone destruction. *Skeletal Radiology*, 34(12):807–811, Dec. 2005. ISSN 0364-2348, 1432-2161. doi: 10.1007/s00256-005-0895-x. URL http://link.springer.com/10.1007/s00256-005-0895-x.

[28] Healthleaders Media Staff. HIGHER-QUALITY MRIS RAISE QUESTIONS ABOUT COSTS AND REIMBURSEMENT, July 2009. URL https://www.healthleadersmedia.com/innovation/higher-quality-mris-raise-questions-about-costs-and-reimbursement.

[29] J. J. Heit, M. Iv, and M. Wintermark. Imaging of Intracranial Hemorrhage. *Journal of Stroke*, 19(1):11–27, Jan. 2017. ISSN 2287-6391, 2287-6405. doi: 10.5853/jos.2016.00563. URL http://j-stroke.org/journal/view.php?doi=10.5853/jos.2016.00563.

[30] Henry Hoffman, MD. Pulse Oximetry Basic Principles and Interpretation, Oct. 2017. URL https://medicine.uiowa.edu/iowaprotocols/pulse-oximetry-basic-principles-and-interpretation.

[31] A. Hillal, T. Ullberg, B. Ramgren, and J. Wassélius. Computed tomography in acute intracerebral hemorrhage: neuroimaging predictors of hematoma expansion and outcome. *Insights into Imaging*, 13(1):180, Nov. 2022. ISSN

1869-4101. doi: 10.1186/s13244-022-01309-1. URL https://insightsimaging.springeropen.com/articles/10.1186/s13244-022-01309-1.

[32] L. Huang, T. Li, and H. Jiang. Technical Note: Thermoacoustic imaging of hemorrhagic stroke: A feasibility study with a human skull. *Medical Physics*, 44(4):1494–1499, Apr. 2017. ISSN 00942405. doi: 10.1002/mp.12138. URL https://onlinelibrary.wiley.com/doi/10.1002/mp.12138.

[33] T. Huppert. Near Infrared Spectroscopy (NIRS) Brain Imaging Laboratory, 2023. URL https://www.researchimaging.pitt.edu/content/near-infrared-spectroscopy-nirs-brain-imaging-laboratory#:~:text=NIRS%20combines%20excellent%20temporal%20resolution,to%20head%20or%20body%20motion.

[34] M. Jain. *Design and Development of a Novel Photoacoustic Imaging System for Detection of Intracranial Hemorrhages*. PhD thesis, McMaster University, Dec. 2018. URL https://www.semanticscholar.org/paper/Design-and-Development-of-a-Novel-Photoacoustic-for-Jain/06a74017624aa58d6162b574d9cc2f153aacbeaa.

[35] K. Joseph Francis, Y. E. Boink, M. Dantuma, M. K. Ajith Singh, S. Manohar, and W. Steenbergen. Tomographic imaging with an ultrasound and LED-based photoacoustic system. *Biomedical Optics Express*, 11(4):2152, Apr. 2020. ISSN 2156-7085, 2156-7085. doi: 10.1364/BOE.384548. URL https://opg.optica.org/abstract.cfm?URI=boe-11-4-2152.

[36] J. Kang, E. M. Boctor, S. Adams, E. Kulikowicz, H. K. Zhang, R. C. Koehler, and E. M. Graham. Validation of noninvasive photoacoustic measurements of

sagittal sinus oxyhemoglobin saturation in hypoxic neonatal piglets. *Journal of Applied Physiology*, 125(4):983–989, Oct. 2018. ISSN 8750-7587, 1522-1601. doi: 10.1152/japplphysiol.00184.2018. URL https://www.physiology.org/doi/10.1152/japplphysiol.00184.2018.

[37] J. Kang, X. Liu, S. Cao, S. R. Zeiler, E. M. Graham, E. M. Boctor, and R. C. Koehler. Transcranial photoacoustic characterization of neurovascular physiology during early-stage photothrombotic stroke in neonatal piglets in vivo. *Journal of Neural Engineering*, 18(6):065001, Dec. 2021. ISSN 1741-2560, 1741-2552. doi: 10.1088/1741-2552/ac4596. URL https://iopscience.iop.org/article/10.1088/1741-2552/ac4596.

[38] J. Kim, S. Park, Y. Jung, S. Chang, J. Park, Y. Zhang, J. F. Lovell, and C. Kim. Programmable Real-time Clinical Photoacoustic and Ultrasound Imaging System. *Scientific Reports*, 6(1):35137, Oct. 2016. ISSN 2045-2322. doi: 10.1038/srep35137. URL https://www.nature.com/articles/srep35137.

[39] W. Koechner. Q-Switching. In *Solid-State Laser Engineering*, volume 1, pages 488–533. Springer New York, New York, NY, 2006. ISBN 978-0-387-29094-2. doi: 10.1007/0-387-29338-8_9. URL http://link.springer.com/10.1007/0-387-29338-8_9. Series Title: Springer Series in Optical Sciences.

[40] R. A. Kruger, R. B. Lam, D. R. Reinecke, S. P. Del Rio, and R. P. Doyle. Photoacoustic angiography of the breast: Photoacoustic angiography of the breast. *Medical Physics*, 37(11):6096–6100, Nov. 2010. ISSN 00942405. doi: 10.1118/1.3497677. URL http://doi.wiley.com/10.1118/1.3497677.

[41] J. Laufer, D. Delpy, C. Elwell, and P. Beard. Quantitative spatially resolved measurement of tissue chromophore concentrations using photoacoustic spectroscopy: application to the measurement of blood oxygenation and haemoglobin concentration. *Physics in Medicine and Biology*, 52(1):141–168, Jan. 2007. ISSN 0031-9155, 1361-6560. doi: 10.1088/0031-9155/52/1/010. URL https://iopscience.iop.org/article/10.1088/0031-9155/52/1/010.

[42] C. Lee, W. Choi, J. Kim, and C. Kim. Three-dimensional clinical handheld photoacoustic/ultrasound scanner. *Photoacoustics*, 18:100173, June 2020. ISSN 22135979. doi: 10.1016/j.pacs.2020.100173. URL https://linkinghub.elsevier.com/retrieve/pii/S2213597920300136.

[43] D. H. Lee, D.-W. Kang, J. S. Ahn, C. G. Choi, S. J. Kim, and D. C. Suh. Imaging of the Ischemic Penumbra in Acute Stroke. *Korean Journal of Radiology*, 6(2):64, 2005. ISSN 1229-6929. doi: 10.3348/kjr.2005.6.2.64. URL https://www.kjronline.org/DOIx.php?id=10.3348/kjr.2005.6.2.64.

[44] C. Li and L. V. Wang. Photoacoustic tomography and sensing in biomedicine. *Physics in Medicine and Biology*, 54(19):R59–R97, Oct. 2009. ISSN 0031-9155, 1361-6560. doi: 10.1088/0031-9155/54/19/R01. URL https://iopscience.iop.org/article/10.1088/0031-9155/54/19/R01.

[45] M. Li, Y. Tang, and J. Yao. Photoacoustic tomography of blood oxygenation: A mini review. *Photoacoustics*, 10:65–73, June 2018. ISSN 22135979. doi: 10.1016/j.pacs.2018.05.001. URL https://linkinghub.elsevier.com/retrieve/pii/S2213597917300575.

[46] W. Li, L. Lin, and G. Li. Wavelength selection method based on test analysis of

variance: application to oximetry. *Anal. Methods*, 6(4):1082–1089, 2014. ISSN 1759-9660, 1759-9679. doi: 10.1039/C3AY41601A. URL http://xlink.rsc.org/?DOI=C3AY41601A.

[47] E. Lin and A. Alessio. What are the basic concepts of temporal, contrast, and spatial resolution in cardiac CT? *Journal of Cardiovascular Computed Tomography*, 3(6):403–408, Nov. 2009. ISSN 19345925. doi: 10.1016/j.jcct.2009.07.003. URL https://linkinghub.elsevier.com/retrieve/pii/S1934592509004055.

[48] G. Liu and R. Whatmore. Design and testing of a d31 mode piezoelectric unimorph for direct power generation by coupling with a microcombustor. In *4M 2006 - Second International Conference on Multi-Material Micro Manufacture*, pages 381–384. Elsevier, 2006. ISBN 978-0-08-045263-0. doi: 10.1016/B978-008045263-0/50087-8. URL https://linkinghub.elsevier.com/retrieve/pii/B9780080452630500878.

[49] Mayo Clinic Staff. Hypoxemia, Mar. 2023. URL https://www.mayoclinic.org/symptoms/hypoxemia/basics/definition/sym-20050930#:~:text=Most%20often%2C%20the%20amount%20of,under%2090%25%20are%20considered%20low.

[50] Mayo Clinic Staff. Stroke, July 2023. URL https://www.mayoclinic.org/diseases-conditions/stroke/symptoms-causes/syc-20350113.

[51] D. W. McRobbie, E. A. Moore, and M. J. Graves. *MRI from picture to proton*. University Printing House, Cambridge University Press, Cambridge ; New York, third edition edition, 2017. ISBN 978-1-107-64323-9.

[52] Meng-Lin Li, Jung-Taek Oh, Xueyi Xie, Geng Ku, Wei Wang, Chun Li, G. Lungu, G. Stoica, and L. Wang. Simultaneous Molecular and Hypoxia Imaging of Brain Tumors *In Vivo* Using Spectroscopic Photoacoustic Tomography. *Proceedings of the IEEE*, 96(3):481–489, Mar. 2008. ISSN 0018-9219, 1558-2256. doi: 10.1109/JPROC.2007.913515. URL `http://ieeexplore.ieee.org/document/4445026/`.

[53] M. M. Miller-Thomas and T. L. Benzinger. Neurologic Applications of PET/MR Imaging. *Magnetic Resonance Imaging Clinics of North America*, 25(2):297–313, May 2017. ISSN 10649689. doi: 10.1016/j.mric.2016.12.003. URL `https://linkinghub.elsevier.com/retrieve/pii/S1064968916301180`.

[54] R. R. Mishra and A. K. Sharma. Microwave–material interaction phenomena: Heating mechanisms, challenges and opportunities in material processing. *Composites Part A: Applied Science and Manufacturing*, 81:78–97, Feb. 2016. ISSN 1359835X. doi: 10.1016/j.compositesa.2015.10.035. URL `https://linkinghub.elsevier.com/retrieve/pii/S1359835X15003917`.

[55] L. Mohammadi, H. Behnam, J. Tavakkoli, and M. Avanaki. Skull's Photoacoustic Attenuation and Dispersion Modeling with Deterministic Ray-Tracing: Towards Real-Time Aberration Correction. *Sensors*, 19(2):345, Jan. 2019. ISSN 1424-8220. doi: 10.3390/s19020345. URL `http://www.mdpi.com/1424-8220/19/2/345`.

[56] J. Muschelli. Recommendations for Processing Head CT Data. *Frontiers in Neuroinformatics*, 13:61, Sept. 2019. ISSN 1662-5196. doi: 10.3389/fninf.2019.

00061. URL https://www.frontiersin.org/article/10.3389/fninf.2019.00061/full.

[57] S. Na, X. Yuan, L. Lin, J. Isla, D. Garrett, and L. V. Wang. Transcranial photoacoustic computed tomography based on a layered back-projection method. *Photoacoustics*, 20:100213, Dec. 2020. ISSN 22135979. doi: 10.1016/j.pacs.2020.100213. URL https://linkinghub.elsevier.com/retrieve/pii/S2213597920300537.

[58] National Institute of Biomedical Imaging and Biomedical Engineering. Ultrasound, July 2016. URL https://www.nibib.nih.gov/science-education/science-topics/ultrasound.

[59] C. R. Nave. Mie Scattering, 2017. URL http://hyperphysics.phy-astr.gsu.edu/hbase/atmos/blusky.html.

[60] V. Ntziachristos. Going deeper than microscopy: the optical imaging frontier in biology. *Nature Methods*, 7(8):603–614, Aug. 2010. ISSN 1548-7091, 1548-7105. doi: 10.1038/nmeth.1483. URL https://www.nature.com/articles/nmeth.1483.

[61] H. N. Panchal, M. S. Shah, and D. S. Shah. Intracerebral Hemorrhage Score and Volume as an Independent Predictor of Mortality in Primary Intracerebral Hemorrhage Patients. *Indian Journal of Surgery*, 77(S2):302–304, Dec. 2015. ISSN 0972-2068, 0973-9793. doi: 10.1007/s12262-012-0803-2. URL http://link.springer.com/10.1007/s12262-012-0803-2.

[62] I. Y. Petrov, Y. Petrov, D. S. Prough, C. J. Richardson, R. A. Fonseca, C. S.

Robertson, C. V. Asokan, A. Agbor, and R. O. Esenaliev. Transmission (forward) mode, transcranial, noninvasive optoacoustic measurements for brain monitoring, imaging, and sensing. In A. A. Oraevsky and L. V. Wang, editors, *Photons Plus Ultrasound: Imaging and Sensing 2016*, page 97084P, San Francisco, California, United States, Mar. 2016. doi: 10.1117/12.2218919. URL `http://proceedings.spiedigitallibrary.org/proceeding.aspx?doi=10.1117/12.2218919`.

[63] K. P. Rao, S. Radhakrishnan, and M. R. Reddy. Brain tissue phantoms for optical near infrared imaging. *Experimental Brain Research*, 170(4):433–437, Apr. 2006. ISSN 0014-4819, 1432-1106. doi: 10.1007/s00221-005-0242-4. URL `http://link.springer.com/10.1007/s00221-005-0242-4`.

[64] V. T. Rathod. A Review of Acoustic Impedance Matching Techniques for Piezoelectric Sensors and Transducers. *Sensors*, 20(14):4051, July 2020. ISSN 1424-8220. doi: 10.3390/s20144051. URL `https://www.mdpi.com/1424-8220/20/14/4051`.

[65] H. A. Rowley. The four Ps of acute stroke imaging: parenchyma, pipes, perfusion, and penumbra. *AJNR. American journal of neuroradiology*, 22(4):599–601, Apr. 2001. ISSN 0195-6108.

[66] T. Shan, H. Yang, S. Jiang, and H. Jiang. Monitoring neonatal brain hemorrhage progression by photoacoustic tomography. *Biomedical Optics Express*, 14(1): 118, Jan. 2023. ISSN 2156-7085, 2156-7085. doi: 10.1364/BOE.469324. URL `https://opg.optica.org/abstract.cfm?URI=boe-14-1-118`.

[67] Smiths Medical PM, Inc. How can SpO2 readings differ from manufacturer to manufacturer?, 2006. URL `http://www.smiths-medical.com`.

[68] K. H. Song and L. V. Wang. Deep reflection-mode photoacoustic imaging of biological tissue. *Journal of Biomedical Optics*, 12(6):060503, 2007. ISSN 10833668. doi: 10.1117/1.2818045. URL http://biomedicaloptics.spiedigitallibrary.org/article.aspx?doi=10.1117/1.2818045.

[69] K. R. Spring, B. O. Flynn, J. C. Long, and M. W. Davidson. Spatial Resolution in Digital Imaging, 2023. URL https://www.microscopyu.com/tutorials/spatial-resolution-in-digital-imaging#:~:text=The%20Nyquist%20criterion%20requires%20a,in%20the%20resulting%20digital%20image.

[70] Steminc. PIEZO RING, 1991. URL https://www.steminc.com/PZT/en/piezo-ring.

[71] ThermoFisher Scientific. India Ink soln., 0.2% in PBS buffer, 2023. URL https://www.thermofisher.com/order/catalog/product/J61007.AP.

[72] T. Thiagarajan. fNIRS: Advances and Challenges, Oct. 2020. URL https://sapienlabs.org/lab-talk/fnirs-advances-and-challenges/#:~:text=Most%20fNIRS%20systems%20have%20spatial,resolution%20of%20about%20100%20Hz.

[73] Titan Electro-Optics. VIBRANT 355 II, June 2012. URL https://www.teo.com.cn/filespath/files/VIBRANT_355II.pdf.

[74] D. Van De Sompel, L. S. Sasportas, A. Dragulescu-Andrasi, S. Bohndiek, and S. S. Gambhir. Improving Image Quality by Accounting for Changes in Water Temperature during a Photoacoustic Tomography Scan. *PLoS ONE*, 7(10):

e45337, Oct. 2012. ISSN 1932-6203. doi: 10.1371/journal.pone.0045337. URL https://dx.plos.org/10.1371/journal.pone.0045337.

[75] D. Viderman, A. Ayapbergenov, N. Abilman, and Y. G. Abdildin. Near-infrared spectroscopy for intracranial hemorrhage detection in traumatic brain injury patients: A systematic review. *The American Journal of Emergency Medicine*, 50:758–764, Dec. 2021. ISSN 07356757. doi: 10.1016/j.ajem.2021.09.070. URL https://linkinghub.elsevier.com/retrieve/pii/S073567572100807X.

[76] K. Wang and M. A. Anastasio. Photoacoustic and Thermoacoustic Tomography: Image Formation Principles. In O. Scherzer, editor, *Handbook of Mathematical Methods in Imaging*, pages 781–815. Springer New York, New York, NY, 2011. ISBN 978-0-387-92919-4 978-0-387-92920-0. doi: 10.1007/978-0-387-92920-0_18. URL http://link.springer.com/10.1007/978-0-387-92920-0_18.

[77] L. V. Wang. Prospects of photoacoustic tomography: Prospects of photoacoustic tomography. *Medical Physics*, 35(12):5758–5767, Nov. 2008. ISSN 00942405. doi: 10.1118/1.3013698. URL http://doi.wiley.com/10.1118/1.3013698.

[78] L. V. Wang and S. Hu. Photoacoustic Tomography: In Vivo Imaging from Organelles to Organs. *Science*, 335(6075):1458–1462, Mar. 2012. ISSN 0036-8075, 1095-9203. doi: 10.1126/science.1216210. URL https://www.science.org/doi/10.1126/science.1216210.

[79] R. Wang, H. Chen, and C. Fan. Impacts of time interval on 18F-FDG uptake for PET/CT in normal organs: A systematic review. *Medicine*, 97(45):e13122, Nov. 2018. ISSN 0025-7974, 1536-5964. doi: 10.1097/MD.0000000000013122. URL https://journals.lww.com/00005792-201811090-00053.

[80] W. Wang, W. Jin, H. Feng, G. Wu, W. Wang, J. Jia, R. Ji, A. Wang, and X. Zhao. Higher Cerebral Blood Flow Predicts Early Hematoma Expansion in Patients With Intracerebral Hemorrhage: A Clinical Study. *Frontiers in Neurology*, 12:735771, Dec. 2021. ISSN 1664-2295. doi: 10.3389/fneur.2021.735771. URL https://www.frontiersin.org/articles/10.3389/fneur.2021.735771/full.

[81] X. Wang, Y. Pang, G. Ku, X. Xie, G. Stoica, and L. V. Wang. Noninvasive laser-induced photoacoustic tomography for structural and functional in vivo imaging of the brain. *Nature Biotechnology*, 21(7):803–806, July 2003. ISSN 1087-0156, 1546-1696. doi: 10.1038/nbt839. URL https://www.nature.com/articles/nbt839.

[82] X. Wang, X. Xie, G. Ku, L. V. Wang, and G. Stoica. Noninvasive imaging of hemoglobin concentration and oxygenation in the rat brain using high-resolution photoacoustic tomography. *Journal of Biomedical Optics*, 11(2):024015, 2006. ISSN 10833668. doi: 10.1117/1.2192804. URL http://biomedicaloptics.spiedigitallibrary.org/article.aspx?doi=10.1117/1.2192804.

[83] Z. Wu, S. Mittal, K. Kish, Y. Yu, J. Hu, and E. M. Haacke. Identification of calcification with MRI using susceptibility-weighted imaging: A case study. *Journal of Magnetic Resonance Imaging*, 29(1):177–182, Jan. 2009. ISSN 10531807, 15222586. doi: 10.1002/jmri.21617. URL https://onlinelibrary.wiley.com/doi/10.1002/jmri.21617.

[84] J. Xia, J. Yao, and L. H. V. Wang. PHOTOACOUSTIC TOMOGRAPHY: PRINCIPLES AND ADVANCES (Invited Review). *Progress In Electromagnetics*

Research, 147:1–22, 2014. ISSN 1559-8985. doi: 10.2528/PIER14032303. URL http://www.jpier.org/PIER/pier.php?paper=14032303.

[85] J. Yao and L. V. Wang. Photoacoustic brain imaging: from microscopic to macroscopic scales. *Neurophotonics*, 1(1):011003, May 2014. ISSN 2329-423X. doi: 10.1117/1.NPh.1.1.011003. URL http://neurophotonics.spiedigitallibrary.org/article.aspx?doi=10.1117/1.NPh.1.1.011003.

[86] W. A. Yost. *Fundamentals of hearing: an introduction*. Academic Press, San Diego, 5th ed edition, 2007. ISBN 978-0-12-370473-3. OCLC: ocm65195303.

[87] T. Young-Schultz, S. Brown, L. Lilge, and V. Betz. FullMonteCUDA: a fast, flexible, and accurate GPU-accelerated Monte Carlo simulator for light propagation in turbid media. *Biomedical Optics Express*, 10(9):4711, Sept. 2019. ISSN 2156-7085, 2156-7085. doi: 10.1364/BOE.10.004711. URL https://opg.optica.org/abstract.cfm?URI=boe-10-9-4711.

[88] E. Z. Zhang, J. G. Laufer, R. B. Pedley, and P. C. Beard. *In vivo* high-resolution 3D photoacoustic imaging of superficial vascular anatomy. *Physics in Medicine and Biology*, 54(4):1035–1046, Feb. 2009. ISSN 0031-9155, 1361-6560. doi: 10.1088/0031-9155/54/4/014. URL https://iopscience.iop.org/article/10.1088/0031-9155/54/4/014.

[89] H. Zhang, M. Ren, S. Zhang, J. Liu, and H. Qin. Microwave-induced thermoacoustic imaging for biomedical applications. *Physica Scripta*, 98(3):032001, Mar. 2023. ISSN 0031-8949, 1402-4896. doi: 10.1088/1402-4896/acbc55. URL https://iopscience.iop.org/article/10.1088/1402-4896/acbc55.

[90] Y. Zhou, J. Yao, and L. V. Wang. Tutorial on photoacoustic tomography. *Journal of Biomedical Optics*, 21(6):061007, Apr. 2016. ISSN 1083-3668. doi: 10.1117/1.JBO.21.6.061007. URL http://biomedicaloptics.spiedigitallibrary.org/article.aspx?doi=10.1117/1.JBO.21.6.061007.